

ABSTRACT

Title of Dissertation: APPLICATIONS OF THE OZONE
MONITORING INSTRUMENT IN OBSERVING
VOLCANIC SULFUR DIOXIDE PLUMES AND
SULFATE DEPOSITION

Niko Markovich Fedkin
Doctor of Philosophy, 2021

Directed by: Professor Russell R. Dickerson
Dr. Can Li
Dr. Nickolay Krotkov
Department of Atmospheric and Oceanic Science

Sulfur dioxide (SO₂), a gas emitted by both volcanoes and anthropogenic activity, is a major pollutant and a precursor to sulfate aerosols. Sulfates can be deposited back to the ground where they have adverse impact on the environment or reside in the stratosphere as aerosols and affect radiative forcing. I investigated two components that stem from SO₂: the deposition of sulfate, and the remote sensing of the SO₂ layer height, important for aviation safety and chemical modeling. In the first study, I used column SO₂ data from the Ozone Monitoring Instrument (OMI), and sulfate wet deposition data from the National Atmospheric Deposition Program to investigate the temporal and spatial relationship between trends in SO₂ emissions and the downward sulfate wet deposition over the northeastern U.S. from 2005 to 2015. The results

showed that emission reductions are reflected in deposition reductions within this same region. Emission reductions along the Ohio River Valley led to decreases in sulfate deposition not only in eastern OH and western PA, but also further downwind at sites in Delaware and Maryland. The findings suggested that emissions and wet deposition are linked through not only the location of sources relative to the observing sites, but also photochemistry and weather patterns characteristic to the region in winter and summer. The second part of this dissertation focuses on SO₂ layer height retrievals and their applications. To this end I applied the Full Physics Inverse Learning Machine (FP-ILM) algorithm to OMI radiances in the spectral range of 310-330 nm. This approach utilized radiative transfer calculations to generate a large dataset of synthetic radiance spectra for a wide range of geophysical parameters. The spectral information was then used to train a neural network to predict the SO₂ height. The main advantage of the algorithm is its speed, retrieving plume height in less than 10 min for an entire OMI orbit. I also compared the SO₂ height retrievals to other data sources and explored some potential applications, in particular their use in volcanic SO₂ plume forecasts and estimating the total mass emitted from volcanic eruptions.

APPLICATIONS OF THE OZONE MONITORING INSTRUMENT IN
OBSERVING VOLCANIC SULFUR DIOXIDE PLUMES AND SULFATE
DEPOSITION

By

Niko Markovich Fedkin

Dissertation submitted to the Faculty of the Graduate School of the
University of Maryland, College Park in partial fulfillment
of the requirements for the degree of
Doctor of Philosophy
2021

Advisory Committee:
Professor Russell R. Dickerson, Chair/Advisor
Professor Zhanqing Li
Professor Timothy Canty
Dr. Nickolay A. Krotkov, Advisor
Dr. Can Li, Advisor
Professor James Farquhar
Research Professor Kenneth E. Pickering

© Copyright by
Niko Fedkin
2021

Acknowledgements

Firstly, I would like to express my gratitude to my research advisors Dr. Can Li and Dr. Nickolay Krotkov at NASA-Goddard for their guidance, support and encouragement throughout my time in the PhD program. I have learned a lot from them, and they have been extremely helpful in mentoring me and providing inputs and feedbacks to my research projects. Likewise, I'd like to thank Prof. Russell Dickerson for his contribution as my academic advisor and his guidance that ultimately helped me to complete my dissertation. I am thankful that I had such amazing advisors that kept me on the right track and also challenged me in different ways.

I would also like to thank our colleagues Diego Loyola and Pascal Hedelt at the German Aerospace Center who aided me in the development of the FP-ILM height retrieval algorithm for OMI, tackling the challenges of machine learning, and providing feedback on my manuscript. Additionally, I thank Robert Spurr, who assisted me with setting up the LIDORT radiative transfer model that I used for my project. I'd like to also acknowledge Prof. Timothy Canty, Prof Zhanqing Li, Dr. Kenneth Pickering and Prof James Farquhar for taking the time to serve on my dissertation committee and providing valuable feedback.

Lastly I thank all friends and family who have kept me sane throughout my graduate school career. I am sincerely grateful for their love, support, and belief in me, even at times when I was doubting myself. Spirituality and religion has also been a big part of my life in the last few years, therefore I have to also give thanks to God for giving me the wisdom and strength to overcome my struggles and stressful times.

Table of Contents

Acknowledgements.....	ii
Table of Contents.....	iii
List of Tables	v
List of Figures.....	vi
Chapter 1: Introduction	1
1.1 Background.....	1
1.2 Remote Sensing of SO ₂	4
1.2.1 UV Spectrometers.....	4
1.2.2 SO ₂ Retrieval Algorithms	8
1.2.3 Retrieval of SO ₂ layer height.....	13
1.3 Research objectives and overview	15
Chapter 2: Sulfate Wet Deposition Trend Analysis	18
2.1 Introduction.....	18
2.2 Methodology	22
2.2.1 Data	22
2.2.2 Trajectory Analysis	24
2.2.3 Potential Source Contribution	27
2.2.4 Normalized Trends	30
2.3 Results	32
2.3.1 Percent Contribution	32
2.3.2 Contribution distribution by distance.....	40
2.3.3 Impact of Maryland Healthy Air Act	44
2.4 Discussion	49
2.4.1 Quantitative Error Estimates.....	49
2.4.2 Other Limitations and Uncertainties	51
2.5 Conclusion	53
Chapter 3: Volcanic SO ₂ Layer Height Retrieval Using Machine Learning	55
3.1 FP-ILM methodology	55
3.1.1 Forward Radiative Transfer Model	56
3.1.2 Data Pre-Processing and Machine Learning	61
3.1.3 Application to Satellite Measurements	66
3.1.4 Parameter Sensitivity Analysis	67
3.2 OMI SO ₂ Layer Height Retrieval Results	70
3.2.1 Kasatochi Eruption	71
3.2.2 Kelud Eruption	73
3.2.3 Calbuco Eruption	75
3.2.4 Raikoke Eruption	76
3.3 Discussion	80
3.4 Conclusion	83
Chapter 4: Application of SO ₂ Layer Height Retrieval	85
4.1 Application of the Algorithm to Other Instruments	85

4.1.1 Background on SNPP-OMPS and NOAA20 OMPS	85
4.1.2 FP-ILM Results.....	87
4.2 Volcanic Plume Tracking	89
4.2.1 HYSPLIT Trajectory Modeling.....	90
4.2.2 Reconstructed Vertical Profiles	97
4.2.3 Discussion	99
4.3 SO ₂ Mass Estimates Using Retrieved Heights	101
4.3.1 Raikoke Mass Estimates	103
4.3.2 Kasatochi Mass Estimates	105
4.4 Conclusion	108
Chapter 5: Overall Conclusions	110
5.1 Summary of Research	110
5.2 Future Work	113
Appendix	116
References	118

List of Tables

Table 2.1. 2005 and 2015 sulfate wet deposition amounts for the six initial case sites

Table 2.2. Mean and median winter SO₂ concentration for 2006-2009 measured by the five AQS sites

Table 2.3. Beltsville wet sulfate deposition, dry sulfate flux and dry SO₂ flux for 2005-2015

Table 3.1. Ranges of the eight physical parameters varied in LIDORT-RRS for synthetic spectra calculations

Table 3.2. Neural network training errors for spectral data with varying SNR

Table 3.3. Mean absolute difference and RMSE for different % reductions of the training dataset

Table 3.4. RMSE and the mean absolute difference of all data points in the test set under different conditions

Table 3.5. Statistical comparisons of the SO₂ height retrievals from different instruments

Table 3.6. Effect of altering random seed number on NN training error and height retrieval results

Table 4.1. Statistics of OMI, SNPP/OMPS and N20-OMPS height retrievals for the Raikoke eruption case

Table 4.2. Distances between the center of masses of the OMI observation and the modeled plume from HYSPLIT

Table 4.3. Location metric for the FP-ILM inputs and the OMI TRU SO₂ VCD dataset

Table 4.4. Calculated total SO₂ mass for Raikoke eruption from FP-ILM and standard heights

Table 4.4. Calculated total SO₂ mass for Kasatochi eruption from FP-ILM and standard heights

Table A1. Cumulative distribution of DJF percent contribution to SO₄²⁻ deposition trend at the Beltsville, MD site, within given ranges from the site

Table A2. Cumulative distribution of JJA percent contribution to SO₄²⁻ deposition trend at the Beltsville, MD site, within given ranges from the site

Table A3. Cumulative distribution of DJF percent contribution to SO₄²⁻ wet deposition trend at the Hackney, OH site, within given ranges from the site

Table A4. Cumulative distribution of JJA percent contribution to SO₄²⁻ wet deposition trend at the Hackney, OH site, within given ranges from the site

List of Figures

Figure 1.1. SO₂ UV absorption cross sections and IR spectrum

Figure 1.2. Measurement principle diagram of OMI

Figure 2.1. Annual trend in OMI Column SO₂ and change in wet SO₄²⁻ deposition between 2005 and 2015 in the eastern United States

Figure 2.2. Locations of observing sites in the NADP network and AQS case sites initially chosen for the study

Figure 2.3. Annual trend NADP sulfate wet deposition and OMI Column SO₂ for 2005-2010 and 2010-2015

Figure 2.4. Scatter plot of the normalized trends for the Beltsville, MD site domain

Figure 2.5. Summer and winter percent contributions to wet deposition trends at Hackney, OH and Beltsville, MD sites.

Figure 2.6. Summer and winter percent contributions to wet deposition trends at South Fayette, Akron, and Wilmington sites

Figure 2.7. Sulfate Wet Deposition amounts at Caldwell, OH NADP site for 1980-2015

Figure 2.8. Map of DJF and JJA 2006-2009 trajectory climatology for Hackney, OH site

Figure 2.9. Map of DJF and JJA 2006-2009 trajectory climatology for Beltsville, MD site

Figure 2.10. Cumulative percentage of contribution to the SO₄²⁻wet deposition trend at the Beltsville NADP site from areas within a given radius from the site

Figure 2.11. Cumulative percentage of contribution to the SO₄²⁻wet deposition trend at the Hackney, OH site from areas within a given radius from the site

Figure 2.12. Monthly averages of hourly SO₂ emissions from the Brandon Shores power generating facility

Figure 2.13. The SO₂ emission inventory from the fuel combustion sector for MD, PA, OH and the entire United States

Figure 2.14. Percent contribution to the Beltsville, MD winter wet deposition trend for 2008-2012.

Figure 2.15. Sulfate Wet Deposition amounts at Beltsville, MD, shown as a time series from 2004 to 2015. The plotted data is from the NADP network at the MD99 site.

Figure 3.1. The flowchart of the FP_ILM methodology for retrieving OMI SO₂ Layer Height.

Figure 3.2. Simulated top of the atmosphere Earthshine radiances for two different SO₂ layer heights, SO₂ height Jacobian (change in radiance per km between the two spectra) along with the absorption cross-sections of SO₂ for reference; (c) the filling-in factor.

Figure 3.3. Explained variance ratio from PCA analysis.

Figure 3.4. Diagram of a neural network with 2 hidden layers.

Figure 3.5. Dependence of retrieval errors on SO₂ amount and SZA

Figure 3.6. SO₂ Height Jacobians (dI/dz) for 4 different assumed SO₂ column amounts

Figure 3.7. Kasatochi eruption plume height comparison between OMI, IASI, GOME-2 and CALIPSO

Figure 3.8. Kelud and Calbuco SO₂ plume height comparisons

Figure 3.9. Probability histograms of SO₂ layer height retrievals for Calbuco and Kelud cases

Figure 3.10. Kasatochi eruption plume height comparison between OMI, IASI, and TROPOMI.

Figure 3.11. Probability histograms of SO₂ layer height retrievals for the Raikoke case

Figure 3.12. CALIPSO lidar backscatter for Raikoke case

Figure 4.1. Raikoke SO₂ layer height retrievals for SNPP/OMPS and NOAA20/OMPS

Figure 4.2. Probability histograms of SO₂ layer height retrievals for SNPP/OMPS and NOAA20/OMPS

Figure 4.3. Starting grid setup for HYSPLIT with the SO₂ layer heights from OMI FP-ILM

Figure 4.4. Trajectory endpoints of HYSPLIT calculations at 23 hours, 46 hours and 69 hours from the OMI orbit 21650 observation

Figure 4.5. Trajectory endpoints from HYSPLIT calculations at (a) 23 hours, (c) 46 hours and (e) 69 hours from the OMI orbit 79449 observation.

Figure 4.6. The reconstructed SO₂ vertical profile using trajectory endpoints for Kasatochi plume

Figure 4.7. The reconstructed SO₂ vertical profile using trajectory endpoints for Raikoke plume

Figure 4.8. Flow chart of potential HYSPLIT-based volcanic plume forecasting system

Figure 4.9. Interpolated OMI VCDs for the Raikoke eruption case

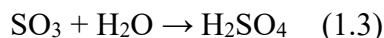
Figure 4.10. Interpolated OMI VCDs for the Kasatochi eruption case

Chapter 1: Introduction

1.1 Background

Sulfur dioxide (SO₂) gas is a toxic pollutant released by both volcanoes and human activity, in particular through burning of sulfur-rich fossil fuels such as coal and petroleum. It can be also produced from smelting of metals. From anthropogenic sources around ~55-65 Tg S, are released into the atmosphere each year [Smith et al., 2011]. In the last twenty years, the regions with the most severe SO₂ pollution have been in India and China where coal combustion has been a primary source of energy. Other locations such as Norilsk, Russia and the Persian Gulf have been the largest point sources of SO₂ in the world due to nickel smelting and oil industry respectively. Through pollution controls such as flue gas desulfurization technology, the level of sulfur pollution can be greatly reduced. China is a good example of this: from 2010 to 2017 the SO₂ emissions from the country were reduced by around 62% [Zheng et al., 2018]. In the northeast United States, areas that previously experienced high SO₂ pollution, SO₂ levels have decreased significantly since the start of the 21st century thanks to sulfur scrubbers and phasing out of coal power plants. While anthropogenic emissions of SO₂ have gone down in some areas, coal remains an important energy source particularly in some developing countries such as India [Li et al., 2017a]. As a result, anthropogenic SO₂ sources continue to play an important role in regional air quality.

One of the main sinks of SO₂ in the atmosphere oxidation into sulfates (SO₄²⁻). The hydroxyl radical (OH) is the dominant driver of oxidation process in the gas phase. It reacts with SO₂ in a multi-step reaction (Eq 1.1-1.3) which eventually results in formation of sulfuric acid [Margitan, 1984]:



Alternatively, SO_2 can be taken up by water droplets and heterogeneous reactions with dissolved hydrogen peroxide (H_2O_2) or ozone (O_3) [Seinfeld and Pandis, 2006] yield sulfate. The aqueous phase reaction is faster than the homogeneous reaction and accounts for roughly 85% of the global sulfate source [Chin et al, 1996]. Sulfate that resides in the troposphere eventually undergoes deposition through either dry or wet processes. In wet deposition, the sulfate is removed through precipitation, which results in acid rain and can cause damage to various ecosystems by destroying vegetation and changing the acidity of ground water [Singh and Agrawal, 2008; Likens and Bormann, 1974]. In dry deposition, the sulfate is deposited to the environment without the presence of precipitation. Ground monitoring networks as well as several studies have attempted to make estimates through modeling deposition velocities in order to determine the flux [Odabasi and Bagiroz, 2002; Xu and Carmichael, 1998]. As a result, dry deposition has larger errors in its estimates than wet deposition since it is not measured directly but rather through a product of measured concentration and modeled velocities. The amount of wet sulfate deposition and its fraction of the total deposition vary by region depending on the proximity to sulfur emission sites and precipitation frequency. For instance, at a strongly polluted site in China, the dry deposition was estimated to be 2-4 times greater than wet deposition [Quan et al., 2008]. Conversely, dry deposition accounted for about 40% of the total according to a study on the eastern United States [Baumgartner et al., 2002]. Historically, sulfate deposition and acid rain have occurred downwind of SO_2 emission sources, most notably coal-

fired power stations. I will discuss sulfate deposition in more detail in Chapter 2 of this dissertation.

Volcanoes are the largest natural source of SO₂ and are estimated to emit 20-25 Tg S through passive degassing [Carn et al., 2017] each year. Explosive volcanic eruptions, however, can additionally release large amounts of SO₂ high into the atmosphere. While anthropogenic SO₂ typically has a lifetime of a few days [Lee et al., 2011], volcanic SO₂ injected into the lower stratosphere can take a few weeks to convert into sulfate [von Glasow et al., 2009, Krotkov et al., 2010; Gorkavyi et al., 2021]. This can also lead to formation of sulfate aerosols which can remain in the stratosphere for months to years, with an e-folding residence time of one year [Robock, 2000]. Sulfate aerosols are known to have a cooling effect on climate, especially if a large SO₂ plume is injected into the lower stratosphere and remains there for longer periods of time. This is demonstrated by significant eruptions such as El Chichon in 1982 [Krueger 1983] and Mt. Pinatubo in 1991 that released 7 Mt and 15-20 Mt of SO₂ into the atmosphere respectively [Bluth et al., 1992; Carn 2021]. In the case of the Mt. Pinatubo eruption, the most explosive eruption of the 20th century, global average temperatures were reduced by around 0.5°C [McCormick et al, 1995; Stenchikov et al., 2021]. This eruption had other atmospheric effects such as depleting ozone in the mid-latitudes and altering atmospheric circulation patterns [Robock and Mao, 1995; Robock, 2002].

Aside from releasing SO₂, volcanic eruptions also emit large amounts of ash into the atmosphere [Stenchikov et al., 2021] which can have adverse impacts on air travel. Ash from volcanic plumes can often interfere with flight paths, greatly reduce visibility near the ground, and cause damage to the aircraft including possible engine failures [Carn et al., 2009]. In addition, SO₂ that is converted to sulfuric acid can cause sulfidation in the engines, an effect that

can reduce their lifetimes [Bernard and Rose, 1990]. From 1953 to 2009, over 120 aviation incidents involving volcanic activity were reported, with roughly 80 of them involving serious damage to the airframe or engine [Guffanti et al., 2010]. Due to the Mt. Pinatubo eruptions in June 1991, more than 40 separate aviation incidents occurred [Casadevall et al. 1996]. There is also the possibility of highly concentrated volcanic SO₂ plumes producing acidic aerosols which can cause irritation of the eyes, nose, and respiratory airways of occupants inside airplanes [Schmidt et al., 2014]. In many cases volcanic SO₂ and ash are collocated, thus making SO₂ a useful proxy for the location of the ash plume. This aids in aviation hazard mitigation and volcanic plume forecasting [Krotkov et al., 2021].

1.2 Remote Sensing of SO₂

1.2.1 UV Spectrometers

For purposes of measuring pollution, concentrations of SO₂ can be measured with in-situ sensors on the ground and or aboard aircraft. However, these measurements do not provide spatial coverage over the entire globe. For this purpose, remote sensing instruments on satellites are used. A variety of gases such as SO₂, NO₂, O₃ and CO₂ can be measured from satellites by extracting absorption features from the measured spectrum. SO₂ information is found both in the UV spectrum in the 300-380 nm range as well as in the infrared range. The absorption of UV light results in an electronic transition (i.e., excitation of an electron) at wavelengths defined by the absorption cross section (Figure 1.1). The IR absorption, however, is caused by vibration and rotations in the molecule. The symmetric and nonlinear geometry of SO₂ allows 3N-3 internal degrees of freedom, where N is the number of atoms in the molecule. Thus it has 3 rotational and 3 vibrational modes (symmetric stretch, antisymmetric stretch and bending) which all interact with infrared radiation.

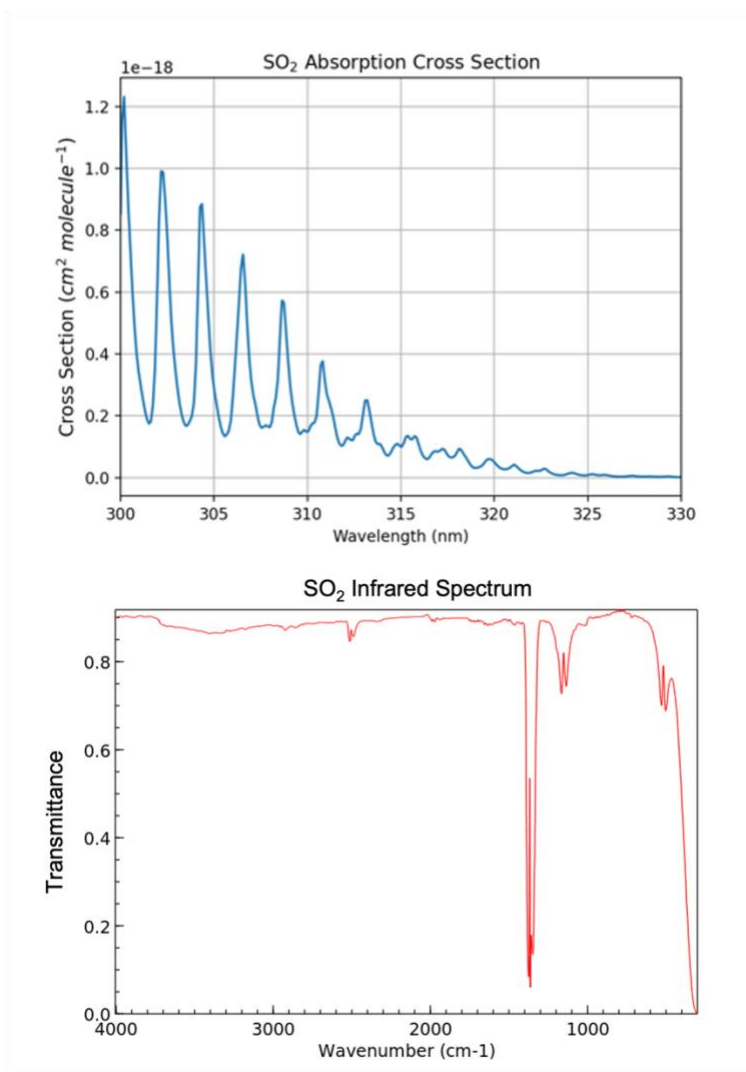


Figure 1.1: The (a) SO₂ absorption cross section from Bogumil et al., (2013) in the 300-330 nm UV range and (b) SO₂ transmittance in the IR spectrum. These cross section peaks in (a) show the wavelengths at which there is the highest probability of interaction with UV radiation, while the inverted peaks in (b) show the SO₂ IR absorption bands. The IR spectrum data was obtained from the NIST Chemistry WebBook (<https://webbook.nist.gov/chemistry>).

Backscattering ultraviolet (BUV) spectrometers have been used to monitor SO₂ from volcanic plumes for the last 40 years and starting in the mid 1990s pollution near the ground. One of the first instruments to monitor volcanic SO₂ was the Total Ozone Mapping Spectrometer (TOMS) [Krueger 1983; Krueger et al., 1995;], launched in 1979 with the National Aeronautics and Space Administration (NASA) Nimbus-7 satellite. Ozone data from TOMS aided greatly in

visualizing the ozone hole discovered in the 1980s, as well as a number of volcanic eruptions. TOMS used 6 wavelength bands to measure ozone and SO₂, however the next generation of instruments were hyperspectral meaning they could measure the UV spectrum at hundreds of wavelengths and at relatively fine spectral resolutions (~1 nm or finer). This led to improvements in detection and in separating SO₂ signals from other species, helping to reduce retrieval noise. One of those was the Global Ozone Monitoring Experiment (GOME) instrument [Burrows et al., 1999], launched in 1995, and later improved upon with the GOME-2 instrument [Munro et al., 2016], which currently flies on the MetOp satellites. The OMI instrument [Levelt et al., 2006], the primary instrument used in this work, is a Dutch-Finish contribution to the NASA Aura satellite and has been operational since 2004. The instrument senses the atmosphere with a 2600 km swath width in a push broom style as the satellite travels in a near-polar sun synchronous orbit with a local equator crossing time of ~13:45. It has 60 cross track positions (rows), a 13 × 24 km² spatial resolution at the nadir position, and a ~0.5 nm spectral resolution. The instrument has two UV channels and one visible channel to measure backscattered radiances from the Earth's atmosphere across the 270-500 nm range. For this work I exclusively used the UV2 channel which makes UV radiance measurements between 307 and 380 nm. OMI also has a 2-D charge coupled device (CCD) detector, one spectral dimension and other covering the cross-track viewing rows [Levelt et al, 2002]. These aspects are illustrated in Figure 1.2.

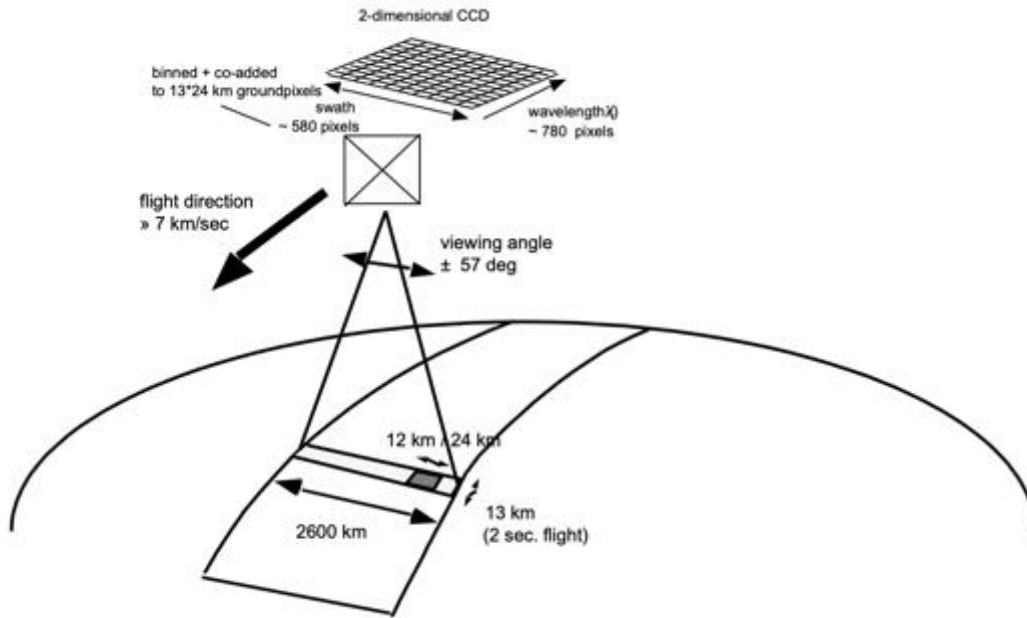


Figure 1.2: Measurement principle of OMI showing the 2-dimensional CCD and the measurement swath. This image was obtained from the OMI Algorithm Theoretical Basis Document (Levelt et al., 2002).

Since 2009, the quality of OMI Level 1 radiance data from about half of the OMI rows has been affected by the row anomaly. This anomaly affects individual rows and slowly evolves over time. As a result, the row anomaly has reduced the daily spatial coverage of Level 2 data products. These products are the geophysical quantities, such as gas column amounts, derived from the Level 1 backscattered radiance data. The cause of the row anomaly is thought to be an internal obstruction of the sensor [Torres et al., 2018].

In 2011 NASA launched the first of the Ozone Mapping and Profiler Suite (OMPS) instruments onboard the NASA/NOAA Suomi-NPP (SNPP) satellite. It consists of three components: a downward looking nadir mapper, a nadir profiler, and a limb profiler [Jaross et al., 2013] which is used to obtain vertical profiles of ozone and aerosol extinction. OMPS was intended for operational forecasting purposes but also been used for extending NASA's data record of ozone and SO₂ with TOMS and OMI. Newer instruments have been launched that

further improve on the resolution of previous generation of instruments. One such spectrometer is the TROPospheric Monitoring Instrument (TROPOMI) launched in 2017 on the Sentinel-5 Precursor satellite. TROPOMI improves upon OMI through its drastic increase in spatial resolution – $7 \times 3.5 \text{ km}^2$, which is around 13 times higher than OMI. This allows the instrument to observe SO₂ plumes in unprecedented detail. In the years since its launch the instrument has provided highly detailed observations of significant volcanic eruption such as Mt. Sinabung [de Laat et al., 2018], Mt Etna [Queißer et. al, 2019] and Raikoke [de Leeuw et al., 2021], as well as small SO₂ emission sources from volcanic degassing [Theys et al., 2019] and anthropogenic activities [Fioletov et al., 2020; Theys et al., 2021]. Another OMPS instrument was also launched onboard the NOAA-20 satellite in 2017. It has a spatial resolution of 17 by 17 km², around 8.5 times greater than that of the SNPP/OMPS.

1.2.2 SO₂ Retrieval Algorithms

SO₂ can be retrieved using a technique called Differential Optical Absorption Spectroscopy (DOAS)[Platt, 1994; Platt and Stutz, 2008]. While implementation details for each instrument vary, the idea remains similar. DOAS utilizes the Beer Lambert Law to find the absorption of solar irradiance for each wavelength. In its simplest form it is expressed as such:

$$I(\lambda, s) = I_0 \exp(-\sigma(\lambda)\rho s) \quad (1.4)$$

Where $I(\lambda, s)$ is the light intensity at the end of the path, I_0 is the incoming intensity, σ is the absorption cross section ρ is the concentration of the absorbing gas and s is the length of the light path. In practical applications, additional terms are added to the equation to account for the

Rayleigh and Raman scattering from air molecules, aerosols, and clouds in the atmosphere. This method helps to obtain the slant column density (SCD) which represents the amount of the gas along the light path. The next step is the conversion of the SCD into a vertical column density (VCD), which is the amount of gas in the column directly above a given location at the surface. This is done using Air Mass Factors (AMFs). The AMF is defined as the ratio of the VCD to the SCD:

$$AMF = \frac{VCD}{SCD} \quad (1.5)$$

With the absence of scattering, a simple geometric AMF is used which is just a function of the solar zenith angle (SZA) θ_s , and viewing zenith angle (SCD), θ_v [Palmer et al., 2001]:

$$AMF_g = \sec\theta_s + \sec\theta_v \quad (1.6)$$

However, in practice, AMFs also depend on a number of different quantities including the vertical profile of the trace gas, surface albedo, the viewing geometry, and effects of clouds and aerosols. These variables take into account the scattering and absorption in the atmosphere and surface BRDF [Vasilkov et al., 2017]. Therefore the AMF can also be expressed as:

$$AMF = AMF_g \int_0^\infty w(z)S(z)dz \quad (1.7)$$

Where $w(z)$ is the “scattering weight” describing the atmospheric scattering and surface BRDF processes [Palmer et al., 2001; Martin et al., 2002; Eskes and Boersma 2003; Krotkov et al., 2017; Lamsal et al., 2021] and $S(z)$ is the vertical profile shape of the absorber (normalized to VCD). In most cases a forward radiative transfer model is used to calculate the $w(z)$ and a-priori absorber vertical profile, $S_a(z)$, to calculate AMF (1.7). Column amounts of SO_2 are commonly expressed in Dobson Units (1 DU = 2.69×10^{16} molecules/cm²) similar to ozone.

The DOAS technique is widely employed to retrieve weakly absorbing trace gases with spectral optical thickness less than 1 [Eskes and Boersma, 2003]. It was used as the legacy SO₂ algorithms for UV-based instruments such as GOME and SCIAMACHY [Richter et al., 2006; Lee et al., 2009] and OMI [Theys et. al., 2015]. The first operational SO₂ retrieval for OMI was based on the band residual difference (BRD) algorithm in the strong ozone and SO₂ absorption UV2 region between 310nm and 313nm [Krotkov et al., 2006]. This algorithm used wavelength pairs consisting of four wavelengths that are centered on the SO₂ absorption bands. The SO₂ amount was retrieved by finding the difference in absorption in the pairs and minimizing the residuals in the radiative transfer model. This algorithm had reasonable sensitivity to low SO₂ amounts, as it took advantage of the strongest SO₂ absorption bands, thus making it suitable for retrieving SO₂ in the PBL. However, for large SO₂ column amounts, as is the case for strong volcanic eruptions, there was notably more uncertainty due to band pair residual starting to show nonlinear and nonmonotonic responses to increases in SO₂ [Yang et al., 2007]. The Linear Fit algorithm [Yang et al., 2007] attempted to rectify this issue by introducing longer wavelength (> 320 nm) bands into the retrieval for large SO₂ loadings. At the longer wavelengths, the response to changes in VCD are more linear than shorter wavelength because SO₂ absorption is weaker. Similar to BRD, the idea of the algorithm is to minimize the residuals of total ozone column amounts retrievals, between the measured top-of-atmosphere (TOA) radiance and the radiance calculated by the forward radiative transfer (RT) model. The calculated radiance is a function of the O₃ and SO₂ column amounts and surface reflectivity. Thus, through fitting the measured spectra both the SO₂ and O₃ VCD can be retrieved.

These two legacy algorithms were used operationally until the invention of the alternative data driven principal component analysis (PCA) algorithm [Li et al., 2013], which retrieves SO₂

VCDs by fitting Principal Components (PCs) of the covariance matrix of the OMI spectral radiance measurements. The PCA technique was also extended to OMI volcanic SO₂ retrievals and operational OMPS instrument on NASA/NOAA Suomi NPP polar orbiting satellite [Li et al., 2017; Zhang et al., 2017; Li et al., 2020]. The PCA method is based on fitting principal components (PCs) extracted from measured radiance data over SO₂ free regions. These PCs implicitly represent combined effect of different interfering processes such as the O₃ absorption, Raman scattering and instrument effects (e.g., wavelength shift). The PCs are then fitted with the pre-calculated column SO₂ Jacobians from a look up table in order to obtain the SO₂ VCD. Column Jacobians represent the sensitivity of the backscattered radiance to the SO₂ VCD. The relationship between the logarithm of the sun normalized radiance (N), the n_v PCs (v_i), coefficients of the PCs (ω), the VCD (Ω_{SO_2}) and SO₂ Jacobians ($\frac{\partial N}{\partial \Omega_{SO_2}}$) is expressed as follows [Li et al., 2013]:

$$N(\omega, \Omega_{SO_2}) = \sum_{i=1}^{n_v} \omega_i v_i + \Omega_{SO_2} \frac{\partial N}{\partial \Omega_{SO_2}} \quad (1.8)$$

This data-driven approach is advantageous since the SO₂ signals can be derived directly from UV measurements. This removes the need for on-line RT calculations (aside from pre-computed Jacobian LUTs). Furthermore, it improves significantly over previous algorithms by reducing biases and suppressing noise by a factor of 2. For volcanic retrievals, all satellite algorithms still have low bias in retrieved total SO₂ mass in fresh opaque volcanic plumes, especially in the presence of volcanic ash [Fisher et al., 2021]. However, the OMI PCA-based volcanic SO₂ algorithm has improved the sensitivity in observing small volcanic sources as well as increasing accuracy in large eruptions by automatically shifting spectral fitting window to the longer and more transparent UV wavelengths [Li et al., 2017]. Overall, the PCA algorithm is

similar to DOAS, but the key difference is that it uses spectral fitting vectors extracted directly from the measured radiances to implicitly account for combined effect of all interfering atmospheric and instrumental processes rather than lab-measured cross sections and parameterized interferences.

The retrieval process for all satellite SO₂ algorithms assume an a priori vertical profile of SO₂. Vertical profiles are needed in the calculation of the SO₂ Jacobian look-up table. Since volcanic plume heights vary for different eruptions, operational retrievals typically assume four different Gaussian profiles with center of mass altitudes of 3, 8, 13 and 18 km. The altitudes represent the lower troposphere (TRL), middle troposphere (TRM), upper troposphere (TRU) and lower stratosphere (STL), respectively. Note that the TRL, TRM and STL profiles were also used in legacy SO₂ algorithms [Krotkov et al., 2006; Yang et al., 2007; Fisher et al., 2019]. The OMI SO₂ VCDs contain 4 separate datasets based on the different height assumptions. The PCA algorithm is also used for the operational OMPS SO₂ products. The OMPS retrieval data were shown to be largely consistent with OMI retrievals, especially for larger sources [Zhang et al., 2017].

Lastly it should be noted that SO₂ retrievals can also be obtained from IR-based instruments [Realmuto, 2000; Thomas and Prata, 2011; Hyman and Pavolonis, 2020]. For instance, the Infrared Atmospheric Sounding Interferometer (IASI) and the Atmospheric Infrared Radiation Sounder (AIRS) [Prata and Bernardo, 2007] have both been used extensively in the last 20 years to retrieve and observe SO₂. IASI is one of the most advanced current operational IR sounders and was launched in 2006, 2012 and most recently in 2018, onboard the MetOP-A, MetOp-B and MetOp-C satellites respectively. It has a high spectral resolution (0.5 cm⁻¹) and a 12 km diameter circular footprint at nadir. The main advantage of IR instruments is that unlike

visible and UV instruments, they do not need sunlight to make measurements, making them useful for sensing at night and during the winter at high latitudes [Krotkov et al., 2021].

However, SO₂ IR retrievals are generally less sensitive to SO₂ at lower altitudes in tropics due to interference with water vapor and surface emissivity. The SO₂ retrieval for IASI [Clarisse et al., 2012], and most other IR instruments, such as MODIS and VIIRS [Realmutu 2000; Krotkov et al., 2021] utilizes the mid IR-range and exploits one or multiple of three SO₂ absorption bands centered at 4, 7.3, and 8.7 μm. These bands are of varying strengths; for example, 7.3 μm band is the strongest by far and the combination band (4 μm) is the weakest and can only be used with reflected solar light. Infrared retrievals from IASI have produced good results for volcanic eruptions in the last 10 years and have been an important addition to SO₂ observation.

1.2.3 Retrievals of SO₂ Layer Heights

In addition to column amounts, backscattered radiances can provide important information about the height of an SO₂ layer, useful information for volcanic ash advisory centers (VAAC) which play a major role in mitigating aviation hazard related to volcanoes. Conceptually, a change in altitude of an SO₂ plume alters the number of backscattered photons going through the layer. If a plume is high in the atmosphere, more photons that are scattered from below the layer pass through the absorbing SO₂ plume. Thus, information about the plume altitude can be found in the UV spectra, especially in the 310-320 nm range where Rayleigh scattering is dominant. Relative to the SO₂ amount, obtaining a fast retrieval of the height of a volcanic plume presents a greater challenge. The retrieved SO₂ amount is dependent on the SO₂ height thus making the two quantities interlinked; this makes more challenging to separate the impacts of each in UV radiances. Consequently, retrieving the height of a plume with satellite measurements would require disentangling the two quantities in the UV radiances. This is more

difficult for the SO₂ height given that the SO₂ absorption is a more dominant feature in the spectra.

Until recently, SO₂ layer height retrieval techniques have involved direct spectral fitting approaches that use backscattered ultraviolet (BUV) measurements in conjunction with extensive forward radiative transfer modeling. The Iterative Spectral Fitting (ISF) algorithm [Yang et al., 2009] was the first OMI SO₂ height algorithm to include simultaneous retrieval of SO₂ height and column amount. Similar to SO₂ amounts, it determined the altitude of the SO₂ layer by adjusting the height at each iteration while minimizing the differences between measured radiances and forward RT calculations. The key to separating the impact of SO₂ height from the amount was to calculate the Jacobians of both the height and amount, and update them through each iteration. Similar spectral fitting techniques involving the VLIDORT RT model [Spurr et al., 2006] were also implemented for the GOME-2 instrument [Nowlan et al., 2011]. The SO₂ plume height has also been retrieved with IR measurements from IASI. The algorithm utilized brightness temperature changes and relative intensities of radiation between absorption lines [Clarisse et al., 2008; Clarisse et al., 2010]. While the height retrievals from spectral fitting methods are accurate, the main disadvantage is the extensive use of radiative transfer modeling and other assumptions including a reasonable first guess for the plume altitude. This makes retrievals too slow for applications in near real time (NRT). Newer schemes were developed for GOME-2 using the SO₂ Plume Height Rapid Inversion (SOPHRI) algorithm [Rix et al., 2012], a DOAS based technique that worked by minimizing differences between plume height from simulated spectra and the assumed height from measured spectra. This technique allowed for reasonably fast retrievals that could be used in near real-time, thanks to the use of pre-calculated GOME spectra stored in a look up table classified according to SO₂ column, SO₂ heights and

other physical parameters. An updated algorithm was also developed for IASI [Clarisse et al., 2014], this time implementing an optimal estimation fit approach with pre-calculated Jacobians. Even faster and more efficient methods for GOME-2 [Efremenko et al., 2017] and TROPOMI [Hedelt et al., 2019] have made use of machine learning algorithms, specifically neural networks (NNs), to develop a trained, full-physics inverse learning machine (FP-ILM) for retrieving SO₂ plume height. The neural network based algorithms provides a quicker and more efficient way of separating out the height information in spectra than previous spectral fitting approaches. This approach has shown good accuracy and speed fast enough for near-real-time operations. The FP-ILM has also been used for retrieving ozone profile shapes [Xu et al., 2017] and geometry-dependent Lambertian equivalent reflectivity [Loyola et al., 2020]. This algorithm is the basis for my work on the OMI volcanic SO₂ height retrieval presented in Chapter 3.

1.3 Research Overview

Since its launch in 2004, the SO₂ data from OMI has been applied to study the trends in SO₂ pollution, to analyze the sources and sinks of SO₂, and to advance the record of data products valuable to both researchers and the general public. In this dissertation I will present two studies to demonstrate the use of OMI and other satellite data in monitoring sulfur pollution and volcanic SO₂.

First, I analyze trends of SO₂ and sulfate pollution in the northeastern United States and the Ohio River Valley, a region with a considerable number of coal-fired power plants. Since the late 20th century SO₂ emissions from the region have been decreasing. Even during the time of OMI operations (post 2005), swift regulations on coal plants have led to further downward trends in SO₂. As a result, sulfate deposition is also expected to decrease as compared. I attempt to link

regions of decreased SO₂ emission with downwind areas where there is a negative sulfate wet deposition trend using OMI data, ground deposition data from the National Atmospheric Deposition Program (NADP), and trajectory modeling. I also quantify these contributions and analyze the seasonal difference in the trends. While this work has focused on the United States, this methodology I developed can be potentially used for diagnosing trends and effects of environmental policy changes for other polluted regions. This work was published in Fedkin et al. [2018].

In chapter 3, I present a fast new volcanic SO₂ layer height retrieval for the OMI and OMPS instruments. This retrieval uses machine learning to train the algorithm to find SO₂ height signals in BUV radiance data. The primary advantages of this approach are the execution speed and the good spatial coverage provided by OMI and OMPS. I separated the training phase, which involves time consuming radiative transfer computations and machine learning model training, from the application phase, where the desired parameter can be retrieved within milliseconds for a single satellite ground pixel using the trained model. I also show comparisons of the height retrievals with other sensors. Because this retrieval is faster than previous OMI and OMPS retrievals it can potentially be transitioned into a NRT data production system that will aid in aviation hazard mitigation and provide information for chemical models and data assimilation within a few hours. This work was published in Fedkin et al. [2021].

The fourth chapter will focus on the potential applications of the volcanic SO₂ height retrieval. First, I examine how the retrieval can be used in volcanic plume forecasting. While observations are valuable, in many cases forecasts are needed by Volcanic Ash Advisory Centers (VAACs). For this purpose, I analyze how well HYSPLIT can forecast the plume height and location if supplied with the OMI retrieved heights and compare the location of the trajectory

end points with observations obtained at the same time. The second half of the chapter explores how the retrieved height can help to refine the SO₂ mass estimates from volcanic eruptions. One question I seek to answer is how much the height retrieval alters mass estimates as opposed to the standard OMI products that use pre-defined, fixed plume heights. Mass estimates from other sensors and literature are provided for comparison. The summary of the results of this dissertation and suggestion for future work are provided in Chapter 5.

Chapter 2: Analyzing Sulfate Wet Deposition Trends in the Eastern United States

2.1 Introduction

Sulfate wet deposition negatively affects surface and ground water and certain ecosystems through changing chemical characteristics of soil [U.S. EPA, 2003; Butler et al., 2001; Likens et al., 2002]. While posing a major pollution problem in the second half of the 20th century, both species have shown a definite downward trend in the eastern United States. The reason for their decreases is undisputed –initiatives such as the various phases of the Clean Air Act [U.S. EPA, 2015; Butler et al., 2001] and introduction of flue gas desulfurization in coal power plants have led to drastic reductions in sulfur emissions and the subsequent SO_4^{2-} formation, especially in regional hotspots such as the Ohio River Valley. In addition, the monitoring of these pollutants and deposition increased, in part due EPA’s Acid Rain Program [U.S. EPA, 2002]. Sulfate is produced chemically in the atmosphere mainly through the oxidation of SO_2 . Sulfur dioxide’s lifetime in the atmosphere strongly depends on the oxidation rate. The lifetime was shown to vary from up to 48 hours in winter to around 13 hours in summer based on a study performed with GEOS-Chem model simulations and observations [Lee et al., 2011]. The deposition of SO_4^{2-} does not necessarily occur near the emission site or in the same areas with high SO_2 concentrations. The wet deposition process is driven by precipitation and air flow patterns in addition to sulfur chemistry. It is important to quantitatively attribute changes in emissions to those in the deposition trends over downwind areas in order to characterize benefits of regulatory controls.

The advent of satellite remote sensing has greatly aided in quantifying amounts of various pollutants. One remote sensing instrument used for obtaining of SO_2 column amounts is

OMI, onboard the Aura satellite. This product has proved useful in locating SO₂ sources and observing their changes in emissions [McLinden et al., 2016; Li et al., 2017a]. For example, a study using the previous OMI SO₂ product detected a 40% decline in SO₂ near the largest coal power plants in the United States between 2005-2007 and 2008-2010, consistent with regulations on emissions [Fioletov et al, 2011]. The latest OMI product is based on a new retrieval technique [Li et al., 2013; 2017b] that further reduces retrieval noise and artifacts, allowing for better detection of sources. A study using this new OMI SO₂ products demonstrates good correlation ($r = 0.91$) between reported emission rates and OMI-estimated emissions, and sources with emissions greater than 30 kt/y can be detected [Fioletov et al., 2015], as compared with 70 kt/y from the previous OMI products. Another study [Krotkov et al., 2016] indicates that from 2005-2015, OMI column amounts of SO₂ decreased by up to 80% in the eastern United States due to stricter pollution control measures.

The wet and dry deposition of SO₂ and its secondary SO₄²⁻ aerosol product are a significant environmental issue, especially downwind of the source areas. In particular, acid deposition is harmful for tree health, can cause damage to crops, and can alter soil chemistry by depleting plant nutrient cations and increasing acidity [Bell, 1986; Driscoll et al., 2001]. Much of the aerosol formed from gaseous pollutants gets deposited in areas downwind of sources. A number of studies have been published attempting to link the wet deposition with emissions and atmospheric transport processes. Samson et al. [1980] performed a meteorological analysis based on air trajectories and found little relationship between SO₄²⁻ and sulfur emissions. However, a later study by the same group showed that the two could be explicitly linked in several areas while being unrelated in others [Brook et al., 1994]. Wet deposition was shown through modeling to have a statistically significant relationship with SO₂ emission reduction due to policy

changes in the late 1980s and early 1990s [Shannon, 1999]. An earlier study also estimated separation distances and atmospheric transport for atmospheric SO₂ and SO₄²⁻ [Shannon, 1997]. In the late 20th century, locations in upstate New York, despite their relatively low local SO₂ concentrations, experienced acid rain and deposition problems. Emission reductions upwind have been found to have a linear relationship with SO₄²⁻ aerosol concentrations in several locations in the area [Dutkiwicz et al., 2000]. The study used NOAA Hybrid Single Particle Lagrangian Integrated Trajectory (HYSPLIT) model [Stein et al., 2015] to track air trajectories to identify major source regions of SO₄²⁻ in Ontario and the Ohio River Valley. In particular, lakes in the Adirondack region in upstate New York have shown decreases in SO₄²⁻ concentrations and reasonable correlation ($r^2 = 0.58$) between SO₂ emission in the eastern United States and wet deposition changes downwind, at Whiteface Mountain and Huntington Forest [Driscoll et al., 2003]. Estimating the potential source regions of the sulfate deposition is especially important in cases where acid rain can be caused by pollution from different countries. For instance, environmental problems relating to acid rain near the U.S-Canada border have led to debates on the sources of the acid rain between the two countries. This ultimately led to the 1991 U.S-Canada Air Quality Agreement [Roelofs, 1993].

Several more recent works have also focused on how meteorology plays a role in aerosol transport and deposition. One such study incorporated methods such as the Positive Matrix Factorization (PMF), Conditional Probability Function (CPF) and the Potential Source Contribution Function (PSCF) to attribute sources of PM_{2.5} in the Pittsburgh, PA area through trajectory modeling [Peckney et al, 2017]. In another study [Begum et al, 2002], the PSCF method was employed to identify the source location of a Quebec forest fire from PM_{2.5} measurements. An earlier study modeled the transport of sulfur species from source to the

receptor sites in Southern California [Gao et al, 1993]. Other localized trends in particulate matter have also been addressed, particularly in the I-95 corridor of the Mid-Atlantic region. A study incorporating modeling and observations showed contributions from both regional and local sources within 100 km of the Baltimore-Washington, D.C. corridor and that the local contribution to PM_{2.5} mass varies seasonally, from >60% in winter to <30% in the summer [Chen et al., 2002].

Similar studies were performed for sites in Wisconsin, where enhanced SO₄²⁻ and nitrate concentration originated from air arriving from potential sources near the Ohio River [Heo et al., 2013]. Recent work incorporated observations of satellites such as GOME and SCHIAMACHY along with GEOS-Chem transport model to constrain global reactive nitrogen deposition rates and trends since 1996 [Geddes et al., 2017].

While a considerable number of studies have quantified source-receptor relationships in regard to atmospheric deposition for multiple sites, less work has been done with more recent deposition data and satellite data. This study aims to take advantage of the availability of OMI column SO₂ measurements, ground based SO₂ observations, and measurements of wet SO₄²⁻ deposition. Between 2005 and 2015, many sites in the eastern U.S. saw substantial reductions in wet deposition of SO₄²⁻. But it is not yet clear which sources of atmospheric SO₂ contributed most to these reductions in deposition and whether there is significant difference in between summer and winter. This study aims to shed some light on these important questions. The methodology and analysis presented in this study can be applicable to other areas, especially those experiencing significant pollution and deposition problems.

2.2 Methodology

2.2.1 Datasets

The Ozone Monitoring Instrument (OMI) has been providing remote sensing products of gaseous pollutants, including sulfur dioxide since 2004. As described in Chapter 1, the SO₂ column amount is retrieved using an algorithm based on principal component analysis of UV radiances measured by the satellite [Li et al., 2013]. The SO₂ data from OMI has been used in a number of previous studies, particularly those on SO₂ emission source regions. For the purposes of this study, Level 3 column SO₂ data [NASA GES-DISC, 2017] was used to derive the trend over the eastern United States for the period of 2005-2015. Level 3 data is a gridded dataset with spatial resolution of 0.25° latitude by 0.25° longitude and is limited to scenes with relatively small cloud fraction (< 0.3). To reduce the impacts of extreme values on the average trend, negative outliers ($< -2\sigma$) were filtered out in the calculation of the averages, following Zhang et al. [2017]. In addition, to remove the effects of positive extreme values likely caused by transient volcanic plumes, values greater than the 99th percentile of the SO₂ values in the U.S. domain were excluded from the averaging process as well [McLinden et al., 2016]. The OMI column SO₂ ten-year trend (Figure 2.1a) was obtained by calculating the three year running mean from 2005 to 2015 and deriving to a linear trend with an annual time step. This trend also highlights the areas that have experienced reduced emissions in the last ten years.

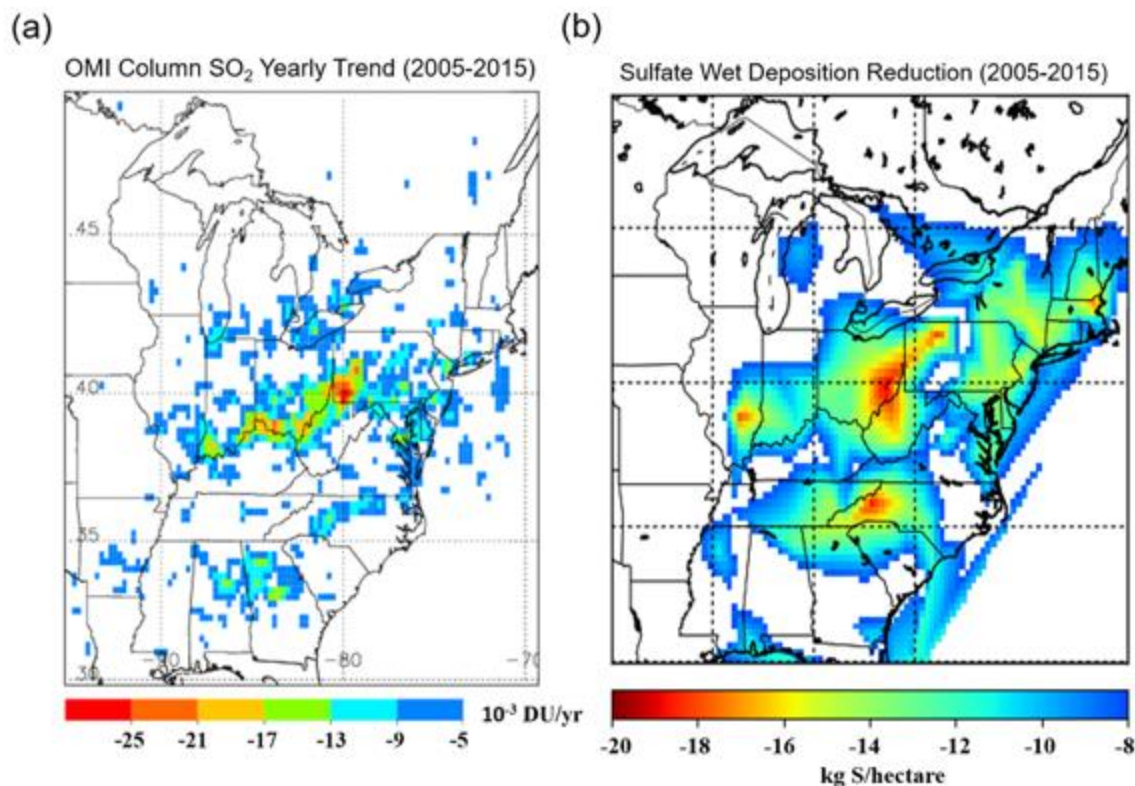


Figure 2.1: (a) Annual trend in OMI Column SO₂ in the eastern United States calculated using yearly averages, from 2005 to 2015 (b) Change in wet SO₄²⁻ deposition between 2005 and 2015 over the same domain and time period, based on NADP deposition measurements.

Sulfate wet deposition data was obtained from the National Atmospheric Deposition Network (NADP). This network, consisting of over 150 monitoring sites nationally, collects rainwater samples on a weekly basis and analyzes them for various chemical species [Lamb et al, 2000]. Total SO₄²⁻ wet deposition is estimated annually for each station, as end of year totals with the deposition given in units of kg S/ha. Due to the non-gridded nature of the data, I interpolated the annual deposition to a regular grid, using Inverse Distance Weighting (IDW) and Kriging interpolation methods, shown to be most efficient for calculating special deposition patterns [Qu et al, 2016]. A ten-year trend and net reduction (Figure 2.1b) in SO₄²⁻ over the entire U.S. domain (CONUS) was calculated for each grid box in the same way as for the SO₂, to

provide SO₂ and SO₄²⁻ trend values for each grid square. While the NADP does not have ideal coverage, there are sufficient active sites in the Eastern U.S. to create a gridded field with spatial interpolation (Figure 2a), albeit with some error.

Another dataset employed in this study is from the Environmental Protection Agency (EPA) Air Quality System (AQS). This network provides hourly and daily ground-based measurements of SO₂. For the purposes of this study, AQS data was used in the PSCF analysis, described later in this section. Dry deposition, a variable percentage of total SO₄²⁻ deposition [Vet et al, 2013], is measured by the CASTNET network [U.S. EPA CASTNET, 2017]. Our primary focus in this study was on wet deposition, since wet deposition is more dependent on weather and precipitation tracks than is dry deposition. At sites in our domain west of the Appalachians, dry deposition contributed >50 % of the S deposition, but east of the mountains wet deposition dominated [NADP, 2016] for the study period. The deposition trends discussed in the methodology and results will refer to wet deposition unless otherwise stated. Lastly, I used some hourly SO₂ emission data obtained from power plant continuous emission reporting systems (CEMs) through the EPA [U.S. EPA, 2017].

2.2.2 Trajectory Analysis

A trajectory analysis was used to diagnose the possible origins of the air containing elevated amounts of SO₂ at various sites in the Eastern United States. Airflow patterns revealed by this analysis can help to establish the link between the trends in SO₂ emissions and SO₄²⁻ wet deposition. The sites chosen for the trajectory analyses (Figure 2.2b) are in the AQS network with available SO₂ in-situ data, as well as a corresponding NADP site nearby with deposition data. The five sites chosen were 1) Hackney, OH [81.670° W, 39.632° N], 2) Beltsville, MD

[76.817° W, 39.028° N], 3) Akron, OH [81.469° W, 41.0635° N], 4) South Fayette, PA [80.167° W, 40.3756° N] and 5) Wilmington, DE [75.558° W, 39.7394° N]. All of these sites had a significant downward trend and at least 50% decrease in deposition between 2005 and 2015 (Table 2.1). A site in upstate New York [74.500° W, 43.4336° N], Piesco Lake, was also considered due to a considerable downward 10-year SO₄²⁻ wet deposition trend in the region, however the in-situ SO₂ concentrations were too low to perform a meaningful trajectory analysis. The SO₂ at this AQS site only exceeded 2.5 ppb 28 days in the winters and not once in the summers over a three-year period.

Table 2.1: The 2005 and 2015 sulfate wet deposition amounts for the six initial case sites. Values were obtained directly from the annual NADP dataset for each site.

Site	SO ₄ ²⁻ Wet Deposition 2005 (kg S /ha)	SO ₄ ²⁻ Wet Deposition 2015 (kg S /ha)	% decrease 2005-2015
Hackney, OH	26.70	8.76	67.2
Akron, OH	22.08	11.08	49.8
Beltsville, MD	18.83	6.93	63.2
Wilmington, DE	19.41	5.57	71.3
South Fayette, PA	25.82	9.82	62.0
Piesco Lake, NY	19.04	7.93	58.3

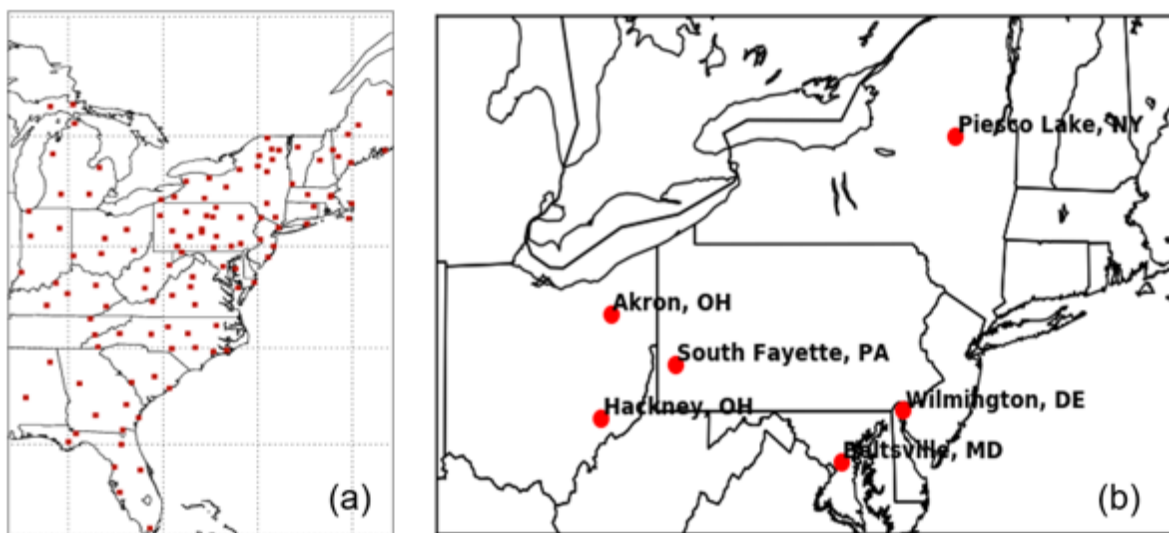


Figure 2.2: Locations of (a) observing sites in the NADP network, shown by the red squares and (b) AQS sites initially chosen for the main analysis. These sites are in reasonably close proximity to NADP sites. Refer to the text for the exact coordinates. The site in New York was removed from the analysis due to SO₂ concentrations frequently below the detection despite having a considerable sulfate wet deposition trend.

The HYSPLIT trajectory model from NOAA (Stein et al, 2015) was used to calculate back trajectories. Three-day back trajectories were calculated each day using archived Eta Data Assimilation System (EDAS) meteorological data at 40 km resolution. The HYSPLIT model runs were initialized daily at 18Z near the overpass time of the satellite. The initialized height was kept constant in the model runs at 500 m above ground level. A climatology of back trajectories was obtained for each site by running daily 72-hour back trajectories for three summers (JJA) and three winters (DJF), in the period 2006-2009. This period was selected because larger downward trends in column SO₂ and SO₄²⁻ wet deposition occurred in 2005-2010 than in 2010-2015, as shown by trend maps for the two time periods (Figure 2.3). However, changes in the average seasonal large-scale flow pattern are unlikely to be strongly dependent on the period selected.

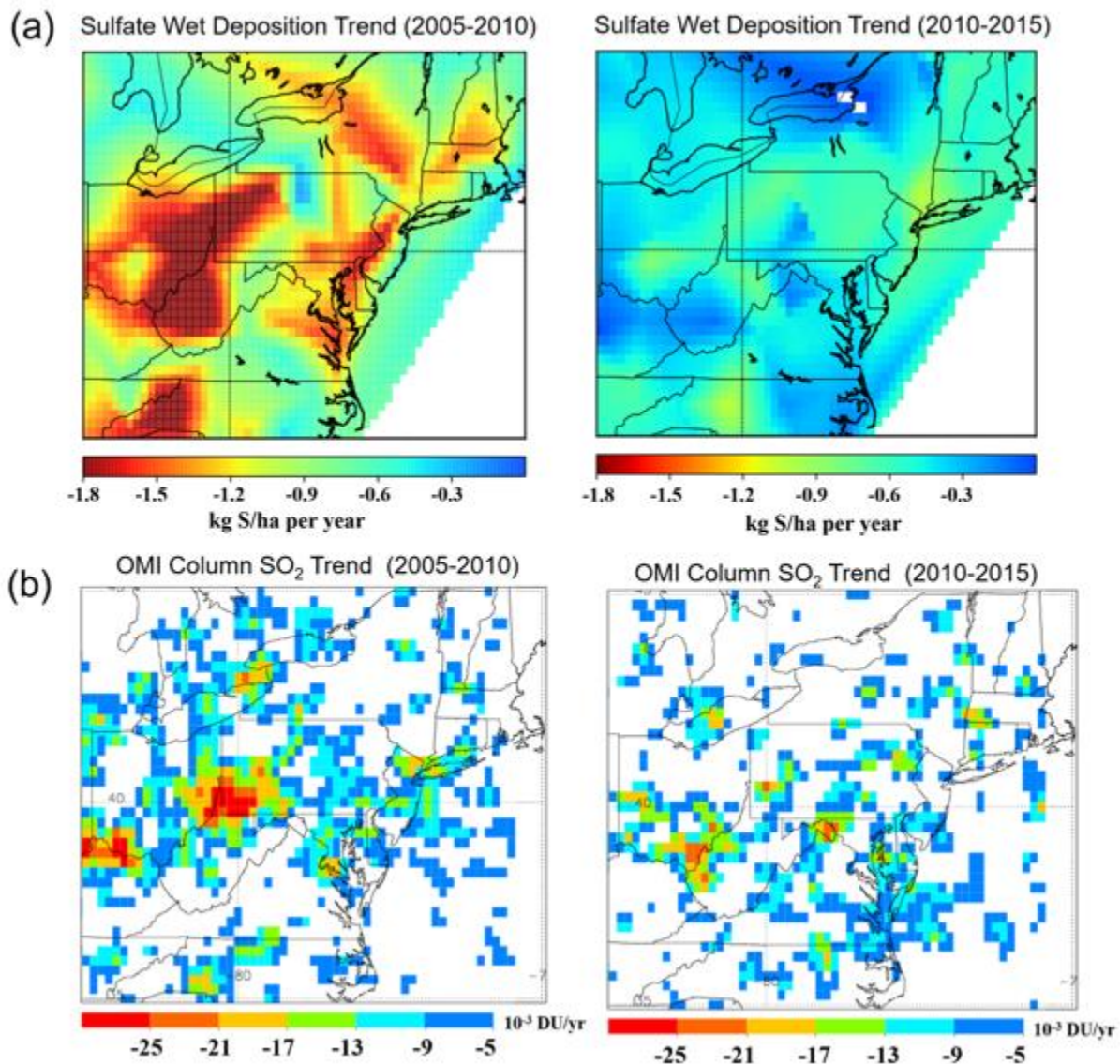


Figure 2.3 : Annual trend for a) NADP sulfate wet deposition and b) OMI Column SO₂ for 2005-2010 (left) and 2010-2015 (right). The improvements in column SO₂ occurred at sites closer to the sources than did the improvements in deposition, but the trends are consistent.

2.2.3 Potential Source Contribution Analysis

The need for a trajectory and PSCF analysis stems from the fact that the spatial correlation between wet SO₄²⁻ deposition and OMI column SO₂ trends is overall fairly weak across the entire domain. The low R² coefficient (0.036) showed poor correlation between the

two normalized trends (Figure 2.4) at the Beltsville, MD location. The method used to normalize the trends will be discussed further in section 2.4.

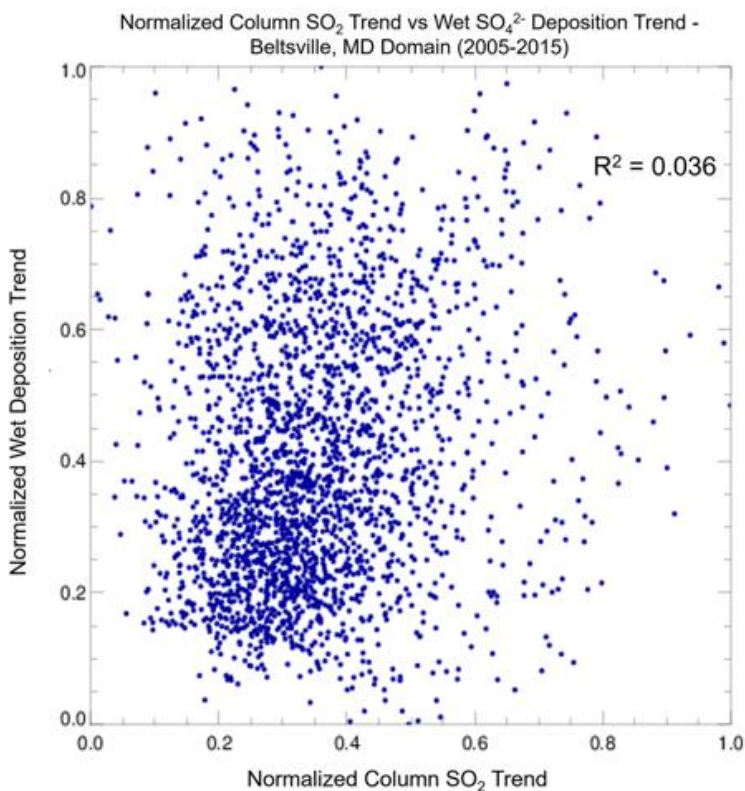


Figure 2.4: A scatter plot of the normalized trends for the Beltsville, MD site domain. Each point represents a grid box in the domain with a unique normalized SO₂ and SO₄²⁻ wet deposition trend value. The bounds for the domain are [88.875°, 73.875° W] and [35.125°, 45.125° N].

To link the trends, characteristic air patterns for a given location are needed to understand the trends occurring in those locations. The calculated trajectories were obtained for the purpose of calculating the probability of high concentrations of SO₂ coming from a given grid box in the domain. The Potential Source Contribution Function (PSCF) is defined as the number of trajectories passing through a grid box carrying an amount of SO₂ exceeding a set threshold (m) divided by the number of total trajectories going through that same grid box (n). Thus, each grid box would have its own PSCF value, between 0 and 1. The function is expressed as:

$$PSCF_{ij} = \frac{m_{ij}}{n_{ij}} \quad (2.1)$$

The subscript ij denotes a single grid box on the grid domain. The domain over which the function was calculated was ± 5 degrees latitude and ± 7.5 degrees longitude from each site. The domain size and location were chosen based on the typical distance covered by trajectories within 72 hr. Based on the arithmetic mean and median concentrations of SO_2 recorded at each of the sites over the three year period (Table 2.2), I chose a value of 5 ppb as the SO_2 threshold for all of the base cases except for the winter South Fayette, for which the threshold was set at 7.5 ppb. These thresholds were kept constant throughout the entire analysis. Even though using a sulfate deposition value as the threshold would be more accurate, the SO_2 measurements are available on a daily time frame, consistent with the trajectory calculations. The SO_2 at the site, when used with the PSCF can still be a useful parameter to find general source regions of sulfur pollution, and given its relatively short lifetime is a reasonable option considering the ground data availability. A simple weighting scheme was assigned for the PSCF calculation to remove the influence of low sample size [Pollisar et al, 1999]. The weighting factors were added in order to eliminate the sample size issues, or occurrences of low values of n_{ij} . For grid boxes with $n < 8$ trajectories, the PSCF value is multiplied by a weighting factor of 0.07. Similarly, for grid boxes with 8-16 and 16-24 trajectories, I used a weighing factor of 0.45 and 0.7, respectively. The weighting factors were assigned values of < 1 in order to maintain a value of PSCF between 0 and 1. These new values are the weighted potential source contribution functions (WPSCF) and were calculated for each of the five sites for JJA and DJF. The weighted scheme is arbitrary and varies across literature, however the one used here is very similar to a study to identify potential source regions of $\text{PM}_{2.5}$ in Beijing using the same type of back-trajectory analysis [Zhang et al, 2015]. Aside from using HYSPLIT to acquire trajectories and graphics generating scripts, I used

a GIS-based program called Trajstat to analyze the trajectories and PSCFs. This software was originally produced for statistical analysis of air pollution data and includes basic geographic map layers and trajectory file conversion capabilities [Wang et al, 2009].

Table 2.2: Mean and median winter SO₂ concentration as measured by the five AQS sites over the 2006-2009 period. These metrics were used to choose a threshold value for the PSCF analysis.

Site	Mean(ppb)	Median (ppb)
Akron, OH	5.15	4.3
Hackney, OH	6.62	4.9
S. Fayette, PA	7.62	6.9
Beltsville, MD	4.35	6.3
Wilmington, DE	5.14	4.8

2.2.4 Normalized Trends

To factor in the effect of the PSCF on the trends, I transformed both trends to the same, normalized scale. The SO₄²⁻ wet deposition trends were normalized to a scale of 0 to 1 with the grid box having the highest downward trend assigned a value of 1 and the grid box with the highest positive trend assigned a value of 0 (Eq. 2.2). The cases of an upward 10-year trend in the deposition were very few in the eastern domain and thus did not influence the outcome. The column SO₂ trend over the entire domain was also normalized the same way. In general, the equation used for normalizing a trend is :

$$x_{ij,norm} = \frac{x_{ij} - \min(X)}{\max(X) - \min(X)} \quad (2.2)$$

Where x is the normalized SO_2 or SO_4^{2-} trend value for a given grid box, X_{ij} is the raw trend for the same grid box and X is the set of gridded trend values for the entire domain. Multiplying the normalized trends result by the PSCF produces a relative product value that describes the relative contribution of the air coming in that grid box to the trend. A grid box with both a high PSCF and large downward wet deposition trend would indicate that air arriving from there has seen significant reductions in sulfur over the years, thus contributing to the decrease in wet deposition at the receptor locations. To relate the NADP trend and WPSCF to OMI observations, the normalized 10 year trend in column SO_2 was added into the calculation:

$$z_{ij} = \text{norm}(\text{SO}_2 \text{ Trend}) \times [\text{WPSCF} \times \text{norm}(\text{SO}_4^{2-} \text{ Trend})] \quad (2.3)$$

This product value helps to identify, for a given receptor site, upwind source locations that not only frequently influence the site through transport and also have large decreases in SO_2 emissions between 2005 and 2015 according to OMI. All three factors in Equation 2.3 are necessary since the deposition trend, emissions and transport are accounted for. Using only the normalized SO_2 trend would only indicate contributions to decreasing SO_2 at the site, rather than deposition. Likewise using only the normalized SO_4^{2-} wet deposition trend, the influence of emission reductions is removed from the contribution. Thus equation 2.3 is instrumental in producing an “overlap” of all three components. A percent contribution was then calculated for each grid box by dividing each individual grid box value of z_{ij} by the sum of all boxes in the domain. Thus this new value expresses the normalized contribution of a particular grid box to the SO_4^{2-} wet deposition trend at the AQS or NADP site, relative to the domain. This provides a quantitative assessment of the trend data relationship.

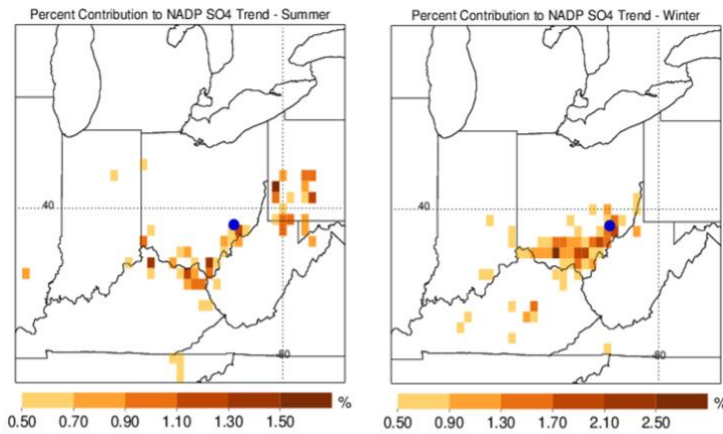
$$\% \text{ Contribution} = \frac{z_{ij}}{\text{sum}(z_{ij})} \times 100\% \quad (2.4)$$

2.3 Results

2.3.1 Percent contribution

This section describes the qualitative and some quantitative aspects of the grid boxes that contribute to wet deposition trends at five different sites. Figures 2.5 and 2.6 show grid cells in the domain with a color representing the final percent contribution value calculated with equation 2.4. I aim to show the specific grid boxes which had the most contribution in the domain to the wet deposition trend at the receptor site, as well as the cumulative contribution at various distances from the site through summations of the percent contribution values.

(a) *Hackney, OH*



(b) *Beltsville, MD*

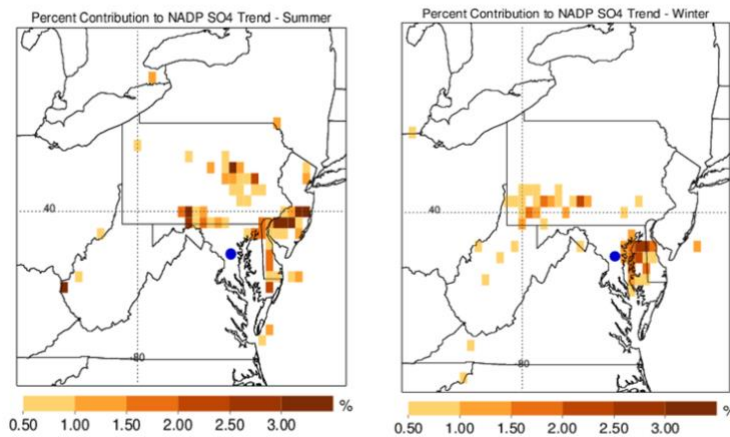
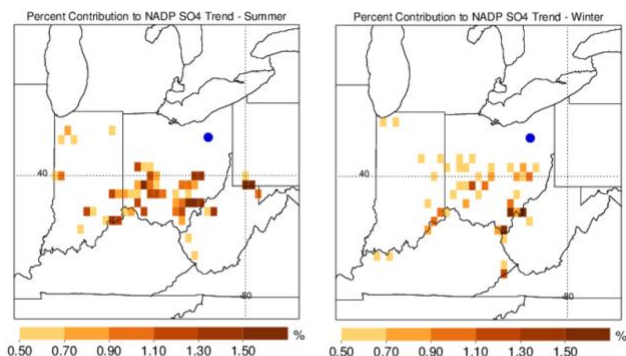
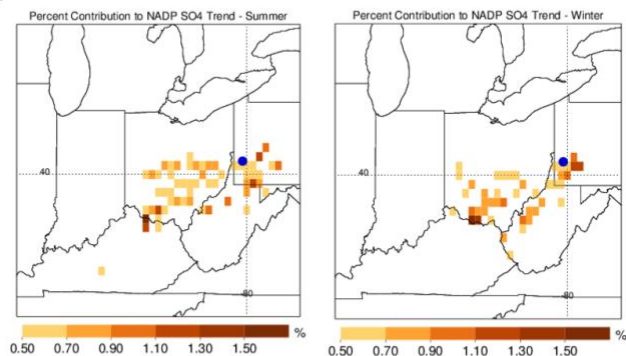


Figure 2.5: Percent contribution for each grid box in the domain with only values above 0.5%. Shown for (a) Hackney, OH and (b) Beltsville, MD sites in JJA (left) and DJF (right). The observation sites are marked with a blue dot.

(a) *Akron, OH*



(b) *South Fayette, PA*



(c) *Wilmington, DE*

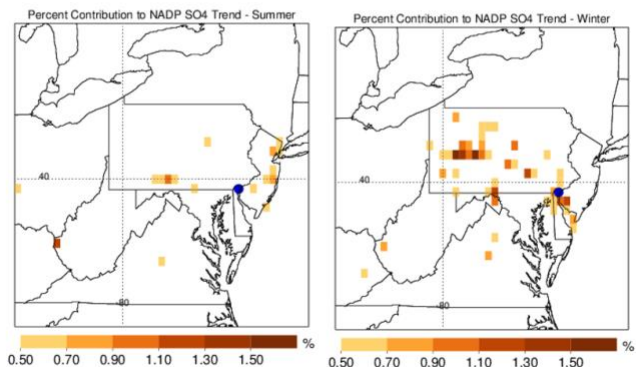


Figure 2.6: Percent contribution for each grid box in the domain with only values above 0.5%. Shown for (a) Akron, Ohio, (b) South Fayette, PA and (c) Wilmington, DE AQS sites in JJA (left) and DJF (right). The observation sites are marked with a blue dot. Note that only values greater than 0.5% are colored.

Hackney, OH

Due to its proximity to numerous sulfur emitting coal-fired power plants, the Hackney, OH AQS site shows high concentrations of SO₂ with average daily value of around 7 ppb and often exceeding 20 ppb in winter. The corresponding NADP site for this area is in Caldwell, OH (Site ID OH49), ~18 km away. I would expect similar characteristic deposition and trajectory patterns for the two locations given the flat terrain and proximity to the same SO₂ sources. In wintertime (DJF), wet deposition trend at the Caldwell NADP site is driven by the dominant southwesterly flow and high outputs of emissions upwind near the Ohio River (Figure 2.5a). The observed annual wet deposition at the Caldwell site decreased from 23.35 kg S/ha in 2005 to 8.76 kg S/ha in 2015 according to the NADP dataset. The wet deposition has significant year-to-year variability (Figure 2.7), however, the overall 10-year trend from 2005 to 2015 was downward.

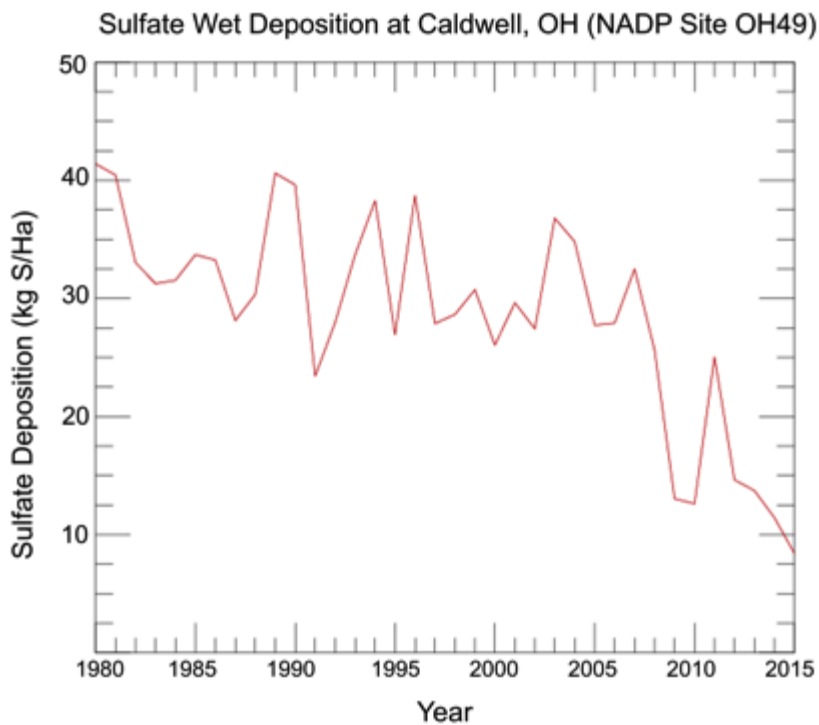


Figure 2.7: Sulfate Wet Deposition amounts at Caldwell, OH NADP site, shown as a time series from 1980 to 2015. The plotted data is from the NADP network at the OH49 site [39.7928 N, 83.5311 W]

Qualitatively, the area with the colored grid boxes in southern Ohio largely contributed to the decreasing deposition (Figure 2.5a). In summer (JJA), major areas in southwestern PA with large SO₂ columns somewhat contribute to the observed trend at the Hackney site, however less so than the sources along the Ohio River. The trajectory climatology for this site (Figure 2.8) shows a clear seasonal change in direction trajectories indicating that emission reduction in the west have likely contributed to the majority of the observed trend at the site.

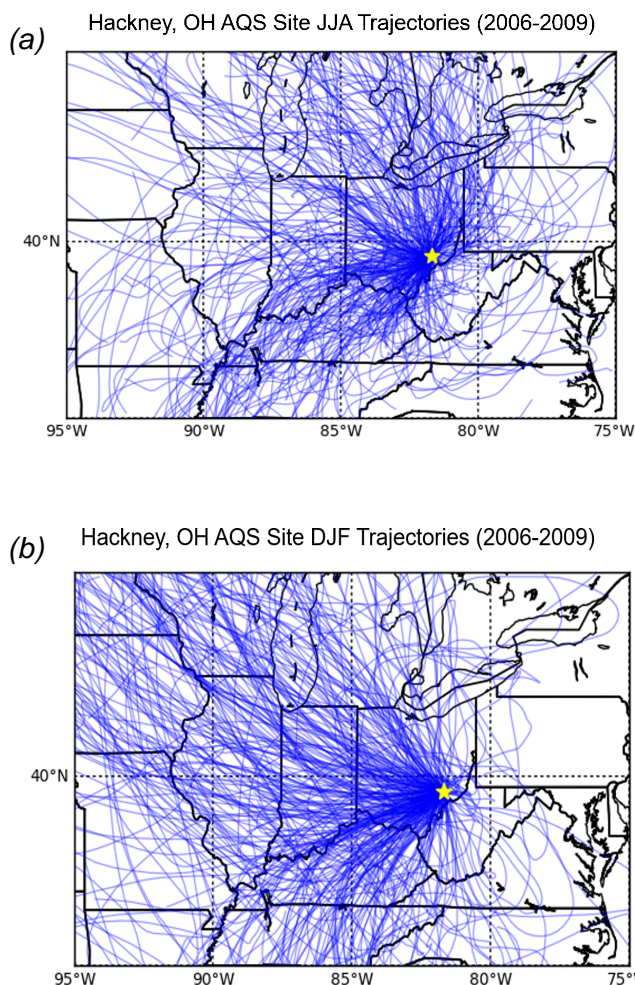


Figure 2.8: Map of (a) summer (JJA) and (b) winter (DJF) trajectory climatology for 2006-2009 at Hackney, OH. The yellow star shows the location of the site and the blue lines are the individual 72 hour back trajectory for each day, initialized at 18Z using the HYSPLIT model.

Beltsville MD

The Beltsville, MD site experienced a downward SO_4^{2-} wet deposition trend, especially in the years 2008-2012, and has two primary regions that contributed to the 10-year decrease. The Southwest PA region shows the greatest cumulative percent contribution which implies that wet deposition has dropped due to the decrease in sulfur emissions in Pennsylvania. However, there is also a signal to the east of the site in Maryland in the PSCF and contribution map (Figure

2.5b). While the dominant trajectory is from the northwest in winter, air can occasionally arrive from the east in both seasons. In summer, wind direction is more variable compared to winter, as indicated by the trajectories from HYSPLIT (Figure 2.9). Note that in the summer case, there are grid boxes with a relatively large percent contribution in southern New Jersey. While there were several coal power plants in that area before 2015 that have since been closed, the features in Figure 2.5b are more likely due to sampling issues since SO₂ and sulfate deposition amounts are lower than in winter. Just before the turn of the decade in 2010, Maryland's Healthy Air Act led to cuts of sulfur emissions of 80-85% from levels in the early 2000s [He et al., 2016]. While most of the contribution is due to decreased emissions to the west, it is probable that local emission controls have also played a role in decreasing SO₄²⁻ deposition in the general vicinity. The case for this site will be further investigated in section 2.3.3.

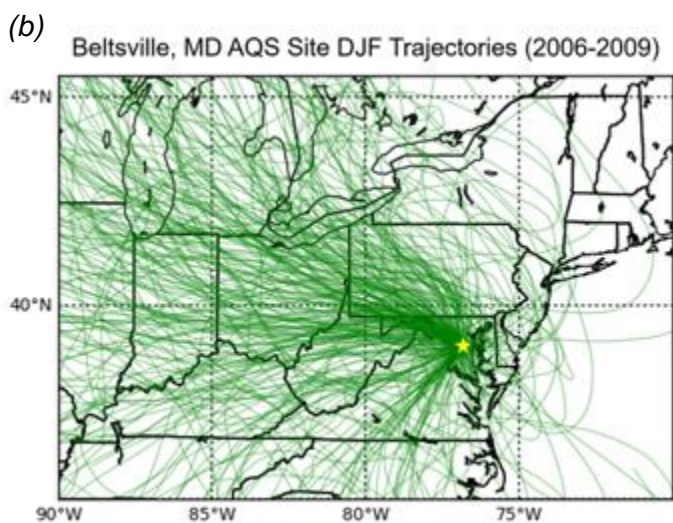
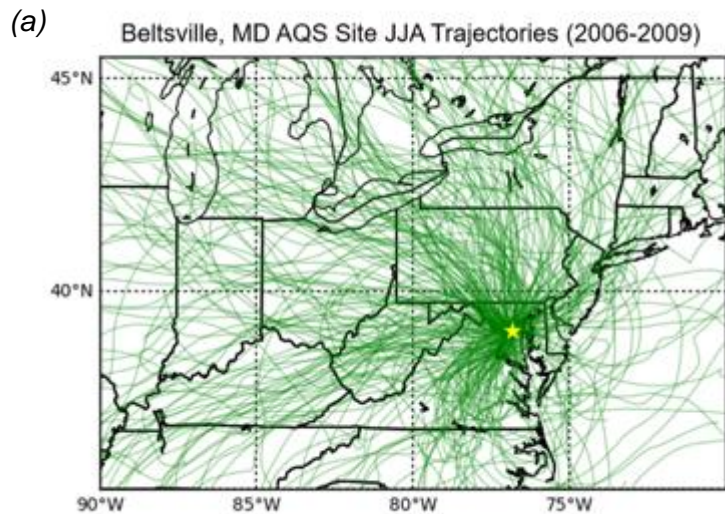


Figure 2.9: Same as Figure 2.8 but for Beltsville, MD AQS site. The trajectories are denoted by green lines in this figure

Akron, OH

Sources to the south and southwest dominate the wet deposition trend for the Akron, OH (Figure 2.6a). Most of the grid cells with a non-negligible percent contribution (greater than 0.5 %) are located near major SO₂ sources, approximately 100-300 km away from Akron in both winter and summer. The percent contributions show fewer grid boxes with contributions over 1.5% in

winter as the contribution is spread out over larger number of grid boxes, especially those further away. This is reflected by higher emissions, generally higher wind speed and longer trajectory distance within the 72 hours in wintertime. In summer months there is also signal from southwest PA with over 1.5% contribution for two grid cells in that region.

South Fayette, PA

The AQS site in South Fayette, PA had the highest median in-situ SO₂ amounts of the five sites reported in the 2006-2009 period for both winter (~7.0 ppb) and summer (~3.5 ppb), whereas in Hackney those median amounts were 5.4 and 2.7 ppb respectively. Sulfate deposition is affected by local sources, but the PSCF analysis also shows elevated SO₂ concentrations arriving from the east and southwest, near the sources along the Ohio River. During summer, there is slightly more contribution from the east, indicating a shift from a predominantly western zonal flow that occurs during winter. However, the seasonal difference in the contribution appears to be smaller than at other sites. The highest percent contributions in both seasons are from southern Ohio and just to the east of the site (Figure 2.6b), which indicates the presence of sulfur emission sources. In this sense, the site is quite similar to the patterns in Hackney, OH, except it is more affected by the local power plants to the east in PA.

Wilmington, DE

For the Wilmington, DE site (Figure 2.6c), the region contributing the most in winter to the deposition trend is from upwind in Pennsylvania, which is home to several large power plants. As shown by OMI, the region had a strong decrease in column SO₂. Given the winter trajectory pattern, it follows that any reductions in Pennsylvania benefitted the Wilmington area in terms of deposition amounts. In summer, there is not much signal from any particular area, with isolated grid boxes in the New York area and in southern PA. It is reasonable to assume that most of the

decrease in annual SO_4^{2-} wet deposition were due to large decreasing trend in winter SO_2 concentrations over upwind areas to the west. While there may have been some minor summer contributions as well, their magnitude was not as great as in winter. This shows an absence of SO_2 source near the site and that a stronger wintertime flow pattern is needed to have impacts on the deposition trends.

2.3.2 Contribution Distributions by Distance

I extended the analysis in the previous by calculating the total percentage contribution to trend observed at a receptor site from all grid boxes within a certain distance from the site. Distances of 50, 100, 200, 300, 400, 500 and 1000 km were used in the analysis. The calculation was performed by creating a circle with a radius of the distance from the site and summing up the contribution of all grid boxes that fall within the circle. This process leads to cumulative distributions of total contribution moving away from the site. This would help in diagnosing if the wet deposition at the site is primarily driven by local or upwind sources and the direction from which the sulfur is arriving at the site. I calculated a cumulative contribution for two sites with significant climatological and geographical differences, Beltsville (Figure 2.10) and Hackney (Figure 2.11), for summer and winter seasons.

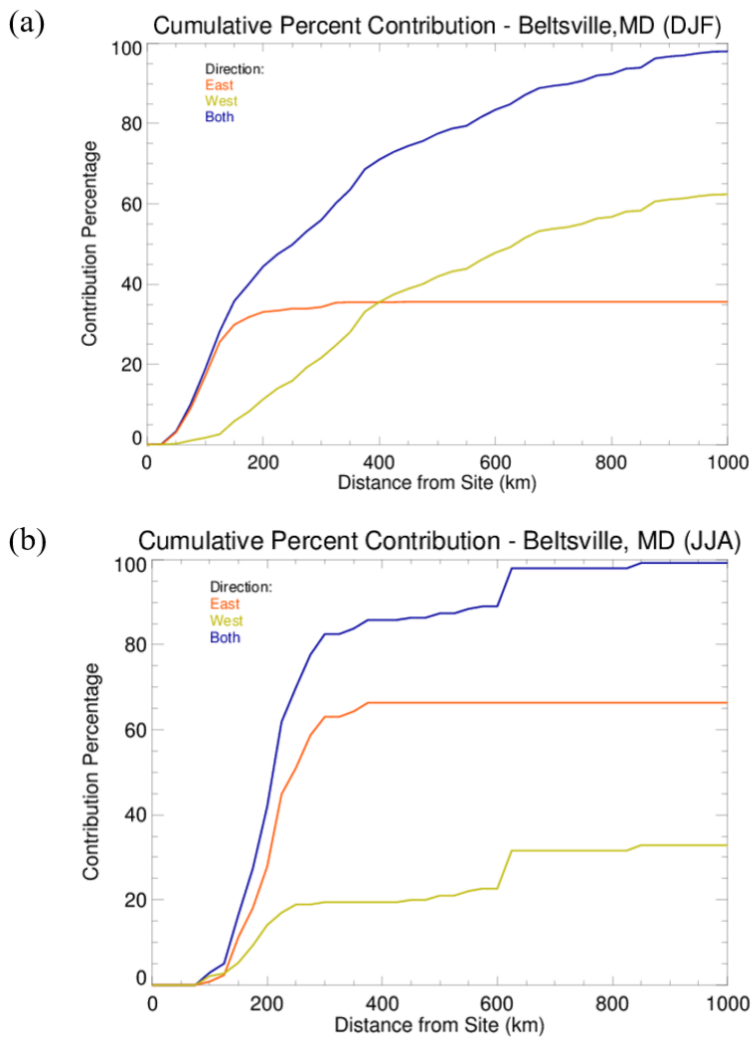


Figure 2.10: The cumulative percentage of contribution to the SO₄²⁻ wet deposition trend at the Beltsville NADP site, from areas within a given radius from the site (x-axis) for (a) winter and (b) summer. The orange, green and blue lines represent contributions from locations with a longitude east of the site, west of the site and all locations within the radius respectively.

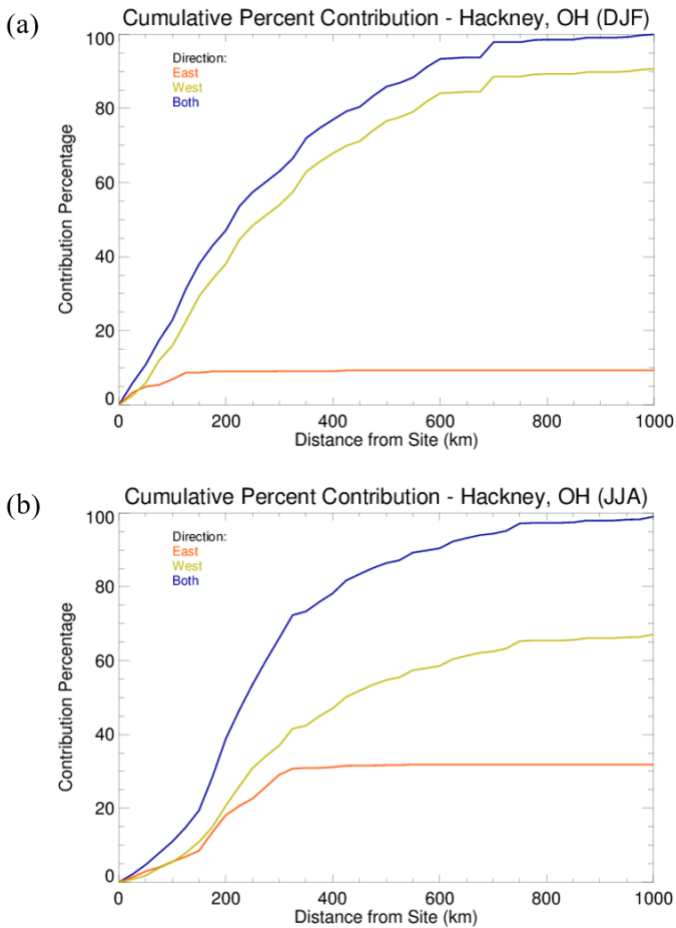


Figure 2.11: Same as Figure 2.10 but for the Hackney AQS site.

Beltsville, MD

For the Beltsville site, half (50%) of the sulfur contributing to the ten-year wet deposition trend is linked to SO₂ observed within a 300 km radius in winter and 200 km in summer (see Table A.1 and Table A.2). However, more contribution comes from locations over 300 km away in winter (44%) than in summer (17.5 %), showing that the lifetime and transport distances are generally greater in winter. The lower in-situ SO₂ amounts in summer than in winter are consistent with the fact that the largest SO₂ emitting power plants in the domain are more than 300 km away. Higher contribution values come from several grid boxes closer to the site in the Beltsville, MD case (within 100 km), yet the accumulated contribution in the southwest PA

region has arguably more effect on the deposition trend. This is evidenced by sources more than 300 km to west of Beltsville, MD that contribute more than 50% of the SO_4^{2-} . The result shows the benefit in reducing emissions upwind in western PA and eastern Ohio, as the decrease has led to a downward deposition trend in addition to improved SO_2 levels in the second part of the study period. In summer, 83% of the contribution comes from within 300 km, with roughly 63% of this coming from the east of the site. This indicates that summer transport distance is short and pollutants are less likely to reach from beyond 500 km away as they do in winter.

Hackney, OH

In winter, while the total contribution from within 300 km (63%) is similar to summer for this site, 54% of it is from the west (see Table A.3). For summer, roughly 66% of the contribution is from within 300 km of the site, with 29% of it from the east and 37% from the west (see Table A.4). While more of the contribution is from the west, the eastern component indicates that some of the SO_4^{2-} originates from areas to the northeast of the site in PA in addition to areas to the southwest of the site. Areas within 100-200 km from the site, contributed to about 24% and 27% of the SO_4^{2-} wet deposition trend in winter and summer respectively, meaning the emission source within that radius are more or less contributing the same in both seasons relative to the rest of the domain. This is a different characteristic from Beltsville, MD since for Beltsville more contribution came from further distances in winter and was not as greatly affected by SO_2 sources within 200 km of the site. Due to proximity of this site to some of the sources, it is possible that the SO_2 from these sources was not resolved in the trajectory analysis with only 40 km resolution of the meteorology data. Over all distances, the western component dominates in both winter and summer with roughly two thirds coming from the west in winter and 90% in

summer. This indicates the dominance of the climatological westerlies over source proximity and deposition processes.

2.3.3 Impact of Maryland Healthy Air Act

Evidence exists that a significant amount of Maryland's sulfur pollution originates upwind in Pennsylvania and Ohio River valley. However, it is interesting to assess the impact of local statewide regulations on the improvements in pollution in the ten-year period. The Brandon Shores power plant is one of the biggest emitters of sulfur dioxide in Maryland, especially before the enactment of the Healthy Air Act of 2010. The plotted average monthly emissions show that the facility cut its SO₂ emissions by over 80% post 2009 (Figure 2.12).

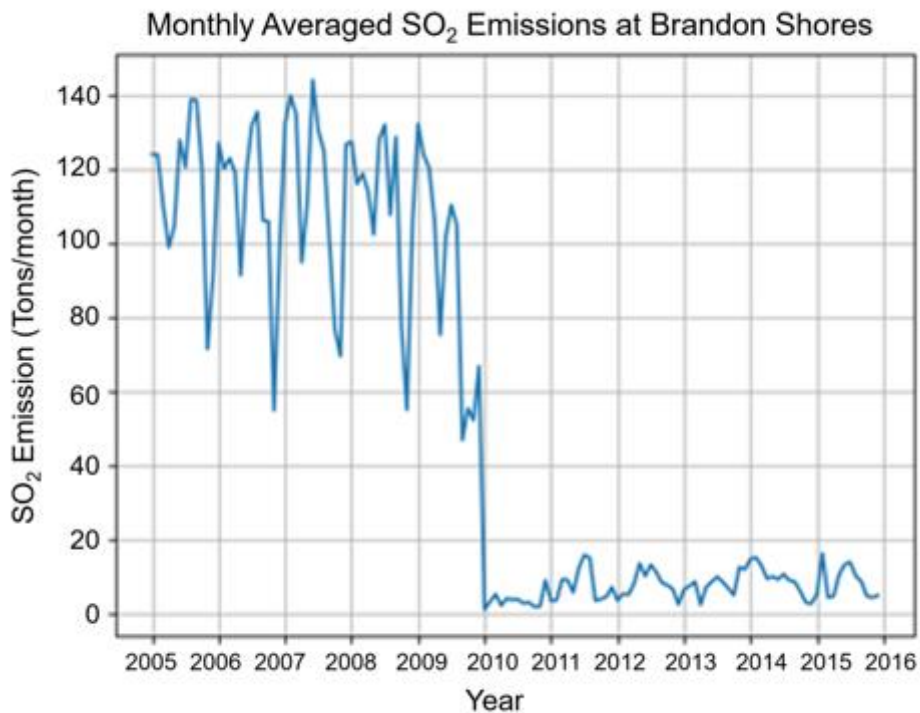


Figure 2.12: Monthly averages of hourly SO₂ emissions from the Brandon Shores power generating facility, located just to the south of Baltimore, MD. The data were obtained from Continuous Emission Monitoring Systems (CEMs) and are distributed by EPA's Air Markets Program database.

Maryland state emission inventories (Figure 2.13a) also show roughly 80% drops in SO₂ emissions between 2005 and 2015 in the fuel combustion sector, which includes power plant emissions. There is a 78% drop in 2007-2012 and 45% drop for 2005-2009, indicating that Maryland cut more of its emissions in 2008-2012. At the same time, emissions have been decreasing consistently in Ohio and Pennsylvania, as well as nationally (Figure 2.13b). The trends for SO₄²⁻ and SO₂ are also of greater magnitude in 2005-2010 than in 2010-2015 (Figure 2.3), which aligns with emission trends and the enactment of the Healthy Air Act.

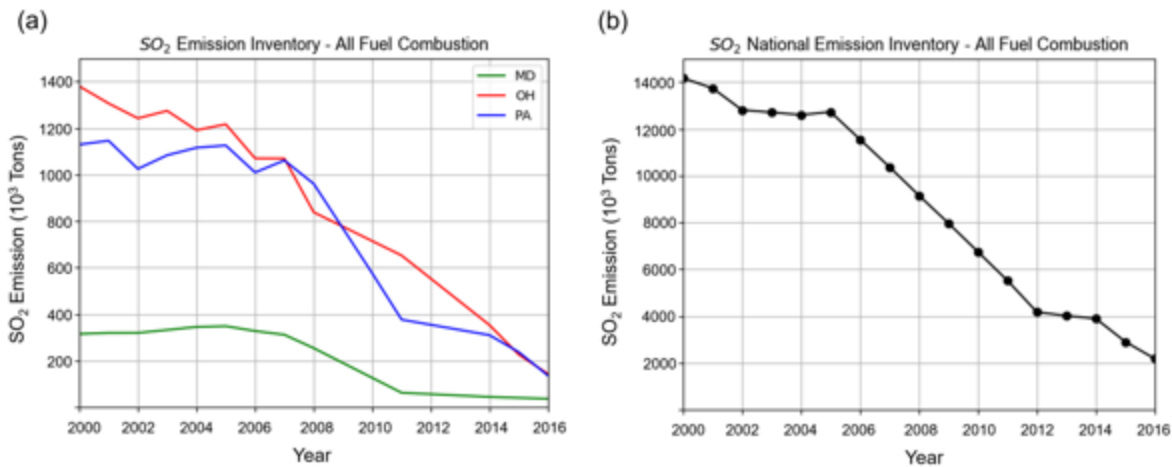


Figure 2.13: The SO₂ emission inventory for (a) three states: MD, PA and OH and (b) the entire United States. Only the total values for the fuel combustion sector, which includes primary power plant emissions, are included. This sector is the dominant portion of the inventory and accounts for over 80% of the total. Emission inventory data can be found on the EPA Emission Inventory site: <https://www.epa.gov/air-emissions-inventories/air-pollutant-emissions-trends-data>

Using the same PSCF analysis method as above, I was able to identify contributions to the SO₄²⁻ sulfate wet deposition trend for 2008-2012 by using the trend and PSCF corresponding to this time period only. As seen in Figure 2.14, there is noticeably larger total contribution from areas close to the site than farther away. There is also a difference between the original 10-year case

and this four-year time period in that the grid boxes directly to the northeast (Baltimore area), contribute to the decreasing trend slightly higher, from 1-1.5% in the 10-year case to 2-3% for 2008-12. This indicates that the state rule helped in somewhat reducing deposition in the short term.

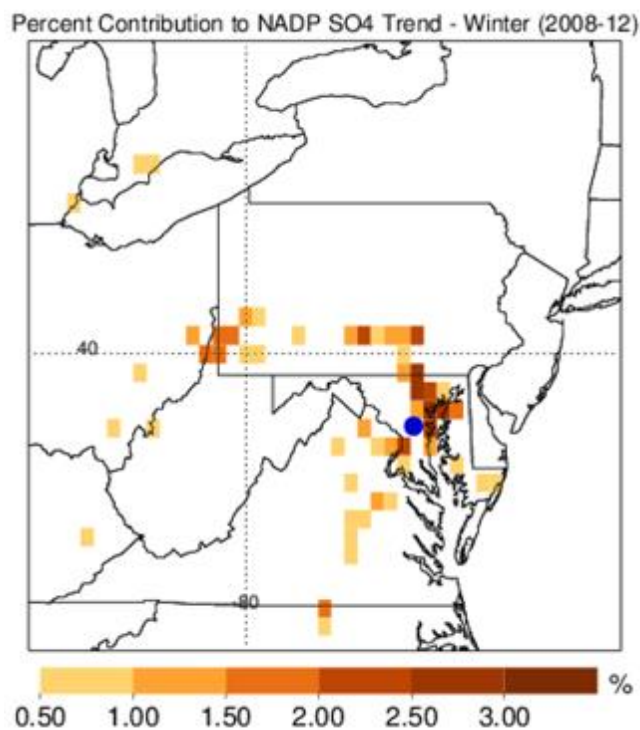


Figure 2.14: Percent contribution to the Beltsville, MD winter wet deposition trend for 2008-2012. The same procedure was used as in the other maps, except with a 2008-2012 winter trajectory climatology and PSCF

This result can also be related to the specific dry and wet deposition amounts occurring in Beltsville over the years. The data in Table 2.3 indicates that dry SO_2 and SO_4^{2-} deposition have decreased overall from 2005 to 2015. The decrease is better seen in the SO_2 than SO_4^{2-} between the first and second 5 years. The effect of cutting emissions at Brandon Shores has clearly decreased local dry deposition of SO_2 . The result is less obvious in the dry SO_4^{2-} , although by 2015, the deposition has dropped by almost 50%, from 1.12 to 0.59 kg S/ha. The fraction of total

sulfur deposition due to dry deposition of SO₂ has fallen by roughly a factor of two over this decade, consistent with greater partition into sulfate [Shah et al., 2018]. According to Figure 2.15, the steepest trend in wet deposition occurred from 2008-2012. The wet deposition end-of-year total for 2012 decreased to 8 kg S/ha from around 20 kg S/ha, reported at the end of 2009 (Figure 2.15).

Table 2.3: Flux of dry SO₂ and SO₄²⁻ at the Beltsville, MD site in the CASTNET network with the annual NADP wet deposition totals. The flux value can be seen as dry and wet deposition of SO₄²⁻ at the site. Note that several years of dry flux data were missing in the dataset and that there is no available measurement for wet SO₂ flux.

Year	Dry SO₂ Flux (kg S/ha)	Dry SO₄ Flux (kg S/ha)	Wet SO₄ Flux (kg S /ha)
2005	7.547	1.857	17.42
2007	4.296	1.777	15.49
2008	4.268	1.426	15.72
2009	3.112	1.005	19.36
2010	2.227	1.126	9.34
2011	1.361	1.048	12.04
2013	1.009	0.785	5.95
2014	1.410	0.706	7.14
2015	1.071	0.588	6.46

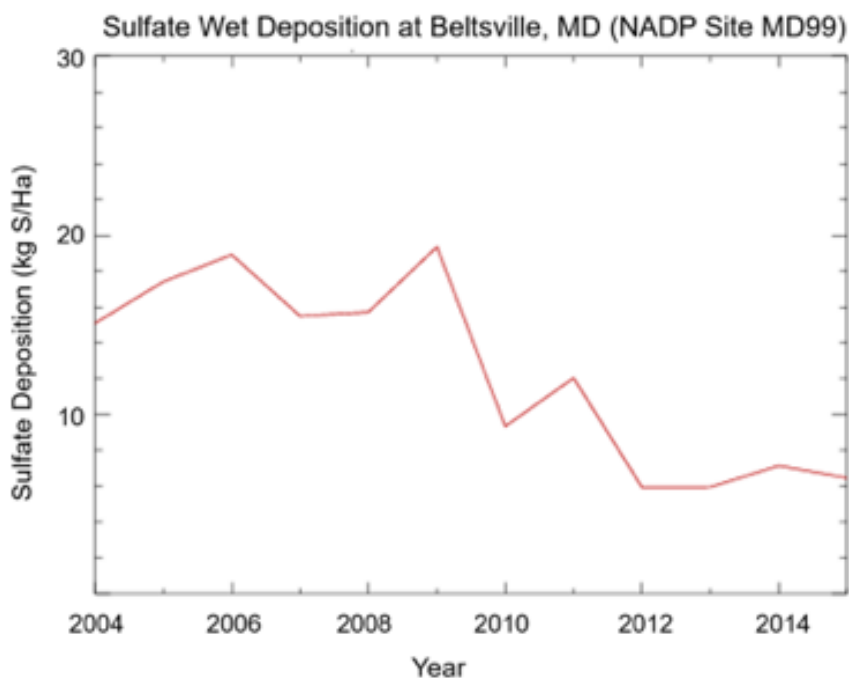


Figure 2.15: Sulfate Wet Deposition amounts at Beltsville, MD, shown as a time series from 2004 to 2015. The plotted data is from the NADP network at the MD99 site.

However, wet deposition is largely driven by the precipitation patterns and consequently more closely related to air trajectory climatology. Given that only less than 25% of back trajectories arrive from east of the site in winter, it is difficult to conclude that the drop in local emissions was the dominant factor in the overall decreasing trend. Yet the effect is non-negligible and may have certainly played a role as the steepest slope indeed occurred between 2009 and 2010. Thus, I can speculate that the signal associated with the contribution values to the east and northeast of the site as well as the increase in percent contribution for the 2008-2012 four year period, are not anomalies or artifacts of the method, but significant characteristics of the contribution to the wet deposition trend in Beltsville between 2008 and 2012. The local and statewide emissions likely only affected the short-term trends in deposition given the drastic changes in emissions, rather than the long term deposition changes over a 10 year period. The

latter is likely driven by a systematic drop of emissions on a larger regional scale and consistent trajectories from the northwest. Lastly the SO₂ lifetime is qualitatively estimated from the contribution maps. In general, there is indication that lifetime is less than 1 day in the summer, while in winter the SO₂ gets carried 100-200 km more especially for the eastern sites. The latter indicates a longer SO₂ lifetime in excess of 1-1.5 days in winter. This is consistent with the SO₂ lifetimes of 13 h and 48 h for summer and winter respectively found by Lee et al. and may be due to seasonal differences in oxidation rates; Shah et al. [2018] reported only 18% of SO₂ was regionally (over the eastern US) oxidized to SO₄²⁻ in winter, but 35% of summer. As shown previously, SO₂ and SO₄²⁻ deposition trends can appear in geographically different areas. Locations that have drastically reduced their sulfur emissions can still have SO₄²⁻ deposition problems due to upwind sources and likewise can benefit from the reduction of emissions from those areas. Thus, both local and regional pollution controls are not only important for air quality but for the environment since air trajectory patterns control the transport and deposition of chemical species.

2.4 Discussion

Although the methodology presented in this study was used consistently for all sites, it did not come without limitations or systematic errors. In this section I discuss potential sources of error and uncertainty stemming from the methods and factors that were difficult to constrain in this study.

2.4.1 Quantitative Error Estimates

From the trend calculations, error statistics showed around ± 0.1 kg S/ha /yr on average for the SO₄²⁻ wet deposition trend for grid cells with relatively high trend magnitudes. The actual error across the domain varied based on the magnitude of the NADP site distribution. Likewise, the

OMI SO₂ trend calculation carried a ± 0.001 to ± 0.0025 DU/yr error with greater uncertainties for grid boxes with low SO₂ amounts or low trends. These errors were estimated by repeating the trend calculation with slight variation based on the uncertainties in OMI SO₂ and interpolated NADP data, with the difference between the calculations being the trend error. Interpolation of irregular spaced data such as the case of NADP sites (Figure 2.2a), inherently carries uncertainty due to varying site coverage and the interpolation method itself. The uncertainty was in the 10-20% error range for more than half the grid boxes in the domain, while areas with less observing sites contained higher percent error. The error analysis was performed through validation of annual wet deposition output from the Community Multi-scale Air Quality (CMAQ) model. These interpolation errors, while having potential impacts on the results, could not be avoided due to limitation of the NADP observing network.

The error in the percent contributions results directly from the uncertainties in the normalized trends and the PSCF, as those are the two components used in the calculation (Eq. 3). Uncertainties in the PSCF can originate from trajectory calculations and from different possibilities of choosing the threshold. Changing the threshold by ± 1 ppb resulted in only 25-30 of the 2400 grid boxes in the domain having a PSCF change of greater than 0.1, as determined by a sensitivity test. Therefore, the overall result across the domain is not significantly affected by this parameter. The calculations of the trajectories inherently contained errors as a result of limited temporal and spatial resolutions of the model reanalysis meteorological data. However, given the spatial resolution of the OMI instrument, the resolution of the meteorological data was appropriate. I can still estimate roughly 20% relative uncertainty, which is proportional to trajectory distance [Stohl, 1998]. In regard to the normalized trends, the grid cells with high trends were estimated through sensitivity tests to have an uncertainty on the order of 20-30%,

accounting for OMI and NADP data uncertainty in addition to the normalized trend calculations. In grid boxes with smaller trends, the uncertainty is higher because their weight is closer to 0. However, the areas with low SO_2 and SO_4^{2-} trends generally do not strongly impact the results presented. The total uncertainties in the percent contribution can be estimated to have an upper limit 30-40% in most grid cells of the domain, as an upper limit. This result was obtained by combining the square error of the PSCF and the two normalized trends.

2.4.2 Other Limitations and Uncertainties

One big limitation in this study is the characteristics of wet deposition. Whether the SO_4^{2-} is being deposited or carried further downwind is dependent on nature of the trajectory and if precipitation occurred. Given the uncertainties in diagnosing rain or cloud formation events along the trajectory, I primarily focus on determining where deposition is highly decreasing along with an active flow pattern from trajectory analysis showing possible origins of SO_4^{2-} from nearby sulfur in the atmosphere. The trajectories are utilized as rough interpretations of air flow and to contribute to a seasonal climatology as shown in Section 2.2. Furthermore, HYSPLIT model parameters were rather simple in the sense that the model was not run at multiple times during the day or from different heights. I kept the constant initialization height of 500 m (above ground) which is a reasonable representation of mid boundary layer height. The back trajectories were only run once a day to match the temporal resolution of OMI and around the time the instrument would pass over the Eastern U.S to make measurements. Due to keeping the initialization time constant at 18Z and the height at 500 meters, there could have been error associated with analyzing the trajectories with respect to high SO_2 amounts since these can change due to weather patterns and within hours. Another limitation was the difficulty in distinguishing between sulfate coming from rainout or washout. With the nature of the data,

relative simplicity of HYSPLIT and lack of a chemistry model, there was not much information that could be gathered regarding the exact origin of the sulfate. However, I would expect a lot of the sulfur from power plants to be found closer to the surface than aloft, consistent with the 500 m trajectory initial height. Overall, chemistry related factors such as how much of the SO₂ is converted to SO₄²⁻ on a daily basis, how much is exported or removed through other pathways, and cloud processes could not be adequately captured by the method, therefore producing additional uncertainty in the results. Lastly, in many cases, the trajectories and the sulfur residing in the atmosphere can be influenced by local and smaller scale meteorology, in addition to the synoptic airflow. This can complicate the deposition and sulfur dioxide transport and can lead to a loss of important information regarding the connection between the two trends. These uncertainties are difficult to quantify but likely do not strongly impact the conclusions of the study, because the lifetime of SO₂ is relatively short and wet deposition is a main sink. Addressing complexities in the future, as opposed to this simplified approach, might gain additional insight on the link between the two trends.

There is also possibility of biases in precipitation collection based on the collector instrument used [Wetherbee et al, 2009]. Likewise, the OMI retrieval of SO₂ while much improved over the years, still has substantial noise and errors and could also have had a minor effect on the calculated trends. Another source of error in the method itself could be the low detection rates of SO₂ exceeding a threshold at a site. This happens during summer when the exceedance rate was low compared to winter, resulting in a more scattered PSCF and contribution maps. The resulting PSCF calculation (Eq. 1) would be fairly sporadic as the number of trajectories with SO₂ amounts above the 5 ppb threshold (m) would be low compared to the total number of trajectories (n). Since the calculated percent contribution was heavily

based on PSCF (Eq. 3), some grid boxes may not be represented as accurately, especially in JJA and at low SO₂ sites (Wilmington and Beltsville). It is important to note that these methods are mostly probabilistic, meaning I cannot discern concrete locations and say with complete certainty that a specific source contributed to the deposition changes.

2.5 Conclusion

In summary, the origin of pollutants in acidic wet deposition can be determined with a combination of in situ and satellite observations coupled to trajectory analysis. In this study I quantified the possible origin of SO₄²⁻ wet deposition for five sites in the eastern United States over 2005-2015. Each site showed characteristic source regions, generally consistent with seasonal wind patterns and observed SO₂ from OMI. Dominant sources depend on prevailing westerly winds, faster summer rates of SO₂ oxidation, and the synoptic conditions associated with precipitation. I also found that contribution changes pattern in direction and range with the season.

Reported emissions, observed concentrations, and monitored deposition all tell a consistent story – efficient scrubbing SO₂ in the eastern US has led to dramatic improvements in SO₄²⁻ wet deposition in the same region and benefits are generally seen within 500 km of the source. At the Beltsville, MD site in winter, about 2/3 of the SO₄²⁻ wet deposition originates from the west and 1/3 from the east, in keeping with the dominance of westerly winds. In summer, when SO₂ has a shorter lifetime with respect to oxidation to SO₄²⁻, closer emitters generally have a greater influence – the bulk of the deposition (80%) is due to sources < 300 km away; in winter this range is expanded to over 500 km. Nearby sources to the east do however have a substantive impact in colder months. The winter season is associated with a higher frequency of strong mid-latitude extratropical weather systems, which will produce periods of northeasterly winds off the

Atlantic Ocean and larger amounts of moisture and precipitation. Likewise, wind direction becomes more variable and, on average, weaker during the summer months. The region also experiences less precipitation during the summer, with the exception of heavy localized precipitation in convective storms. Nonetheless, 2/3 of the contribution (Table 4) is from east of the site, indicating the importance of source proximity and summer weather patterns. Both statewide emission controls and those upwind, out-of-state appear to have contributed to the decreasing SO_4^{2-} deposition trend. While higher contribution values come from several grid boxes within 100 km of the Beltsville site for the 2008-2012 period, the accumulated contribution in the southwest PA region has arguably more effect on the full ten year deposition trend overall. At the Hackney, OH site, the summer-winter difference is weaker, with 80% of the deposition from within ~400 km in both seasons, reflecting sources located closer to the site. Despite major SO_2 sources to the east, transport of sulfur from the west dominates, accounting for 2/3 of the deposition in the summer, and 9/10 in the winter. At this site, the prevailing wind pattern rather than proximity to emitters is the governing factor for this distribution.

Without the implementation of the appropriate methodology, such as the trajectory analysis used in this work, the regional SO_2 concentrations and deposition could not be adequately linked given their geographic displacement. The satellite data provide a consistent context for interpreting in-situ measurements and trajectory-based PCSF analyses, allowing me to identify major source areas that contribute to the observed decreases in SO_4^{2-} wet deposition.

Chapter 3: Volcanic SO₂ Effective Layer Height Retrieval for OMI

In this chapter, I present a newly developed volcanic SO₂ layer height retrieval for OMI. As stated earlier, the main motivation for this work is to obtain SO₂ height data quick enough for near real time operation, which has not yet been achieved for OMI. The volcanic SO₂ layer height is important because it can be used as a proxy for the ash plumes which can impact air traffic, as well as being an essential input for chemical and climate models. The retrieval algorithm I used was the Full Physics Inverse Machine Learning (FP-ILM) model originally implemented by Hedelt et al. [2019] for TROPOMI SO₂ height retrievals. The FP-ILM approach consists of two parts, the training phase, and the application (or operational) phase. The retrieval is fast due to the time consuming portions, the radiative transfer modeling and machine learning, being done in an offline training phase. The satellite radiance data is only introduced in the application phase, once the algorithm has been trained. This makes for a quick calculation from the BUV radiance inputs to the output (SO₂ layer height). The height results from this retrieval and comparisons with other instruments and previous studies are also presented in this chapter.

3.1 FP-ILM Methodology

The training phase of FP-ILM starts with the generation of a synthetic training dataset of top of the atmosphere (TOA) reflectance spectra from a radiative transfer model. This spectral dataset is then used to train a Multi-Layer Perceptron Regression (MLPR) NN model to predict the SO₂ layer height as an output. In the application phase, the trained inverse model is applied to real OMI radiance measurements. This inverse model is optimized from the training, and the predictions of SO₂ layer height based on the model are very fast as compared with the time-consuming RT calculations during the training phase. The main steps of the algorithm are shown in a flowchart (Figure 3.1) and discussed in detail in the next sections.

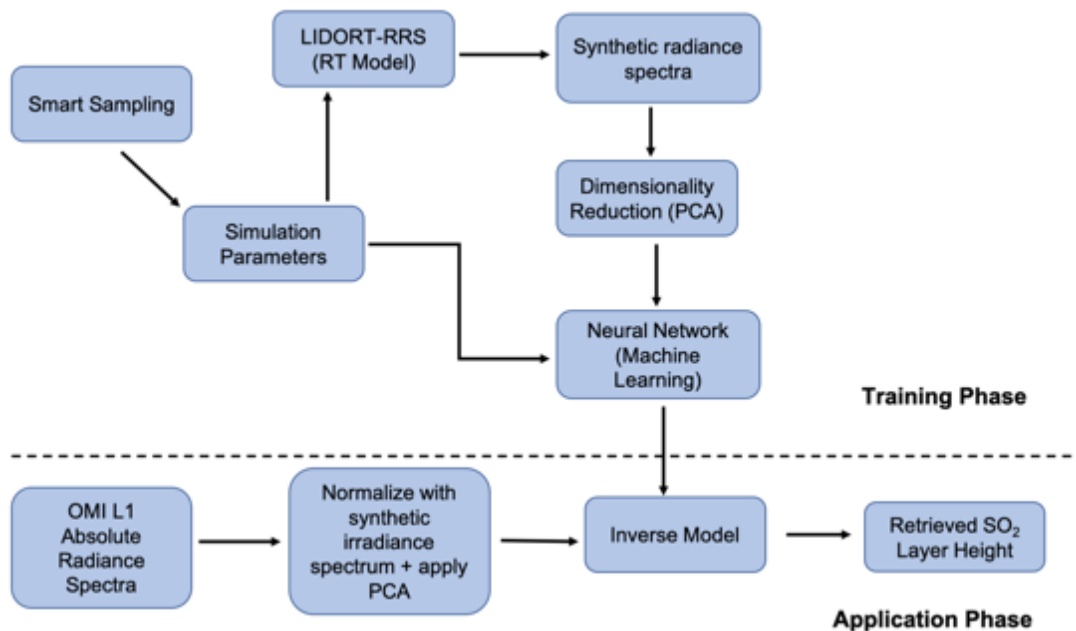


Figure 3.1: The flowchart of the FP_ILM methodology for retrieving OMI SO₂ Effective Layer Height. The steps above the dashed line are part of the training phase done prior to incorporation of OMI measurements. The application phase involves deployment of the trained model to the OMI radiance measurements to obtain estimates of effective volcanic SO₂ layer heights.

3.1.1 Forward Radiative Transfer Model

The first step in the training phase is to build a large data set of synthetic backscattered UV Earthshine radiance spectra from forward radiative transfer (RT) calculations. Earthshine spectra express the outgoing radiance from Earth’s atmosphere – they differ from solar spectra due to scattering processes by molecules and aerosols as well as absorption by various gases. These calculations are performed using the LInearized Discrete Ordinate Radiative Transfer (LIDORT) model with the rotational Raman scattering (RRS) capability [Spurr et al., 2008]. This version of the model treats first-order inelastic Raman scattering in addition to all orders of elastic (Rayleigh) scattering processes. Rotational Raman scattering occurs when a photon is scattered at lower or higher energy levels than the incident radiation. RRS cannot be neglected; it

is known to be responsible for the Ring effect [Grainger and Ring 1962], a spectral interference signature characterized by the filling-in of Fraunhofer lines and telluric-absorber features.

Allowing for RRS in the RT model leads to differences in calculated radiances compared to those made with purely elastic scattering, as characterized by the filling-in factor. This quantity is generally of the order of a few percent, consistent with estimates that 4% of the total scattering in the atmospheric is inelastic [Young, 1981]. Fundamentally the SO₂ layer height information can be retrieved by backscattered radiance spectra because the amount of scattering occurring in the overlying atmosphere is determined by the height of the volcanic SO₂ plume. This is demonstrated by comparing two otherwise identical RT calculations with different SO₂ layer heights (Figure 3.2a). At shorter wavelengths where Rayleigh scattering is stronger, there is less backscattered radiance for the case with higher SO₂ plume height, particularly at shorter wavelengths < 320 nm (Figure 3.2b). Likewise, the filling-in factor (Figure 3.2c) shows the importance of including RRS in the RT calculations as in some cases there can be 2-3% difference between the Raman and elastic calculations.

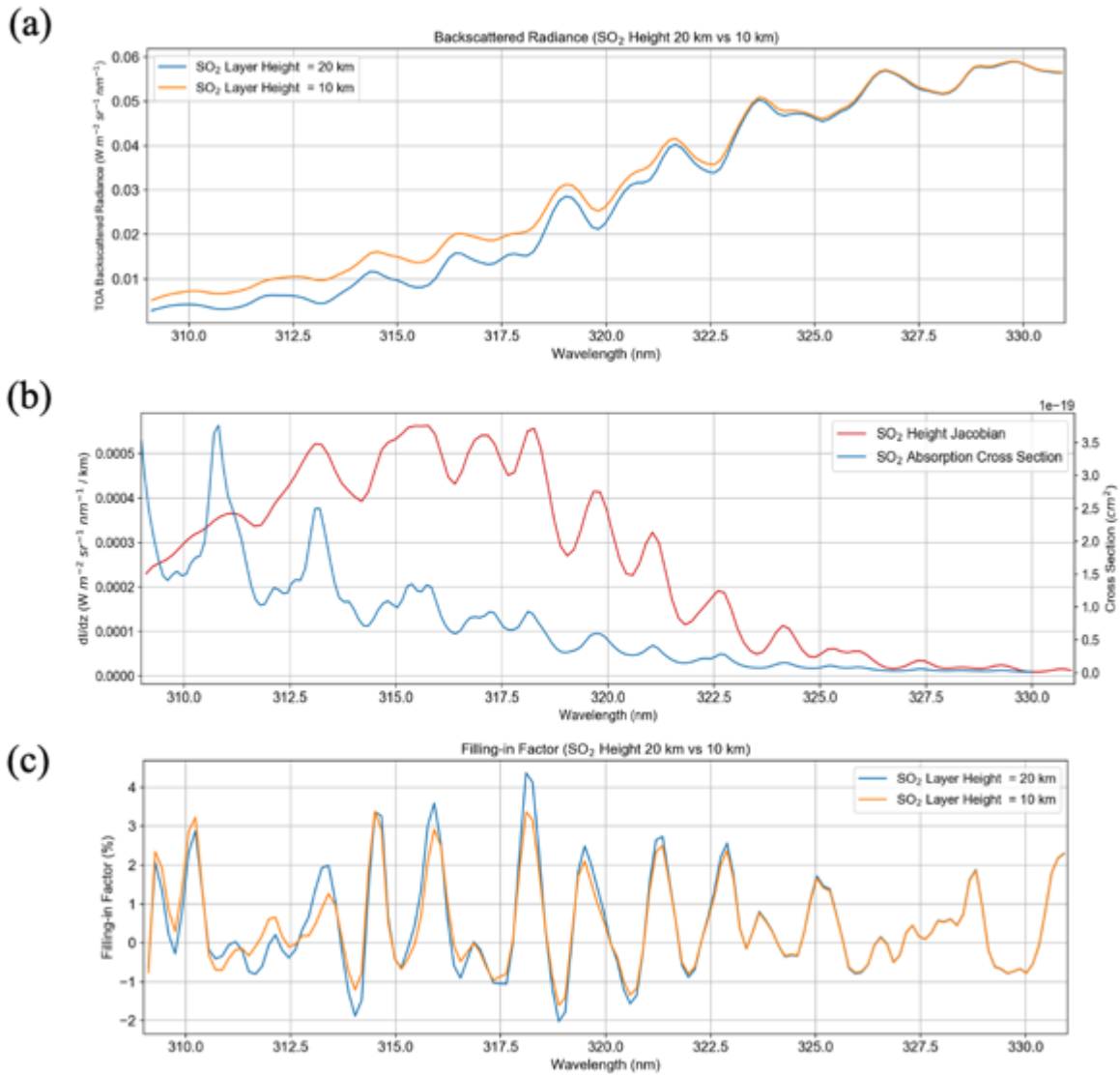


Figure 3.2: (a) Simulated top of the atmosphere (TOA) Earthshine radiances for two different SO_2 layer heights (10 km and 20 km) from the LIDORT-RRS model. Also shown: (b) the SO_2 height Jacobian (change in radiance per km between the two spectra) along with the absorption cross-sections of SO_2 for reference; (c) the filling-in factor. The filling-in factor is defined as the difference between the total and elastic-only radiance results, divided by the total radiance, expressed as a percentage. An SO_2 column amount of 200 DU was used in the two calculations and all other parameters were kept constant except for the SO_2 layer height.

All LIDORT-RRS calculations in this study were performed for the 310-330 nm spectral range, which captures strong SO_2 and ozone absorption features. The model is supplied with ozone [Daumont et al., 1992] and SO_2 absorption [Bogumil et al., 2003] cross sections,

atmospheric profile, ozone profile and a high resolution Fraunhofer solar irradiance spectrum. The atmospheric profile has 48 layers and contains a temperature/pressure/height grid from the standard US atmosphere, with an increased vertical resolution of 0.5 km below 12 km. The ozone profile is determined by the total column amount, latitude zone and month as specified in the TOMS V7 ozone profile climatology [Bhartia, 2002]. Using the input of total column amount, an interpolated profile is calculated based on two TOMS climatological profiles with fixed ozone amount values. In these simulations, surface ozone pollution would not have a significant effect on the profile due to a coarse vertical resolution in the atmospheric profile and the majority of the ozone being located in the stratosphere. A unique SO₂ profile is also calculated for each model simulation based on the input of the SO₂ plume height and SO₂ column amount parameters. It is assumed to be a Gaussian shape with a full width half maximum (FWHM) of 2.5 km, centered around the given height. This is a reasonable approximation for the average thickness of an SO₂ plume and slightly varying the FWHM did not impact the result of the calculation significantly. The solar spectrum is a re-gridded version of the high resolution synthetic solar reference spectrum [Chance and Kurucz, 2010], originally with a spectral resolution of 0.01 nm. The re-gridded version has a resolution of 0.05 nm, finer than that for OMI (0.16 nm sampling for a FWHM spectral resolution of ~0.5 nm). The advantage of using this reference spectrum over the instrument-measured irradiance is that only one set of calculations is needed; they can be applied to multiple instruments and instrument cross track positions without utilizing unique measured solar flux spectra for each situation. Using instrument-measured solar flux data may carry less potential error and be able to better handle issues with instrument degradation. However, the downside is that the inverse model would need to be re-trained whenever a new measured solar flux spectrum is used. Since I expect the

retrieval to be primarily sensitive to SO₂ absorption signatures, the radiative transfer calculation was performed for a molecular atmosphere with no aerosol scattering.

In order to obtain a large number of different spectra, eight key physical parameters were varied for the LRRS calculations. These parameters include solar zenith angle (SZA), relative azimuth angle (RAA), viewing zenith angle (VZA), surface albedo, surface pressure, O₃ column amount, SO₂ column amount and SO₂ layer height. The ranges of these parameters are given in Table 3.1.

Table 3.1: Ranges of the eight physical parameters varied in LIDORT-RRS for the synthetic spectra calculations.

Parameter	Range
Solar Zenith Angle	0-90°
Viewing Zenith Angle	0-70°
Relative Azimuth Angle	0-180°
Surface albedo	0-1
Surface pressure	250-1013.25 hPa
O ₃ VCD	225-525 DU
SO ₂ VCD	0-1000 DU
SO ₂ Layer Height	2.5-20 km

The number of calculations and the parameter sets for each simulation were determined through a smart sampling technique (Loyola et al. 2016). A selective parameter grid with sets of parameters for each simulation was established through the use of Halton sequences (Halton, 1962) in 8 dimensions. The calculations are continued until the moments of the output data, mean and median converged across all wavelengths. In total around 200,000 calculations were done to achieve sufficiently comprehensive sample size for the variation in the eight parameters across all rows of OMI. This sampling was done in order to ensure that 1) each set of parameters was unique and training data is diverse; and 2) that the sample size of the entire dataset is large enough for the machine learning application.

3.1.2 Data Pre-Processing and Machine Learning

After the RT calculations are completed, the spectra are convolved with the OMI instrument slit function. Since each cross-track position of OMI contains a unique slit function, the appropriate function was applied based on the VZA input for that particular calculation. The VZA ranges from 0-70° across all rows in the OMI swath, with the middle (nadir) rows having a VZA of close to 0. For each row, only spectra within +/- 3° of the actual VZA were convolved with the appropriate slit functions. In addition, Gaussian noise with a signal-to-noise ratio (SNR) of 1000 was added to the spectra. While the SNR of OMI tends to be lower [Schenkeveld et al., 2017], adding too much noise can greatly decrease performance of the machine learning (Table 2). The root mean squared error (RMSE) and mean absolute difference (MAE) between the SO₂ height from the RT calculation parameter sets and the height predicted by the neural network were used as metrics (see Section 3.1.3). At SNRs of less than 500, the performance starts to increasingly degrade. Between 1000 and 500 SNR, there is an increase of ~0.1 km in RMSE (Table 3.2). However, adding some degree of noise is necessary to account for errors in satellite instrument measurements.

Table 3.2: The RMSE and the mean absolute difference (km) of all data points in the independent test set after adding noise as indicated by different SNR values. All other parameters and input data were kept constant. SZA < 75 degrees and SO₂ VCD > 40 DU were excluded from the test set for these comparisons.

	No noise	SNR=1000	750	500	200	100
Mean Absolute Difference (y_known - y_pred) (km)	0.894	0.904	0.939	0.996	1.114	1.362
RMSE (km)	1.454	1.498	1.521	1.632	1.807	2.143
R-coefficient	0.988	0.985	0.983	0.980	0.972	0.955

Next, the PCA analysis was applied to the spectral dataset for each row, in order to extract the most significant features of the spectra, and to reduce dimensionality. Since each convolved sample consists of 142 wavelength points, the dimensionality of this problem becomes very large. However, PCA transforms each sample to a set of weights based on 8 principal components (PCs). These principal components explain 99.998% of the variance in the synthetic dataset (Figure 3.3). Including additional PCs does not add any significant value to the retrieval and may even lead to overfitting. Prior to starting the machine learning process, the dataset is split into a training subset (90%) and a testing subset (10%). The training subset is used for the neural network learning, while the testing subset only deployed verifying the performance of the network to predict the output.

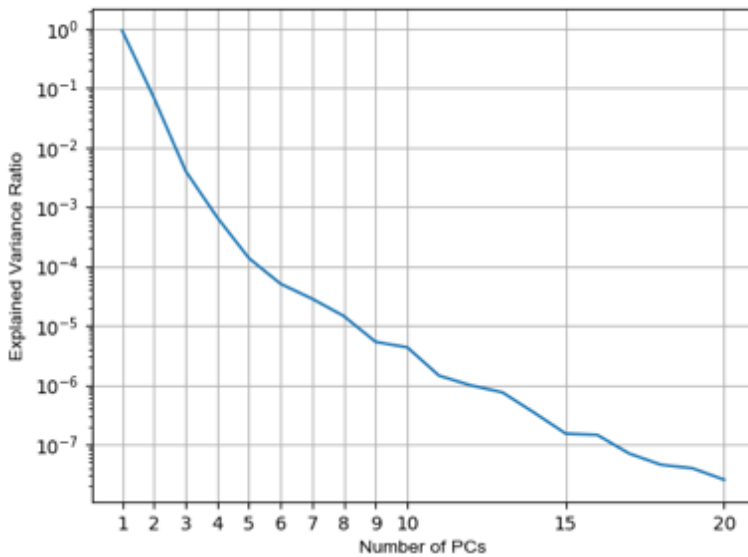


Figure 3.3: Explained variance ratio as a function of the number of principal components of the spectral dataset.

The 8 PCs, and selected parameters including the SZA, RAA, VZA, surface pressure and surface albedo were used as input for training a MLPR, which is sometimes referred to as a deep

neural network. This machine learning technique is especially useful for problems such as this one, as it can provide a nonlinear mapping between multiple numeric inputs and outputs. The output layer of the NN contains the effective SO₂ layer height. Column amounts of SO₂ were not included in the training or in the application stage because of the large dependency of column amounts on SO₂ layer height. The ozone column amount was included initially but was also excluded for simplicity, as it did not improve performance in the NN. To improve stability, the inputs (PC weights, SZA, VZA, etc.) and output (effective SO₂ height) are scaled between -0.9 and 0.9 according to the minimum and maximum of each input variable prior to input into the NN. In a NN, the input and output layers are connected by hidden layers containing neurons (also known as nodes). Each neuron is connected to others by a series of weights, by means of which the input data is passed to the next level as a weighted sum of all inputs. Inside the neural network, the Adam optimizer with a stochastic gradient descent algorithm (Kingma and Ba, 2015) is used to minimize the loss function, in this case the mean squared error (MSE) between the result of each iteration and the actual SO₂ layer height used to generate the synthetic spectral sample. With each iteration, the partial derivative of the MSE with respect to each node is calculated; this is used to update the weights. The training of a NN progresses by cycling through iterations of the entire training dataset, called epochs, until the training and validation MSE is minimized and there is no improvement to be obtained from further training. Throughout the training, the NN uses 10% of the training subset for validation to assess the performance with each iteration. This validation set is different from the independent test data that was set aside from training. The “tanh” (hyperbolic tangent) activation function is applied at the hidden layers to further increase stability in the NN. Other activation functions (e.g., ReLU and PReLU) were tested, however tanh was found to produce slightly better NN performance. There is also

considerable flexibility in the structure of the NN, in particular the number of hidden layers and nodes in each layer. The final configuration of the NN in this study includes 2 hidden layers with 20 and 10 nodes in the first and second layer, respectively. This was determined through testing and analyzing the errors of the NN with respect to the synthetic test data set and the quality of the retrieval results after application to satellite measurements. More complex configurations of hidden layers and number of neurons were also tested and found to have worse performance when using OMI data as input. Hence the relatively simple configuration was chosen as the final setup for this study. The general concept and structure of the neural network used in the retrieval is illustrated in Figure 3.4.

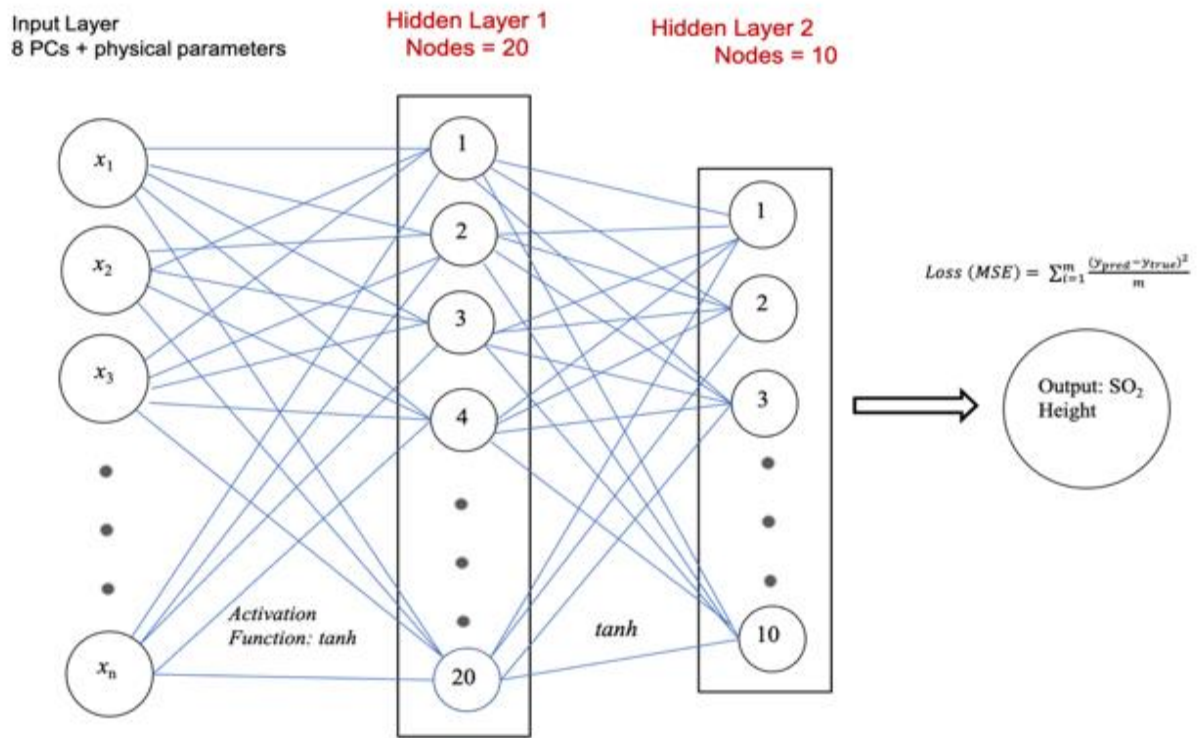


Figure 3.4: Diagram of a neural network with 2 hidden layers. The PCA-transformed data is provided into the input layer and the solution is obtained by minimizing error of SO₂ height.

In neural networks a common problem known as overfitting often occurs when the machine learning model is tuned so closely to the training inputs that it does not perform well on new data. During training this can be diagnosed if the validation error is much higher than the training error. To reduce overfitting, L2 regularization was implemented in the training. The regularization reduces the effect of small and very large weight values by penalizing the MSE loss function. For this study, the training was done separately for each OMI row due to the different VZAs and slit functions between rows; however, the configuration of the NN was kept constant between rows. The only difference in the training is the number of training epochs conducted for each row before the solution becomes optimal for that row. The number of epochs varies slightly but is in the 200-300 range for all rows. The final trained version of the NN, the inverse operator, contains the optimal weights needed to predict the SO₂ layer height from an input of separate test data.

An important aspect for neural network performance is the number of training samples. Aside from smart sampling, the appropriate number of samples for training can be determined by comparing errors from training runs where different percentages of training samples were removed (e.g., 10%, 20%, 50%) beforehand. The mean absolute error between height predicted by the NN and the test set height was calculated when using different numbers of input samples. With a 50% reduction in training samples, the absolute error went up by around 0.3 km. In contrast, reducing the training set by 10% had little impact on the error (see Table 3.3). These results provide confirmation that for this case the training data are adequate, and that there would likely be diminishing returns in NN performance with a larger training dataset.

Table 3.3: Mean absolute difference and RMSE for different reductions of the original training dataset. The test was performed on training sets for five different OMI rows and the errors were averaged.

% of samples withheld	0	10	20	30	40	50
Mean Abs Difference	0.95	0.98	1.02	1.08	1.12	1.24
RMSE	1.46	1.45	1.62	1.69	1.79	2.00

3.1.3 Application to satellite measurements

In the application phase of the retrieval, the inverse operator is applied to OMI radiance spectra, resulting in a predicted SO₂ layer height for each ground pixel in the OMI swath. For this the OMI L1B Geolocated Earthshine radiance dataset is used. Since OMI only provides absolute radiances, these data were normalized with respect to the same solar flux spectrum as used in the generation of the synthetic spectra. In other words, the measured input becomes the fraction of backscattered radiance to the incoming solar irradiance (i.e., reflectance spectrum). Prior to normalizing, the irradiance spectrum was convolved with an OMI slit function for the particular OMI row and orbit. The irradiance spectrum is convolved with the appropriate OMI slit function in order to have consistency in wavelength points between the measured radiances, synthetic radiances and irradiance of each row. To follow the same procedure as was used in the training step, the PCA operator from the training phase is applied to the OMI spectra to perform the dimensionality reduction and obtain a set of PC weights for each sample. The other inputs are VZA, SZA, RAA, albedo and surface pressure parameters from the OMI data files. As in the training phase, all inputs are scaled to the [-0.9, 0.9] range. After SO₂ heights are retrieved separately for each row, one height value is given for each pixel (and spectral sample). The application phase of the retrieval takes only 2-3 seconds for a given row. This short duration includes the application of the training phase PCA operator to OMI measurements, the scaling of

inputs and the deployment of the inverse operator. The whole process is repeated for each row in order to get a prediction for an entire OMI swath. For some rows the retrieval is unreliable due to the row anomaly, which negatively affects the quality of the OMI L1B radiance data at all wavelengths and consequently L2 retrievals.

3.1.4 Parameter Sensitivity Analysis

From the training phase, it becomes clear that the performance of the algorithm will depend on several factors. As demonstrated in Figure 3.5, two important factors are the SO₂ column amount and SZA which affects the retrieval error in some test samples.

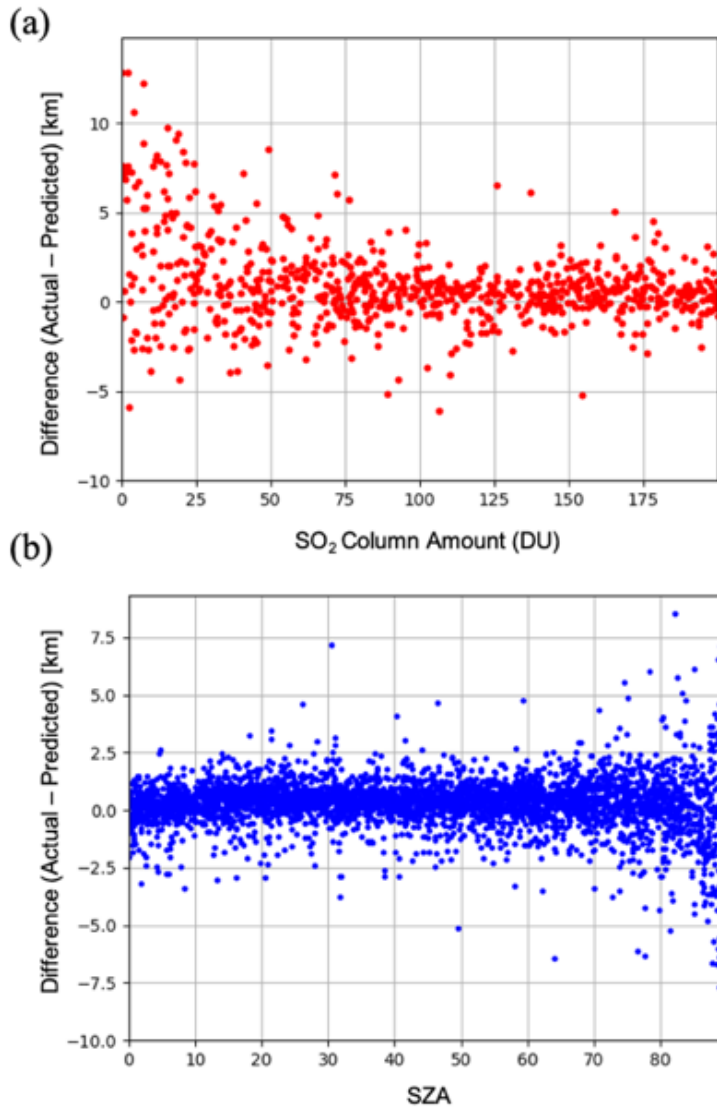


Figure 3.5: Dependence of retrieval errors on (a) SO₂ amount and (b) SZA for cases with SO₂ VCD > 40 DU. The error is defined as the difference between the SO₂ layer height predicted by the neural network using inputs from the independent test set, and the actual height from the same samples. The test set comprises 10% of the original spectral dataset withheld from training the neural network. The plots show that the retrieval error is mostly within +/- 2.5 km for SZA < 70 but increases significantly for large SZAs.

Overall, the NN makes better predictions for the test data subset for SO₂ amounts > 40 DU.

Below 40 DU, information content on the layer height to be retrieved becomes increasingly small, as evidenced by large differences between predicted heights and those in the actual test set (Figure 3.5a). Additionally, larger SO₂ loadings result in greater sensitivity between two heights,

as seen by comparisons of SO₂ height Jacobians for multiple amounts (Figure 3.6). For instance, the height Jacobian is reduced by 60-80% for the lower absorption wavelengths when the SO₂ amount in the RT calculation is 40 DU versus 200 DU. Quantitatively, if samples with SO₂ amounts less than 40 DU are excluded, the RMSE decreases from 1.48 to 1.15 km (Table 3.4). As with other sensitivity analyses, the RMSE and MAE in Table 3.3 are calculated between the predicted output from NN and the height from the independent test dataset.

Table 3.4: The RMSE and the mean absolute difference of all data points in the test set under different conditions. For each condition, the appropriate points were removed and excluded in error calculations. All cases in this table used synthetic training spectra with added SNR 1000.

	All cases	SO ₂ > 20 DU	SO ₂ > 40 DU	SO ₂ > 60 DU	SZA < 75°	SO ₂ > 40 DU and SZA < 75°	Albedo < 0.6	SO ₂ > 40 DU, SZA < 75°, Albedo < 0.6
RMSE	1.487	1.216	1.150	1.109	1.281	0.931	1.524	0.895
Absolute Mean Difference (km) (Predicted – Actual)	0.910	0.834	0.803	0.782	0.795	0.697	0.895	0.667

Therefore, I can expect the retrieval to produce reasonable results for moderate to large volcanic eruptions. In widely dispersed plumes where the SO₂ VCD is low or for volcanic degassing events, the retrieval would be less accurate. The second major dependency is on SZA. The problem here stems from the occurrence of relatively large errors in RT modeling due to shallow light paths and lower OMI SNR at the higher SZAs. Reasonably accurate results are to be expected only for SZA < 75°. Figure 3.5b shows significant differences in predicted and actual heights in spectra associated with large SZAs, after removal of low VCD samples.

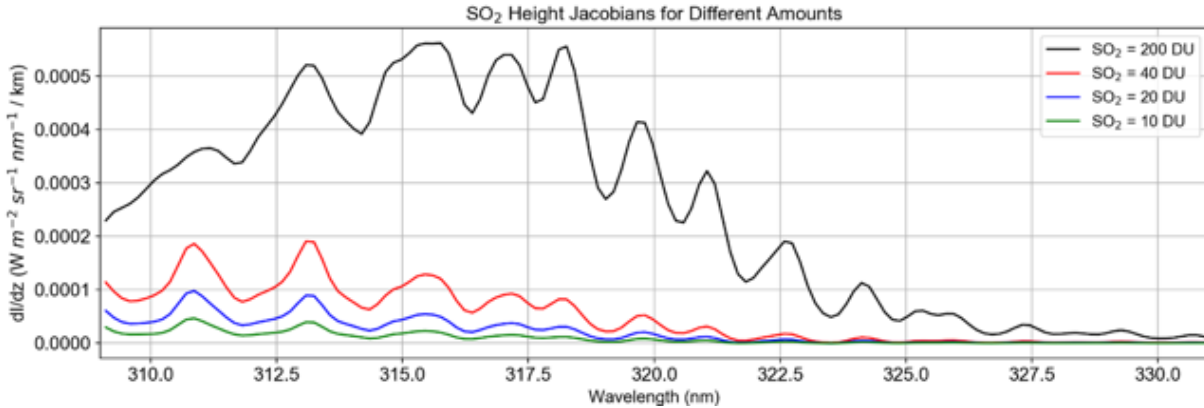


Figure 3.6: SO₂ Height Jacobians (dI/dz) for 4 different assumed SO₂ column amounts. The Jacobians were calculated from the difference between two radiance spectra with 10 km and 20 km SO₂ height. All other physical parameters were identical in the calculation of the spectra.

Due to these sensitivities, for the final training approach it was necessary to exclude spectra with large SZAs. Dependencies on other physical parameters are small when compared with these two issues discussed here, although there is some evidence that high surface albedo also increases error. If spectra with albedo > 0.6 are removed, there is a minor improvement in RMSE from 0.93 to ~ 0.89 km (Table 3.4). However, even with strong volcanic SO₂ signals, I can realistically expect that on average the absolute error to be at least 1 km, due to inherent simplifications in the neural network retrieval approach. The errors in actual retrievals using OMI data are expected to be larger due to introduction of measured spectra (see Section 3.3).

3.2 OMI SO₂ Layer Height Results

For testing the FP_ILM retrieval on OMI data, four volcanic eruption cases with sufficiently strong SO₂ signals were selected (i.e., where peak SO₂ VCDs were greater than 40 DU). Each case is described in detail in the following subsections. For each case, comparisons were made to other satellite-derived datasets where available, for example the Cloud-Aerosol Lidar with Orthogonal Polarization (CALIOP) lidar instrument onboard the Cloud-Aerosol Lidar

and Infrared Pathfinder Satellite Observation (CALIPSO), the IASI SO₂ layer height retrieval [Clarisse et al., 2014], and the GOME-2 [Efremenko et al., 2017] and TROPOMI retrievals [Hedelt et al., 2019]. It is important to note that the CALIOP lidar indicates the height of the ash plume rather than the SO₂ height. Although ash and SO₂ plumes are often collocated, this is not always the case, thus making direct comparisons difficult. In addition, CALIPSO measures one cross section of the plume and does not have the spatial coverage of the entire plume like OMI.

3.2.1 Kasatochi (2008)

Kasatochi is a volcano located on the Aleutian Islands of Alaska (52.178°N, 175.508°W). It underwent a series of eruptions beginning late in the day on August 7th, 2008, which injected great amounts of ash and SO₂ into the stratosphere. Overall, the explosion released roughly 2 million tons of SO₂, at the time the highest SO₂ loading since the Mt Pinatubo eruption [Yang et al., 2010]. SO₂ effective layer heights retrieved using the machine learning model for OMI (orbit 21650) on August 10th, 2008, were around 11-12 km with some portions being slightly lower (Figure 3.7a). This is in reasonable agreement with previous SO₂ height retrievals of 9-11 km which used the ISF algorithm for OMI [Yang et al., 2010], considering that the uncertainty of both retrievals are around 2 km. Likewise, Nowlan et al. [2011] showed that the majority of the plume was around 10 km, and up to 15 km in some parts. There is also agreement with IASI (Figure 3.7b) and CALIOP data (Figure 3.7d) which showed plume heights of 10-12 km and 12.5 km respectively. The lidar data is considered the most accurate source, however it only offers one cross section of the plume in its overpass rather than full spatial coverage. It is important to note that the IASI overpass occurred later in the day than those for OMI and CALIPSO. Another verification source I used was the GOME-2 SO₂ layer height retrieval that uses FP_ILM [Efremenko et al., 2017]. The study found a height of around 10 km and up to 14

km in areas of high SO₂ loading for August 10th (Figure 3.7c). The GOME-2 overpass occurred 4 hours earlier than OMI. The mean, median, standard deviation, and the inner quartile range (IQR) of the three retrievals (Table 3.5) also show good agreement for this case. Although the OMI results agree well in general with the results of these studies and datasets, the retrieval is less sensitive with respect to detecting variability in the SO₂ layer height within the plume.

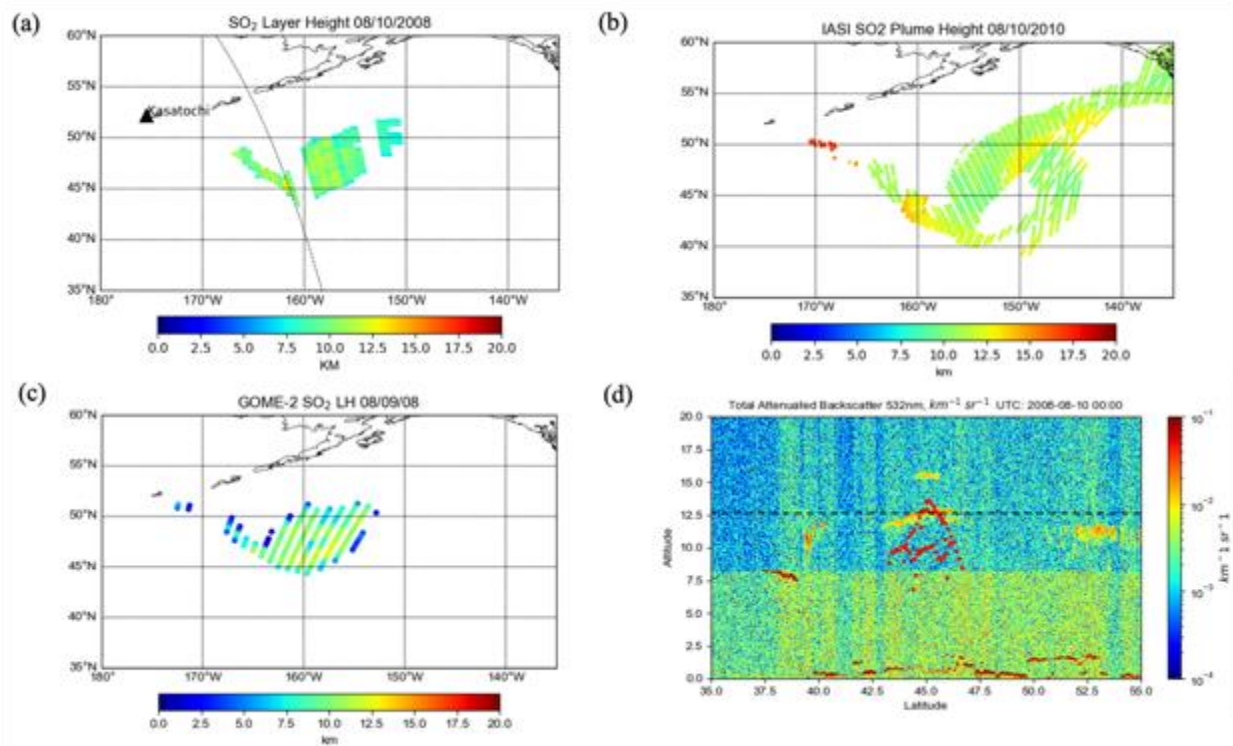


Figure 3.7: Comparison between the volcanic plume heights from (a) OMI, (b) IASI, (c) GOME-2 and (d) CALIOP lidar 532-nm attenuated backscatter, for the 2008 Kasatochi eruption. The black dotted line in (a) shows the CALIPSO track. Some rows of OMI in this case were affected by the row anomaly, as seen by the gaps in the plume. The red dots in (d) show the OMI retrieval near the CALIPSO path and the black dashed line denotes the height of the ash plume observed by CALIPSO.

Table 3.5: Statistical comparisons of the SO₂ height retrievals for two days of the Raikoke eruption and the Kasatochi eruption cases.

Metric (km)	Raikoke (June 23 rd , 2019)			Raikoke (June 24 th , 2019)			Kasatochi (Aug 10 th , 2008)		
	OMI	IASI	TROPOMI	OMI	IASI	TROPOMI	OMI	IASI	GOME-2
Std. Deviation	1.67	0.85	1.96	2.38	0.65	1.04	1.39	0.72	1.29
Median	10.60	9.00	12.10	10.30	10.00	13.24	9.70	10.00	10.21
Mean	10.20	9.63	12.15	10.00	9.83	13.30	9.84	10.40	10.02
IQR	1.79	1.00	2.71	2.68	1.00	1.20	1.36	1.00	1.67

3.2.2 Kelud (2014)

Kelud, a stratovolcano located in East Java, Indonesia (7.935°S, 112.315°E), erupted on February 13th, 2014 at 1550 UTC, in the process depositing ash in a 500 km diameter around the volcano and leading to mass evacuations from nearby towns. Even though this case has somewhat lower SO₂ VCDs than those from Raikoke and Kasatochi, the peak SO₂ VCDs of ~60-70 DU should still allow for retrievals with reasonable accuracy. The OMI retrieval results indicate that the maximum height of the main plume was 18-19 km (Figure 3.8b), although other studies suggest that several smaller layers of SO₂ and ash were located as high as 26 km [Vernier et al., 2016] on the previous day. However, the SO₂ loading at that level was most likely too low for an accurate retrieval using OMI radiances. CALIOP lidar detected ash plumes at around 19.5 km and the IASI retrievals registered the plume at 17.5 km over the same area as that for OMI. The height of the ash plume from this eruption was also estimated using Multifunctional Transport Satellite (MTSAT 2) observations and transport modeling [Kristiansen et al., 2015]. That study found an injected height of around 17 km, which is in agreement with the OMI result, especially when considering the most probable heights on the PDF (Figure 3.9b). I note here that only a small portion of the plume was retrieved with our algorithm, given the relatively low SO₂ VCDs and interference due to the OMI row anomaly. It is promising to note that the OMI

retrieval was able to identify heights at the upper end of the height range used in the training phase. On the other hand, while the retrieval can extrapolate to heights above 20 km, the accuracy would likely degrade due to the lack of training data with heights outside of this limit.

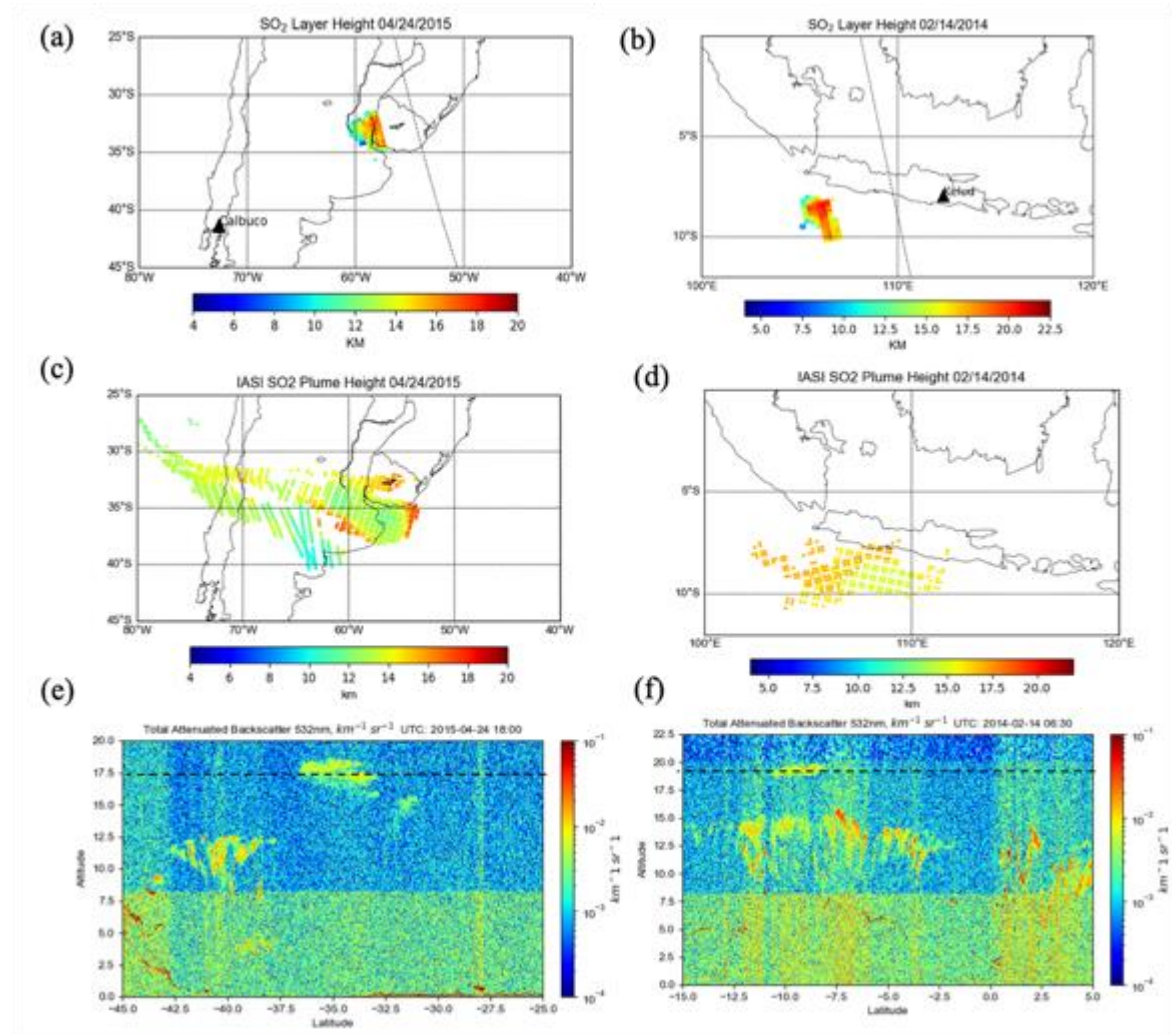


Figure 3.8: Comparisons of plume heights for the 2015 Calbuco eruption (left) and the Kelud eruption (right) for OMI (a,b), IASI (c,d) and 532-nm total attenuated backscatter from the CALIOP lidar (e,f). For OMI, only pixels with > 30 DU of SO₂ are shown and retrievals were unavailable for some parts of the plume due to the row anomaly. The black dotted line in (a) and (b) marks the CALIPSO track. Direct comparison with CALIPSO was not possible due to obstruction by the OMI row anomaly

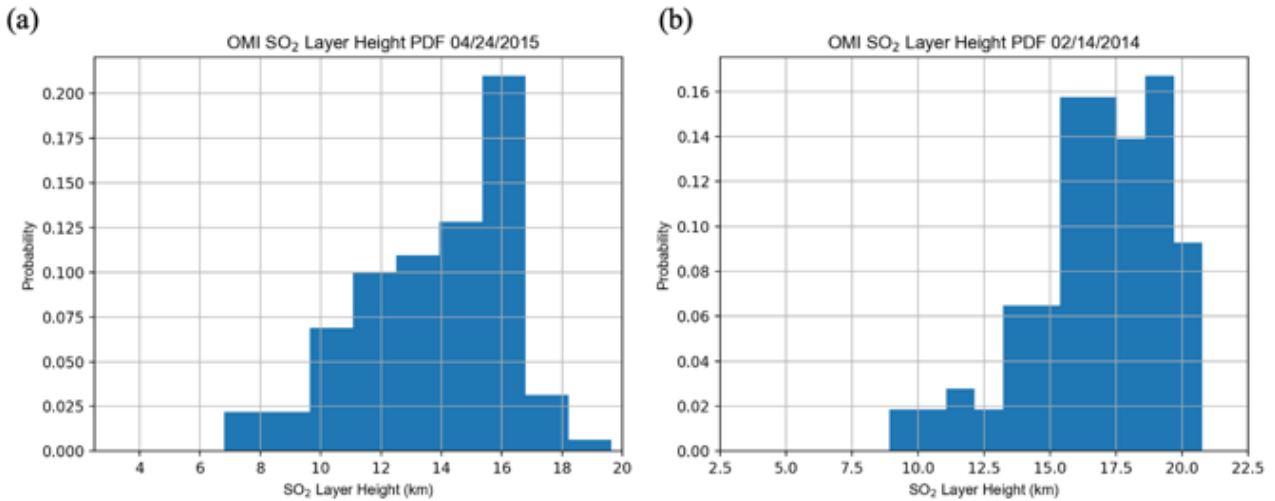


Figure 3.9: Probability histograms of SO₂ effective layer height retrievals for (a) the Calbuco eruption on April 24, 2015 and (b) the Kelud eruption on February 14, 2014.

3.2.3 Calbuco (2015)

The Calbuco volcano is located in Chile (41.331°S, 72.609°W). The primary eruption had a volcanic explosivity index (VEI) of 4 and occurred on April 22nd with little warning. The primary plume ascended higher than 15 km, while plumes from smaller subsequent eruptions stayed in the troposphere. The volcanic plume spread northeast in the following days, resulting in flight cancellations at Uruguayan and south Brazilian airports. The OMI-retrieved SO₂ effective layer heights in the area of greatest VCD was in the 15-17 km range (Figure 3.8a). In the same region, IASI results (Figure 3.8c) show similar plume heights, approximately around 15 km, although as with the previous events, the overpass times of the two instruments are different. CALIOP lidar shows the ash plume to at roughly 17 km (Figure 3.8e). Unfortunately, the overpass of CALIPSO occurs over an area of OMI's swath that is affected by the row anomaly, and this makes a direct comparison unfeasible. Nevertheless, the CALIPSO aerosol layer height is still comparable to OMI-retrieved effective SO₂ layer heights for the portion of the plume further to the west. The retrieval for OMI is consistent with the other instruments for SO₂

plumes, with the exception of the part of the plume with low SO₂ amounts (< 30 DU) for which results were not plotted in Figure 3.8a due to lower biases.

3.2.4 Raikoke (2019)

The eruption of the Raikoke stratovolcano (48.2932°N, 153.254°E), located on the Kuril Islands of Russia, occurred on June 21st, 2019 at 1800 UTC. A series of explosions during the eruption sent large amounts of ash and SO₂ into the lower stratosphere. Maximal loadings of SO₂ measured by OMI and other sensors exceeded 500 DU. In the following days the plume underwent dispersion and spread out over the northern Pacific Ocean and later over eastern Russia. Early estimates of plume injection height for the eruption were predominantly in the 10-13 km range with potentially larger heights in some areas of the plume. In Figures 3.10a and 3.10b, the SO₂ effective layer heights retrieved from OMI data are shown for the Raikoke plume on June 23rd and June 24th respectively. The plume heights for both days are predominantly in the range 10-12 km, although some areas of the plume had estimated peak heights of 13-14 km. In comparison, the TROPOMI results show slightly larger heights (13-14 km) for June 24th and similar heights to OMI for June 23rd (Figure 3.10c and d). The difference may partially be due to the finer resolution of TROPOMI and catching more of the peak heights than OMI. The IASI SO₂ height product also shows fairly good agreement, with heights mainly at the 10-11 km level (Figure 3.10e and f). It is also useful to look at a distribution of heights predicted for the domain (Figure 3.11) in order to get a more quantitative comparison between the datasets. Based on this distribution, there is clearly at least 2 km difference between the most probable heights from OMI and those from TROPOMI for June 24th (Figure 3.11b and d) and slightly lower heights in the distribution for IASI. This is also displayed in Table 3.5 which shows a 2-3 km difference in the mean and median of retrieved heights between OMI and TROPOMI.

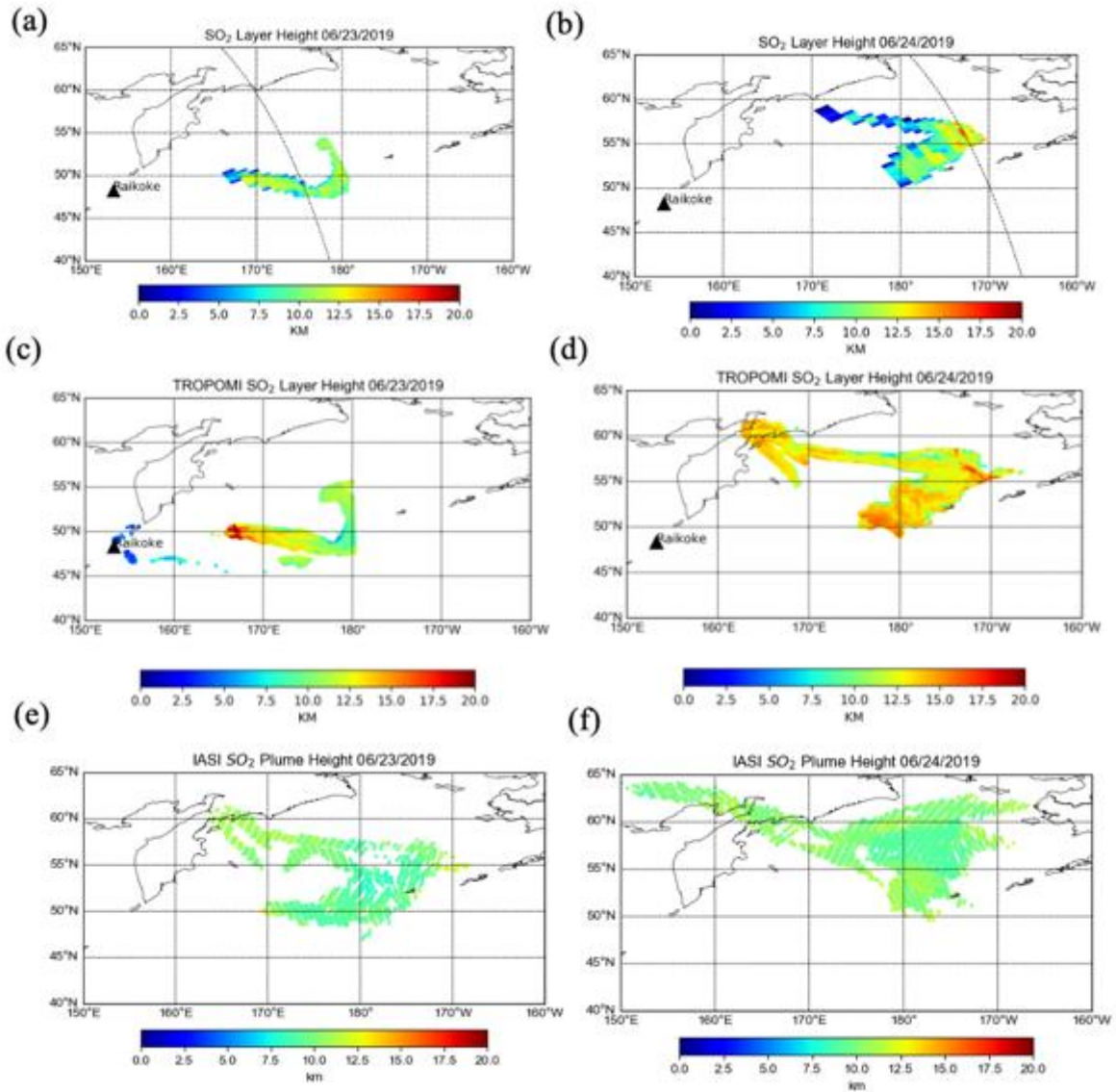


Figure 3.10: The SO₂ layer height retrieval for the Raikoke eruption plume on June 23rd, 2019 (left) and June 24th, 2019 (right) for the OMI (a, b), TROPOMI (c, d) and IASI (e, f) instruments. For all 3 sensors, only pixels where SO₂ VCD > 30 DU are shown.

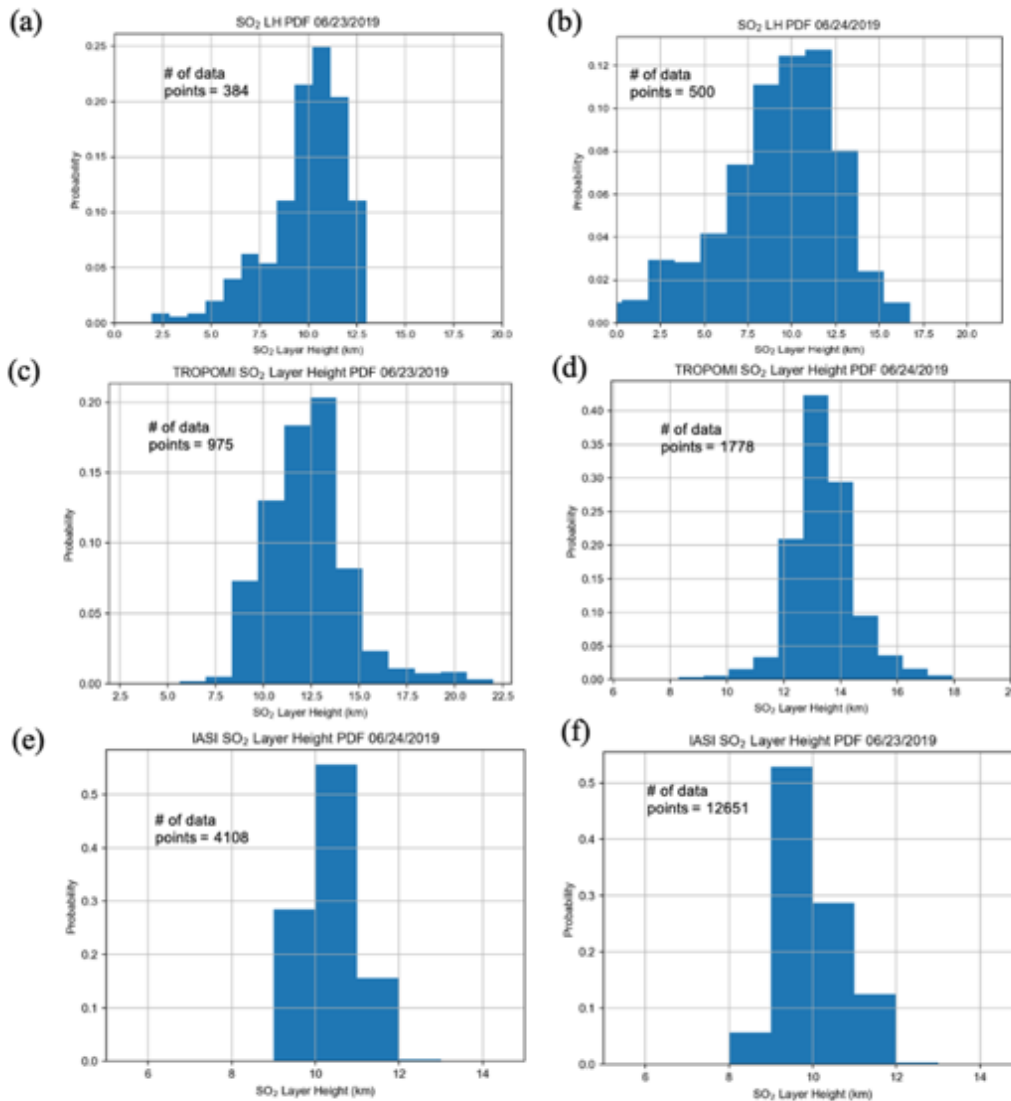


Figure 3.11: Probability histograms of SO₂ layer height retrievals for (a,b) OMI and (c,d), TROPOMI on June 23rd, 2019 (left) and June 24th, 2019 (right) and (e,f) IASI. Only pixels with SO₂ column amount greater than 30 DU are included. These plots correspond to the results plotted in Figures 3.10a-f.

Additionally the IQR and standard deviation provide a quantitative measure of the variation in the distribution of the retrieved heights, which can change from one orbit to another. Note that points with lower than 30 DU are not included in the PDFs for all sensors. The results are also compared with CALIOP lidar onboard CALIPSO, which shows ash plume heights of 12-13 km for both days (Figure 3.12a and b). Although there is overestimation for some OMI pixels,

especially for June 24th, the section of the plume with the CALIPSO flyover has similar heights (around 12.5 km) to lidar-determined aerosol layer altitudes. Lastly, I note that a recent study highlighted probabilistic height retrievals using the Crosstrack Infrared Sounder (CrIS) for Raikoke. This study found a median height of 10-12 km across a large part of the plume, however with some areas upwards of 15 km. While there are some notable differences across all of the datasets, the OMI retrieval for this case falls within the general consensus of plume height estimates for this volcanic event.

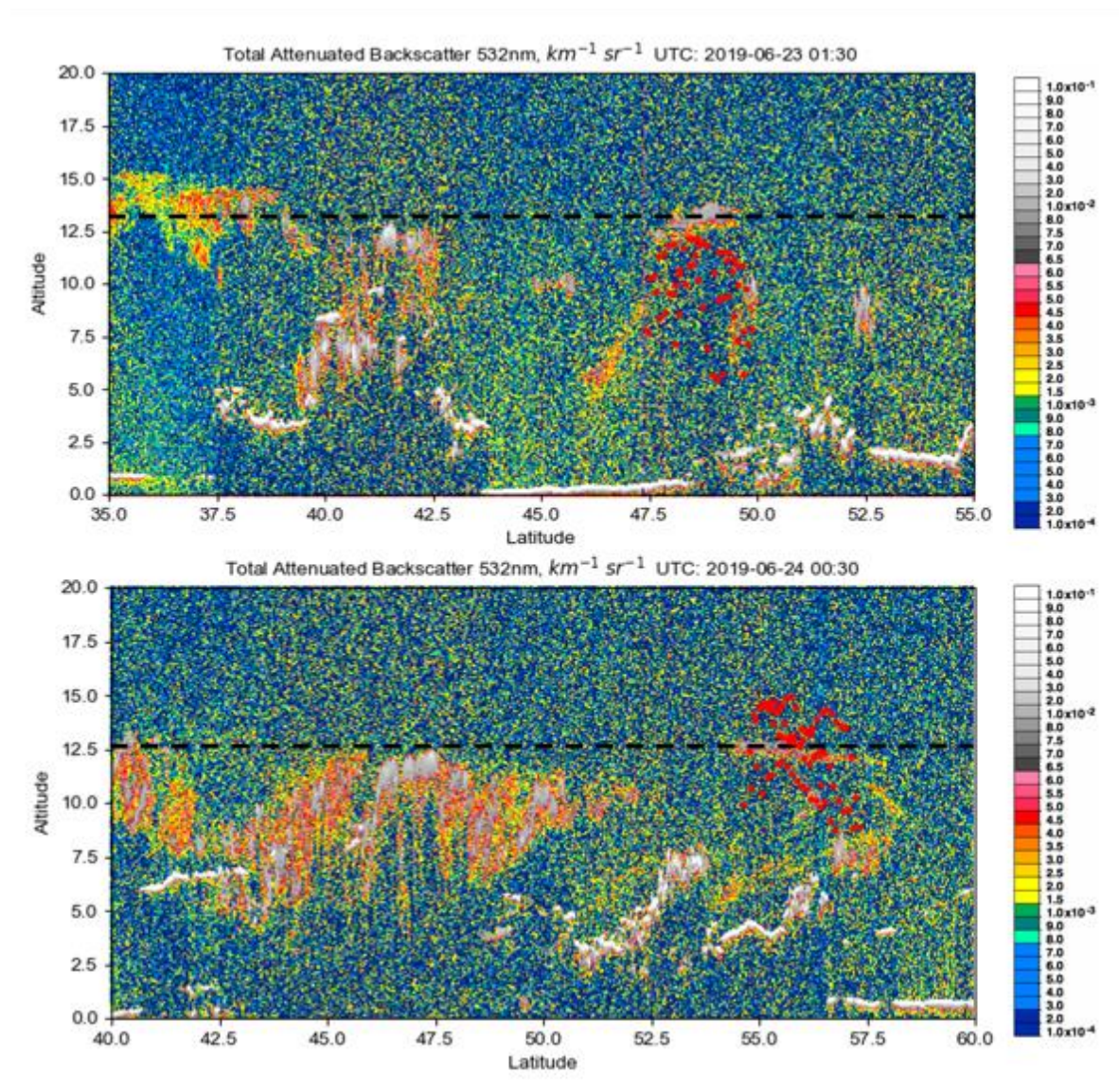


Figure 3.12: CALIPSO lidar 532-nm attenuated backscatter for the Raikoke eruption on (a) June 23rd and (b) June 24th, 2019. The black dashed line symbolizes the height of ash plume seen by CALIPSO and red dots show the results from the OMI retrieval along CALIPSO's flight path. The flyovers occurred shortly after 01:30 and 00:30 UTC on June 23rd and 24th respectively, around the same time as OMI.

3.3 Discussion

It is clear that predicting SO₂ layer height with FP_ILM is an efficient process, but one that is not flawless in terms of accuracy. As comparisons between instruments/retrievals have shown, on average there were 1-2 km differences in heights, especially for the Raikoke event, although I consider this to be good agreement given the estimated MAE and RMSE associated with this retrieval. In this regard, the retrieval is an approximate estimate of the SO₂ plume height rather than a precise determination. Differences in the retrieved heights between different studies/algorithms result from differences in instruments, forward model assumptions and retrieval techniques as well as uncertainties in each retrieval. For instance, IASI is a thermal IR instrument and its retrieval does not use FP_ILM. Therefore exact agreement with IASI results is difficult to achieve, especially since the IASI retrieval itself has a stated error range of ± 2 km, although its retrievals serve as a good verification dataset. The stated uncertainty for TROPOMI retrievals [Hedelt et al., 2019] is ~ 2 km for SO₂ amounts of greater than 20 DU, similar to our estimated uncertainties for OMI. While the general retrieval approach for TROPOMI [Hedelt et al., 2019] is similar to that for OMI in the present study, there are also important instrument differences that can lead to differences in the retrieved heights between the two instruments, such as the pixel size, noise, radiometric accuracy and the level of degradation. TROPOMI has a much finer spatial resolution compared to OMI, with footprints typically 5.5×3.5 km² up to maximum size 7×3.5 km²; TROPOMI also has larger maximal SO₂ signals. Consequently, TROPOMI is better able to resolve localized variations in the height throughout the plume and is

likely to be more accurate overall due to better SNR. However, current TROPOMI L1 data are known to have issues with instrument degradation and radiometric accuracy in the UV spectral range [Ludewig et al., 2020]; this could be a potential contributing factor the differences between the two instruments. OMI retrievals show more or less uniform height levels across the entire plume with the peak heights in areas with the best SO₂ signal. Note, CALIOP lidar profiles sometimes show disagreements with OMI retrieved heights, because CALIOP only identifies the height of the ash or aerosol plume. It also offers a comparison for only a single cross section of the entire plume per orbit. Despite the uncertainties, the consensus provided by different instrumental datasets can provide a reasonable estimate for the SO₂ layer height, and if done in near real time, can aid in decision making with regards to aviation safety.

Another source of error is present in the training phase. One difficulty here is finding the ideal choice of neural network setup. With many parameters to consider, such as the number of input PCs, number of layers, number of nodes, learning rate, regularization, weight initialization, etc., it is very time consuming to optimize the neural network setup. The relatively simple configuration that I found performed reasonably well with both test data and real OMI measurements for all scenarios and events considered. However, even after optimization of the parameters, random error inherently exists in the neural network. A measure of random error can be obtained by altering the random state of the neural network whilst keeping other parameters constant. For ten trial runs with different random seeds, variations of the MAE error were around 0.15-0.2 km (Table 3.6).

Table 3.6: Effect of altering random seed number on error obtained using the test dataset, and the SO₂ height retrieval result after application to OMI. For the results, heights for two different pixels within the orbit from the Raikoke event (June 24th, 2019) are shown. Heights were retrieved using separate inverse models trained using 10 random states.

		Random Seed Number	1	2	3	4	5	6	7	8	9	10
NN Training error	Abs. Mean Error		0.98	1.14	1.03	1.16	1.08	1.18	1.05	1.01	1.12	0.98
	RMSE		1.69	1.85	1.71	1.78	1.79	1.92	1.71	1.67	1.73	1.70
Application (Raikoke - OMI Orbit 79463)	Sample pixel 1		10.52	10.69	10.49	9.72	9.98	10.23	10.53	10.19	10.07	10.48
	Sample pixel 2		12.42	13.15	12.08	11.70	11.88	12.01	12.38	11.22	11.94	12.16

Although the differences in the errors calculated with the synthetic test data are relatively small, larger changes can be expected during the application phase. Indeed, when applying the inverse models to OMI, there is noticeable, up to 1 km variation in the retrieved height for the same pixels. It is thus difficult to improve results further than ~1 km absolute error, even in the training phase. In the application phase, some additional error comes from the differences between synthetic spectra and real satellite measurements with noise errors. For example, with an SNR of 500 used in training, which is a typical noise level for OMI, the RMSE of the neural network prediction is around 1.25 km (see Table 3.2).

This can be considered the lower limit of retrieval error when the inverse operator is used on OMI measurements. Lastly, some deviations between the measured and synthetic training spectra originate from the RT modeling. The calculations contain several assumptions including the SO₂ plume shape, atmospheric profiles, gas profiles, and a molecular scattering atmosphere. Further testing is required in order to determine if the inclusion of aerosols in RT calculations would improve the algorithm performance.

3.4 Conclusion

In this study I introduced a new algorithm for OMI retrievals of the volcanic SO₂ effective layer height from UV earthshine radiances. This algorithm is based on an existing FP_ILM method which combines a computationally time-consuming training phase with full radiative transfer model simulations and a machine learning approach to develop a fast inverse model for the extraction of plume height information from radiance spectra. Fast performance means that the algorithm can be considered for operational deployment, given that the retrieval of a SO₂ layer height prediction from the inverse model takes only a matter of milliseconds for a single OMI ground pixel. For the training, a synthetic dataset of earthshine radiance spectra were created with the LIDORT-RRS RT model for a variety of conditions based on choices of 8 physical parameters determined with smart sampling techniques. A dimensionality reduction was performed through PCA in order to reduce the complexity of the problem and to separate those features that best capture the great majority of variance of the dataset; 8 principal components were sufficient for this purpose. Dimensionally-reduced data together with the associated parameters were used to train a double hidden-layer neural network to predict SO₂ plume height from any given input data. The PCA from the training phase and the inverse operator resulting from the optimal NN framework were then applied to real satellite radiance spectra and parameters to get retrieved values of SO₂ plume heights for several volcanic eruption events.

Through comparisons with CALIPSO lidar overpasses, as well as TROPOMI and IASI retrievals, it was shown that the retrieval for OMI can estimate reasonable SO₂ layer height for all the events considered, with absolute errors in the range of 1-2 km. These results can give an indication of plume heights achieved during medium- to large-scale eruptions, and guide important decisions in aviation hazard mitigation. For all events treated in this study, there was

general agreement with CALIOP lidar, although SO₂ could not be retrieved for the locations of the CALIPSO flight path for the Kelud and Calbuco cases due to OMI row anomaly issues.

Chapter 4: Application of SO₂ Layer Height Retrieval

4.1 Application of the algorithm to other instruments

In Chapter 3, the new OMI SO₂ layer height retrieval with the FP-ILM algorithm was discussed. One of the advantages of this algorithm is that it is not restricted specifically to OMI. It has already been used for TROPOMI and GOME-2 retrievals and can be applied to other UV instruments as well. The process of implementing the algorithm with other instruments is similar to that for OMI, and involves multiple steps including PCA of the data and training of the neural network. The main difference in the retrieval process between different instruments is that during the training phase, the synthetic spectra are convolved with the instrument slit functions (or spectral response functions) that are unique to the specific sensor. The SNR in the added noise can also depend on the instrument. The training process of the neural network was therefore adjusted to account for the instrument-specific slit function and SNR. I applied the FP-ILM algorithm to two additional instruments – the Ozone Mapping and Profiler Suite (OMPS) onboard the Suomi National Polar-orbiting Partnership (SNPP) satellite, and the newer copy of the instrument on board the NOAA-20 satellite (NOAA-20 OMPS).

4.1.1 Background on SNPP/OMPS and NOAA20/OMPS

The Suomi-NPP OMPS instrument has been in operation since 2011 [Flynn et al., 2014] and like OMI has been used for retrievals of ozone, SO₂, and other gases. It measures backscattered UV radiances in the 300-380 nm range. OMPS contains a nadir mapper with a 2800 km cross track, 36 cross track positions, a 50 km × 50 km spatial resolution at nadir, and a spectral resolution of ~1 nm. These resolutions are both coarser than OMI, which has 13×24 km resolution at nadir and ~0.5 nm spectral resolution. Although the relatively coarse resolution can lead to dilution in SO₂ signals from anthropogenic and small degassing volcanoes as compared

with OMI, OMPS has a higher SNR of around 1500 at 310 nm [Yang et al., 2013]. Another advantage of OMPS is that it does not suffer the same instrument issues as OMI, namely the row anomaly (see section 1.2), which reduces the quality and spatial coverage of the instrument radiance data. Therefore, OMPS together with OMI can provide better overall coverage, as well as being a useful source for intercomparisons for SO₂ amount and SO₂ height retrievals. As a newer instrument, OMPS can also continue the existing OMI data records of ozone and SO₂. The OMPS SO₂ VCD retrievals are currently produced with the same PCA algorithm that is used for the OMI SO₂ product. These retrievals have been found to be consistent with OMI for moderate to large volcanic eruptions (Li et al., 2017). Although OMPS has lower sensitivity for anthropogenic point sources than volcanic, another study found that the correlation between the two instruments is still around $r = 0.9$ for anthropogenic SO₂ sources on average globally [Zhang et al., 2017]. The same study also notes that OMPS can detect 50% of 10-50 kt yr⁻¹ emission sources and 100% of sources greater than 130 kt yr⁻¹ that are detected by OMI. As with the OMI product, the OMPS SO₂ product also has different retrieved VCDs using the same assumed reference plume center heights – 3 km (lower troposphere), 8 km (mid troposphere), 13 km (upper troposphere) and 18 km (lower stratosphere).

Operations for the NOAA-20 OMPS instrument began in late 2017, as part of the Joint Polar Satellite System (JPSS-1). It flies ~50 min ahead of SNPP OMPS in the same Sun-synchronous orbit. It is similar to SNPP/OMPS but operates at significantly finer spatial resolution. The nadir mapper of NOAA-20/OMPS has a 17 km×17 km spatial resolution from a nadir viewing position due to less co-adding of pixels. This gives the NOAA-20 more utility at observing volcanic plumes in better detail compared to the lower resolution instruments. However, it is important to note the NOAA-20 OMPS has not been as thoroughly calibrated as

the SNPP/OMPS, which may lead to biases in the SO₂ height retrievals. It also has a lower SNR due to the higher resolution.

4.1.2 FP-ILM Results

The 2019 Raikoke eruption was chosen as the test case for the retrievals of the OMPS instruments, as it is a large eruption with a strong SO₂ signal that was captured by both OMPS instruments. The SO₂ layer height retrievals were tested for two orbits on June 24th, 2019 (Figure 4.1). Results can also be compared to OMI results in Chapter 3 since the overpass times are generally within one hour for each day.

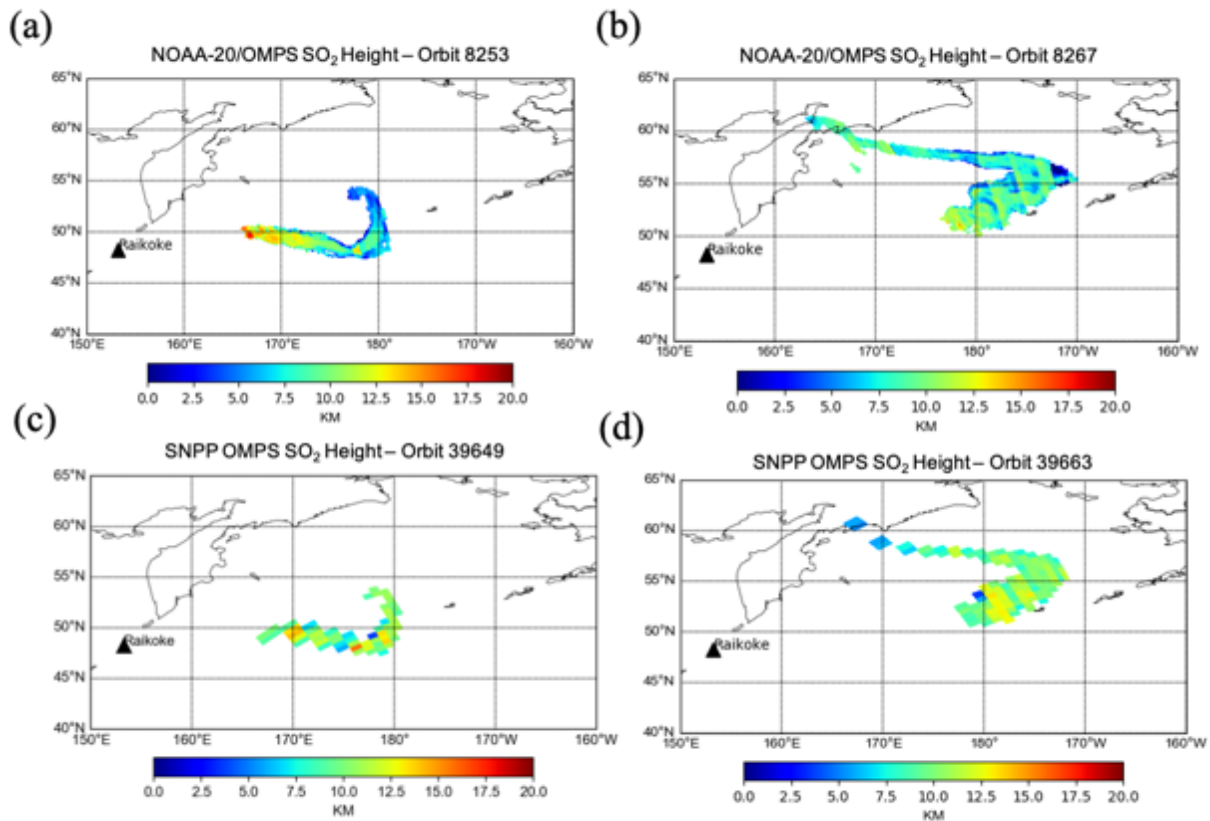


Figure 4.1: Mapped SO₂ layer height retrievals for (a) orbit 8253 and (b) orbit 8267 of NOAA-20 OMPS, and (c) orbit 39649 and (d) orbit 39663 of SNPP/OMPS. Pixels with SO₂ VCD < 20 DU are excluded. The Data corresponds to overpasses on 06/23/2019 and 06/24/2019 around 00Z, the second and third day after the start of the eruption. The overpass of NOAA-20 occurs 50 minutes ahead of SNPP/OMPS.

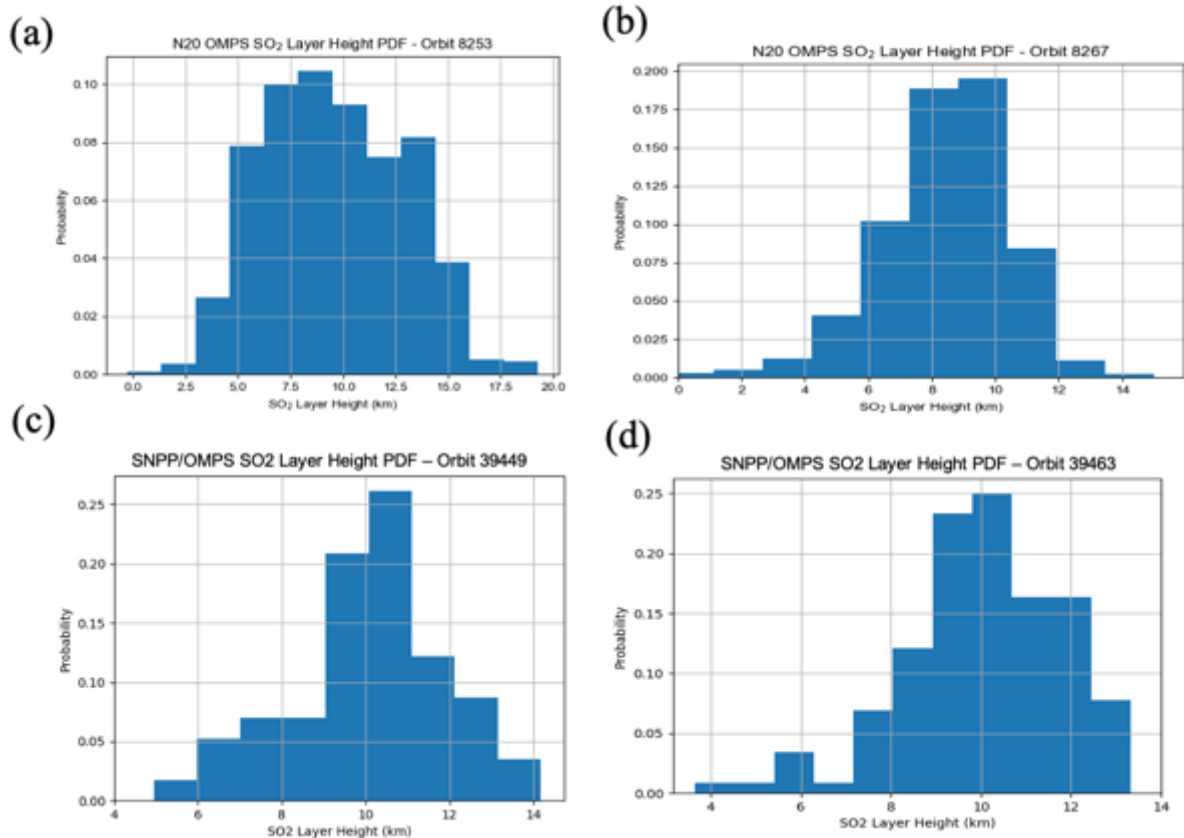


Figure 4.2: Probability density histograms of SO₂ layer height retrievals for (a,b) NOAA-20 OMPS and (c,d), SNPP/OMPS on June 23rd, 2019 (left) and June 24th, 2019 (right). Only pixels with SO₂ VCD greater than 20 DU are included in the calculation. These plots correspond to the results plotted in Figures 4.1a-d.

Overall the results for SNPP/OMPS and NOAA-20 OMPS are consistent with OMI within the 2 km uncertainty range. The differences in mean and median between instruments are less than 1 km which is consistent with the peaks of the height distributions (Figure 4.2). The probability density functions of the results (Figure 4.2) shows that the NOAA-20/OMPS retrieved SO₂ heights are centered at around ~9 km which is slightly lower than SNPP/OMPS, which had a mode at 10-10.5 km. The standard deviation and inner quartile range for the OMPS instruments are higher (by around 0.5 km and 1-1.5 km respectively) than OMI the retrieval, which indicates slightly larger spread the retrieved SO₂ layer heights across the plume domains. It is possible the

retrieval algorithm may be further refined for the two OMPS instruments; however, for a preliminary test the results show fairly good agreement.

Table 4.1: Statistics of OMI, SNPP/OMPS and N20-OMPS height retrievals for the Raikoke eruption case.

Metric (km)	Raikoke Day 1 (06/24/19 00Z)			Raikoke Day 2 (06/24/19 23Z)		
	OMI	SNPP/OMPS	N20-OMPS	OMI	SNPP/OMPS	N20-OMPS
Standard Deviation	2.38	2.73	2.93	1.67	1.97	2.17
Median	10.30	10.27	9.46	10.60	9.75	9.44
Mean	10.00	10.11	9.52	10.20	10.00	9.21
IQR	2.68	2.87	3.38	1.79	3.10	2.55

The promising results show that the FP-ILM algorithm can be applied to more 1 hyperspectral UV instruments and thus build a long-term data record of volcanic SO₂ layer heights from multiple satellites. Given the excellent signal to noise ratio of OMPS and improved spatial resolution in the case of NOAA-20 OMPS, these instruments would be ideal for operational NRT retrievals of volcanic SO₂ layer height.

4.2 Volcanic Plume Tracking

The second application of the SO₂ plume height retrieval is to aid in plume forecasting. While satellite observation of the SO₂ height via the retrievals provides useful information about the current state of the volcanic plume, another crucial component is forecasting where the plume will go in the near future. This can give advanced warning for addressing aviation safety concerns. In general, the transport of a constituent such as ash or SO₂ is simulated through a chemical transport model or a trajectory model combined with initial meteorological conditions, that can track where an air parcel will go hours or days into the future. For instance, the model

used by NASA for volcanic applications is the GEOS-5 earth system model coupled with the Goddard Chemistry Aerosol and Radiation (GOCART) module [Chin et al., 2000; Colarco et al., 2010]. It performs simulation with an input of SO₂ and ash flux from the eruption and an assumed injection height. Due to their speed and simplicity, trajectory models can have an advantage in producing quick and relatively accurate forecasts. In this section, the ability of using the retrieved SO₂ height within the HYSPLIT trajectory model is demonstrated for forecasting the movement of the plume. While a full chemical transport model would incorporate more details such as fluxes and chemical processes, HYSPLIT is a suitable tool for solely determining the future location and height of an SO₂ plume. One of the most important parameters is the SO₂ height, which can strongly affect the forecast produced by both chemical transport and trajectory models. In many cases the height is estimated rather than observed which can lead to some inaccuracies; thus it is important to have SO₂ height retrieval algorithms. In this section I will use my retrieved height as input into the HYSPLIT to assess plume forecasts.

4.2.1 HYSPLIT Trajectory Modeling

To demonstrate how the retrieved SO₂ height can be applied, I use forward trajectories calculated by HYSPLIT from a grid of starting points (Figure 4.3). The points are composed of re-gridded height retrievals in the vicinity of the volcanic plumes of interest.

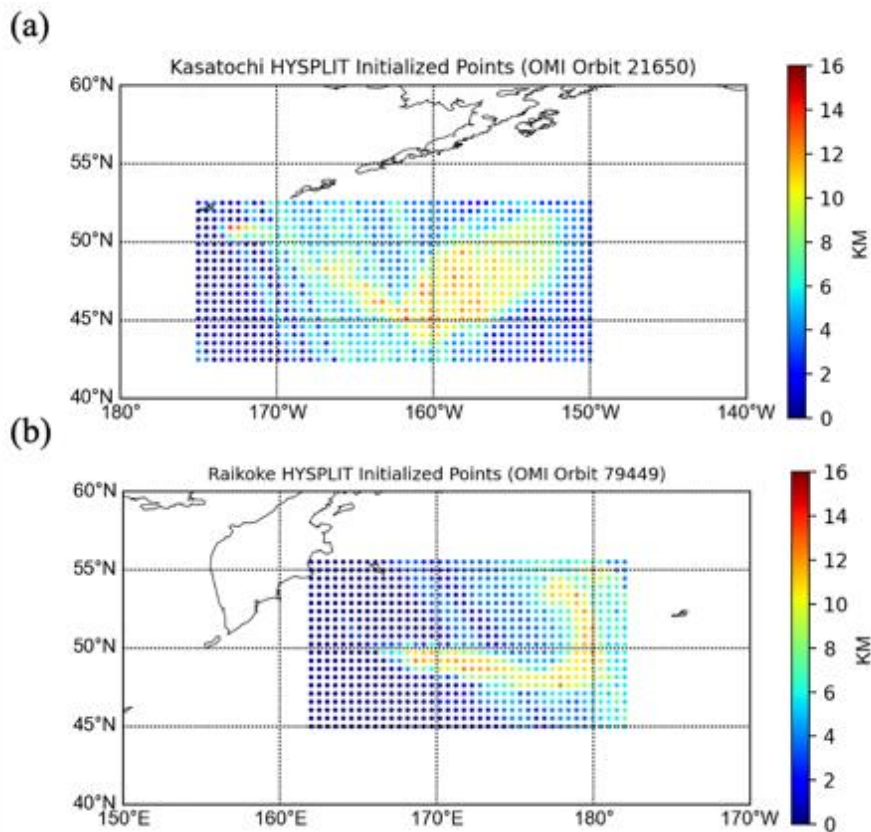


Figure 4.3: Starting grid setup with the SO₂ layer heights from OMI FP-ILM retrieval for (a) Kasatochi case and (b) Raikoke case. The heights used are from OMI orbit 21650 and 79449 respectively. Each point with the associated altitude represents a single starting point for a HYSPLIT trajectory calculation.

As described in Chapter 2, the trajectory calculation is initialized with the starting coordinates and altitude of the air parcel, along with the meteorological data such as temperature, pressure, and wind data for the starting day and time. The meteorological dataset used for this application was the NCEP Global Data Assimilation System (GDAS) that has a horizontal resolution of 1° latitude by 1° longitude and contains 23 vertical layers. Forward trajectories were calculated for 3 days into the future from the initial observation. I note that the OMI overpass does not occur exactly the same time each day but rather around an hour earlier than the previous day. Therefore the trajectory data analyzed here were for 23, 46, and 69 hours from the start time. The OMI SO₂

Layer height was re-gridded to a 0.5° by 0.5° grid that covers the domain of the volcanic plume. It was then used as an input into HYSPLIT as the starting altitude. Since the plume height can be somewhat uncertain, a vertical SO_2 profile was assumed with a near Gaussian distribution within ± 2 km of the retrieved height (Figure 4.4). The 3D grid initialized into the model contained thousands of points, the exact number depending on the size of the domain covered by the plume.

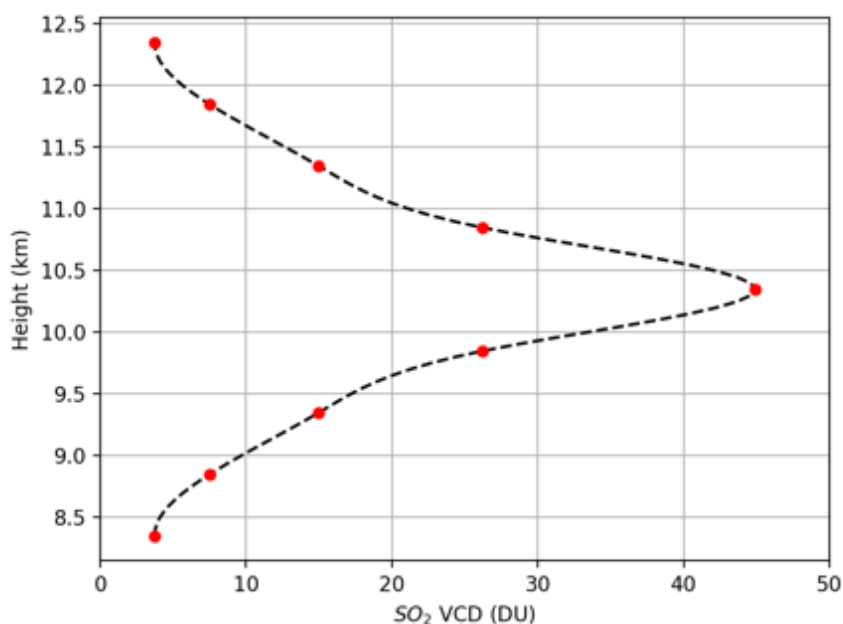


Figure 4.4: Example of the distribution of SO_2 height for a single grid point in the HYSPLIT initialization. The red dots indicate all the points where the trajectory is initialized. The distribution is centered around the retrieved height from FP-ILM interpolated at that point. The total SO_2 amount for this particular point was 149.7 DU and the center height is 10.34 km.

The two cases considered for this analysis were the Raikoke and Kasatochi eruptions. These were chosen since there were multiple consecutive days of coverage from OMI with relatively strong SO_2 signals. Height retrievals for OMI Orbit 79463 (Raikoke) and Orbit 21650 (Kasatochi) were used to initiate the trajectory model. After the trajectory calculation, the

endpoints at 23, 46 and 69 hours are compared with the retrieved heights for the corresponding orbits during the following OMI overpasses.

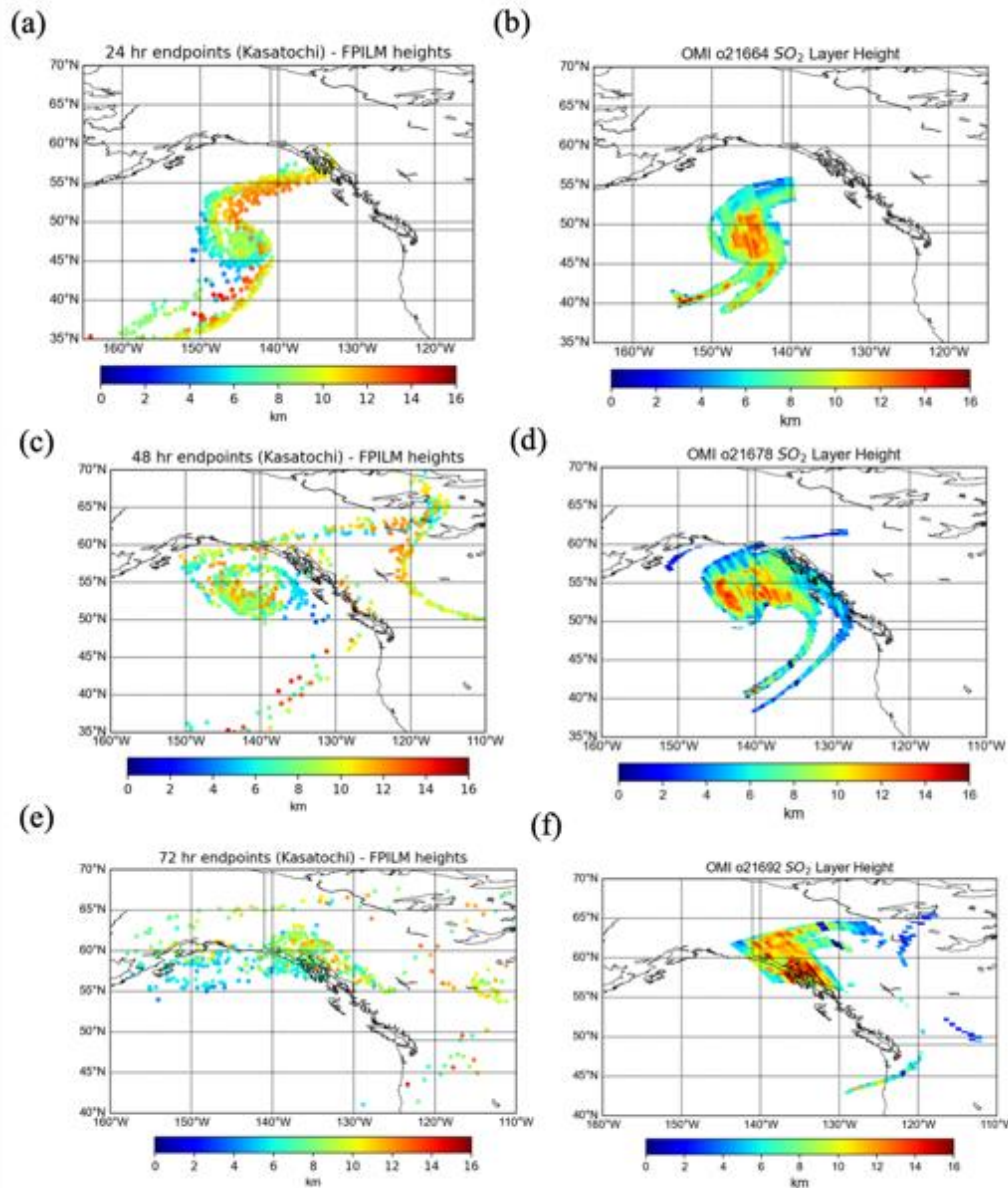


Figure 4.5: Trajectory endpoints of HYSPLIT calculations at (a) 23 hours, (c) 46 hours and (e) 69 hours from the OMI orbit 21650 observation. The points are color coded based on the height. The OMI SO₂ layer height retrieval for (b) orbit 21664, (d) orbit 21678 and (f) orbit 21992 are shown for comparison of each time frame. The HYSPLIT calculation was initialized at 01 UTC on August 10, 2008, which matches with the observation time of OMI orbit 21650.

For the Kasatochi eruption (Figure 4.5), the endpoints are spatially aligned with OMI observations, especially the portion with the densest cluster of points. Comparing the altitudes of the end points with height observations is more difficult. This is due to the fact that HYSPLIT calculations can vary based on meteorological conditions at different altitudes and low biases originating from the lower heights in the initial SO₂ profile. The third day shows the least agreement where the retrieved OMI heights for orbit 21692 are 12-14 km in a big bulk of the plume and only 10-12 km in the final trajectory endpoints. The trajectory error also likely increases in HYSPLIT by 15-30% of the distance traveled [Draxler and Rolph, 2007] thus making longer forecasts more uncertain. Lastly, there is some potential uncertainty due to the GDAS meteorological data used in this analysis as it is a relatively coarse resolution.

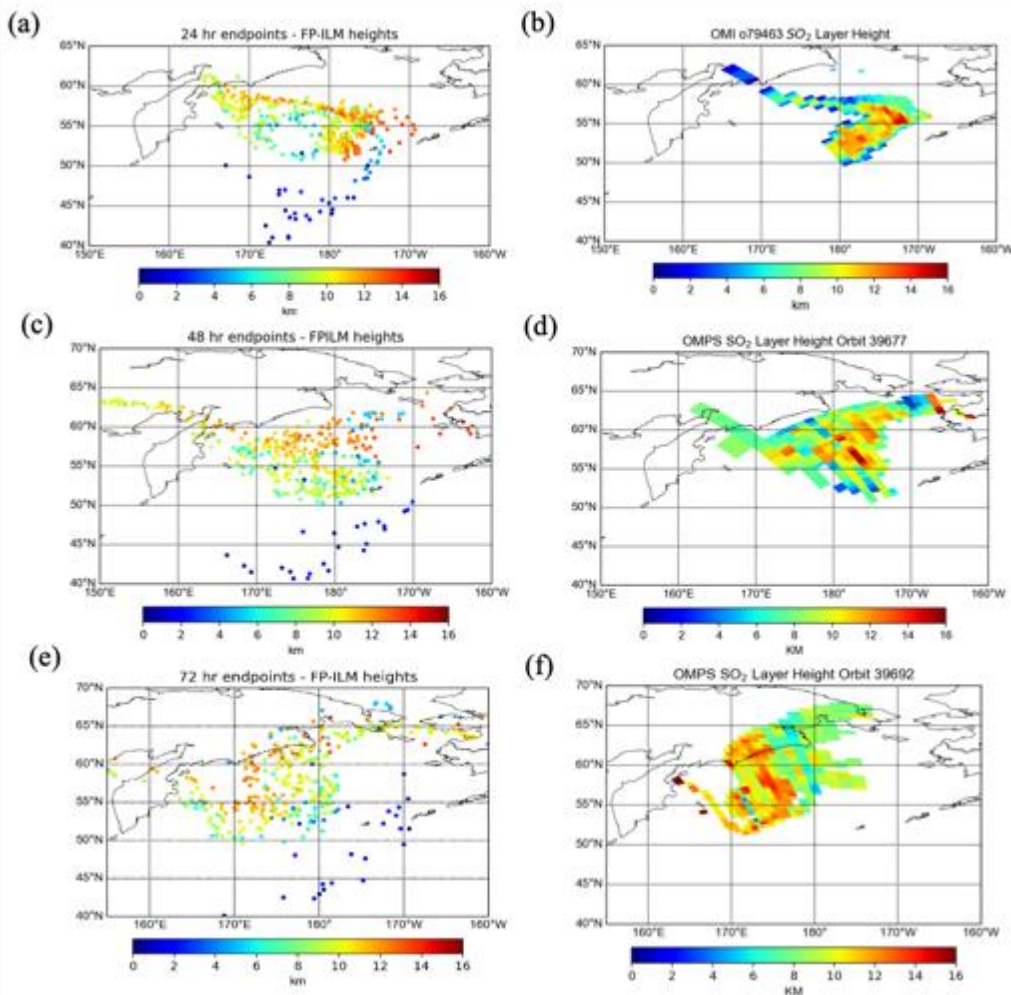


Figure 4.6: Trajectory endpoints from HYSPLIT calculations at (a) 23 hours, (c) 46 hours and (e) 69 hours for the Raikoke eruption. The points are color coded based on the height. The OMI SO₂ layer height retrieval for (b) orbit 79463, (d) OMPS orbit 39677 and (f) OMPS orbit 39692 are shown for comparison of each time frame. The HYSPLIT calculation was initialized at 1 UTC on June 23, 2019 at 00 UTC which matches with the observation time of OMI orbit 79449.

In the Raikoke case (Figure 4.6) the plume moved relatively slowly and did not move as far from the initial observation, staying between 50-60° N and 170-180° E. The trajectory results confirm this and are comparable to the OMI SO₂ height fields.

For more quantitative comparisons, I calculated the difference in the center of mass between the observed height retrieval field and the trajectory endpoints. I also compare this quantity between the FP-ILM starting altitudes and those from two reference model runs, one

using the OMI TRU product with a 13 km reference height to initiate the trajectory model, the other using the OMI TRM product with an 8 km reference height. For a 1-3 day forecast the error in the plume center between the OMI observation and the trajectory clusters is less than 150 km (Table 4.2). The TRU reference run had comparable results while the TRM reference run performed worse in forecasting the plume center. The plume center was defined as the center of mass of all points or pixels with an SO₂ VCD > 1 DU in the domain which was calculated as the weighted average location.

Table 4.2: Distances between the center of masses of the OMI observation and the modeled plume from HYSPLIT.

HYSPLIT Height Input	Raikoke distance from obs (24h traj) [km]	Raikoke distance from obs (48h traj) [km]	Raikoke distance from obs (72h traj)[km]	Kasatochi distance from obs (24h traj) [km]	Kasatochi distance from obs (48h traj) [km]	Kasatochi distance from obs (72h traj)[km]
FP-ILM	124	129	156	75	91	111
TRU Ref (13 km)	105	156	127	79	69	93
TRM Ref (8 km)	201	344	354	144	172	193

In order to account for the spread of the plume, the location metric [Prata et al., 2021] was used.

It is defined as:

$$L = L_1 + L_2 \quad (\text{Eq. 4.1})$$

The first term L_1 , is the difference in the center of mass of the plume between the HYSPLIT result and OMI height field. L_2 is the difference in weighted average distances of the two fields.

The average distance is obtained by taking the mean of the differences between the center of plume and each individual data point in the domain. After normalization, the metric L has a range of 0-2, with 0 representing a perfect agreement between the forecast and observed plumes.

Overall, the forecast using FP-ILM input has similar performance with the reference one using

the TRU (13-km) retrievals for model initialization (within 0.1 for all cases). The small difference in L may possibly be attributed to similar meteorological transport at the 13 km level and 10-11 km (FP-ILM retrieved height). It is also notable that based on the location metric the error is greater for the day 3 (69h) calculation. This shows that although the general location of the plume is well predicted by HYSPLIT, this method is most accurate for 1-2 day forecasts especially in a plume such as Kasatochi's, where it disperses and covers a large area.

Table 4.3: Location metric (L) for the FP-ILM inputs and the OMI TRU SO₂ Column Amount dataset at 23, 46, and 69 hour of the HYSPLIT trajectory calculation.

	Raikoke 23h	Kasatochi 23h	Raikoke 46h	Kasatochi 46h	Raikoke 69h	Kasatochi 69h
FP-ILM	0.1285	0.1495	0.211	0.155	0.283	0.526
TRU (13 km height)	0.154	0.195	0.1	0.118	0.303	0.5008

4.2.2 Reconstructed Vertical Profiles

After trajectory calculations, the vertical SO₂ profile can be reconstructed. Initially each starting point in the grid contains an amount of SO₂ based on the OMI SO₂ VCD data for the orbit. Assuming each grid point is an air parcel with that specific amount of SO₂, by tracking each parcel within HYSPLIT I can get an idea of where it will end up. Note that the SO₂ would be lost over time through various chemical and physical processes that are ignored in the present study. Despite this, the vertical distribution of SO₂ within the core part of the plume can be estimated using the HYSPLIT calculated trajectories. This was done by obtaining a sum of SO₂ amount for twenty nine 0.5 km layers between 4.5 and 18 km along a Gaussian distribution, excluding points that were originally outside of the main plume detected by OMI. The sums were normalized to show a relative weight for the profile (Figure 4.7). However, knowing the

approximate structure can be useful as a supplement to volcanic plume forecasts ahead for up to 48 hours.

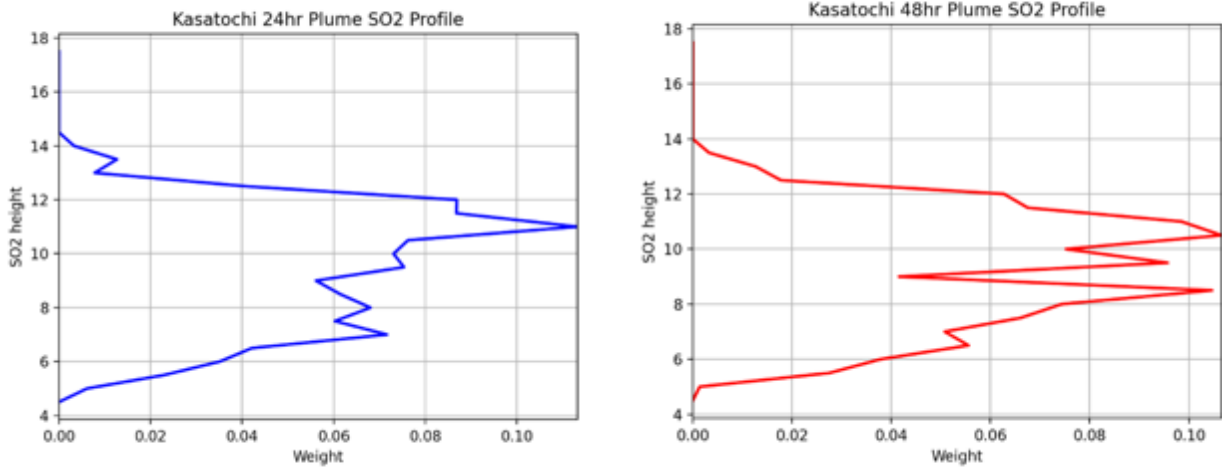


Figure 4.7: The reconstructed SO₂ vertical profile using trajectory endpoints for (a) 23 hours and (b) 46 hours. The profiles correspond to the points in Figure 4.4a and 4.3b respectively. The weight is a measure of how much each layer contributes to the total mass of the plume.

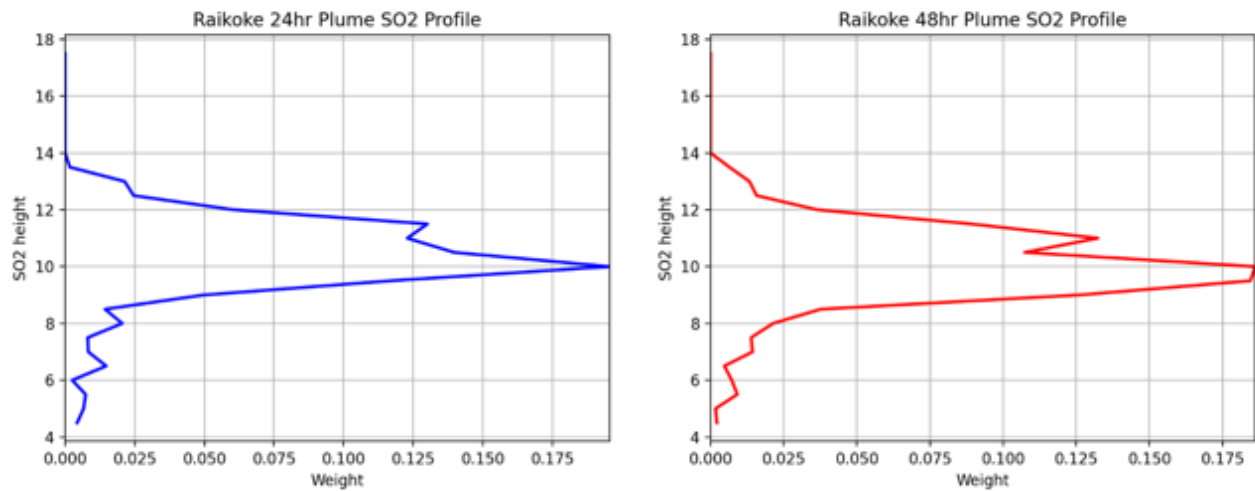


Figure 4.8: The reconstructed SO₂ vertical profile using trajectory endpoints for (a) 23 hours and (b) 46 hours. The profiles correspond to the points in Figure 4.4a and 4.4b respectively. The weight is a measure of how much each layer contributes to the total mass of the plume.

The reconstructed SO₂ profiles show that the dominant height in the Kasatochi case (Figure 4.7) is 11 km for both the 1 and 2 day trajectories. There are also low biases as evidenced by secondary peaks at around 8 km, which are expected given the known low biases in the original OMI SO₂ LH retrievals. The assumed Gaussian distribution in the starting heights also introduces lower initial heights into HYSPLIT. The Raikoke distribution (Figure 4.8) for both days shows a peak at around 10 km and smaller amounts of SO₂ above 12 km. As discussed in the SO₂ height retrieval results, this is lower than the TROPOMI estimates but agrees with the IASI retrieved heights. This is supported by a study [de Leeuw et al., 2021] which compares the emission profiles constructed from IASI observations (VolRes 1.5) with one based on TROPOMI VCDs (StratProfile); the former has a center height at 10 km with a smaller peak near 14 km, while in the latter, the largest portions of SO₂ are found at 12-13 km. In their simulations using these two profiles, the difference in center altitude caused different percentages of the SO₂ to be emitted into the lower stratosphere and upper troposphere. Overall the StratProfile agreed better with TROPOMI observation of peak mass burden and e-folding time. This shows that estimates of injection height are crucial for modeling the dynamics of the SO₂ plume.

4.2.3 Discussion

The results in sections 4.2.1 and 4.2.2 demonstrate how the SO₂ layer height retrievals can be integrated with HYSPLIT in order to forecast the movement and height of the plume up to 2-3 days with reasonable accuracy. The greatest advantage of this type of application is also the speed of the forecasts. Producing quick and reliable ways of tracking and forecasting volcanic plumes will be of great value for addressing aviation disruptions caused by these eruptions. As discussed previously, the FP-ILM height retrieval can be performed in a matter of minutes which makes it suitable for near real time operations. Likewise, HYSPLIT while less complex than

other models, has the advantage of speed in performing the trajectory calculations. Even for a big domain like the Kasatochi case where 9000 initial points were used, the trajectories can be calculated for 3 days in under 10 minutes. Therefore, it would be feasible to have an operational framework for this application (Figure 4.9). First, the OMPS SO₂ heights would be retrieved with the most recent OMPS Level 1 radiance data the product for which is readily available for operational use. By using available OMPS SO₂ Column Amount data, an automated script can determine if there is SO₂ above a certain threshold in order to initiate the plume tracking. The operational system would then set the domain of the grid based on the observed plume location. The gridded SO₂ LH data and grid coordinates would be fed into HYSPLIT, which would then perform the forward calculations for up to 72 hours. Note that only one model run is needed since the location and altitude data is calculated for each intermittent hour up to the maximum time (72h). A readily available meteorological dataset such as the output from the NCEP GFS with a 0.25° by 0.25° grid would be fed into HYSPLIT. After the trajectory calculations the endpoints can be re-gridded into a height field forecast for that particular time. Height profiles as shown in Figures 4.7 and 4.8 would also be obtained. This would provide information on the vertical distribution of the SO₂, and determine the most likely plume height for the desired forecast time. Errors in the initial SO₂ profile, in particular the center height can potentially affect the forecast accuracy. Since there is quite a bit of variation in the final altitude of trajectory endpoints, the reconstructed height profile can give better confidence for a probabilistic forecast. Note that the OMPS instrument should be used for operational application instead of OMI since it does not have row anomaly issues that can reduce spatial coverage. Nonetheless, future work on this application will need to address the issue of collocation of ash and SO₂ as it is the ash that poses the greatest risk to airplanes. While in many cases SO₂ can be used as a proxy for volcanic

ash, in some situations SO₂ can be separated from the ash plume especially if wind shear is present and the injection heights are different between the two species [Sears et al., 2012]. Additionally, ash has a shorter lifetime than SO₂ due to gravitational settlement. Therefore using a method like this in conjunction with ash plume models could be useful for volcanic plume forecasting.

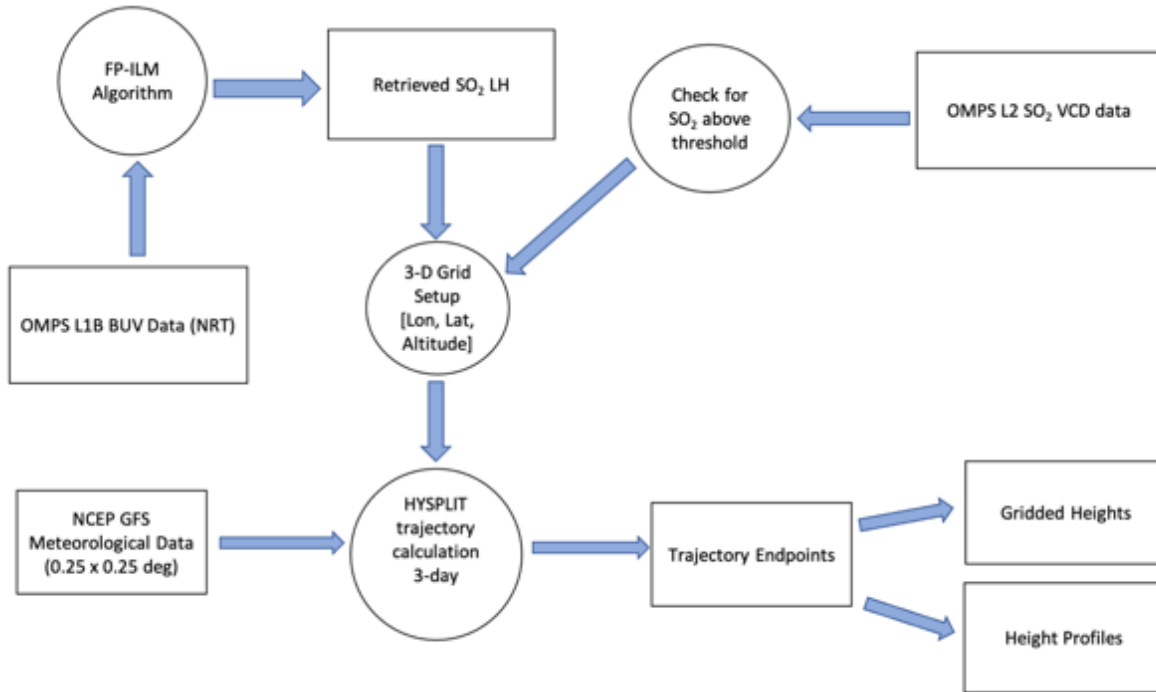


Figure 4.9: Flowchart of a potential operational volcanic SO₂ plume forecast system using HYSPLIT and retrieved OMPS SO₂ layer heights. Rectangles indicate datasets while circles indicate a computational step.

4.3 SO₂ Mass Estimates Using Retrieved Heights

The second application of FP-ILM OMI retrieval is using it in estimations of the total SO₂ mass in the plume. Determining the SO₂ mass from eruptions is important as it is used to determine the SO₂ flux from the volcano which in turn is used as an input to chemical models and data assimilation systems. It is also important to determine the amount of SO₂ being injected into the stratosphere where it can perturb the climate system. Obtaining the flux of SO₂ from volcanoes is

less straightforward and more challenging than the total mass. Flux can be estimated with one of three methods - the transect method, the delta-M method or the inverse method [Theys et al., 2013]. The transect method takes into consideration the variable wind speed and a defined transect perpendicular to the plume. Delta-M method requires successive satellite overpass data and aims to invert the mass conservation equation. Lastly, the inversion method requires additional dispersion models, for example the FLEXPART dispersion model [Stohl et al. 2005], and a known mass loading. On the contrary, SO₂ mass can be calculated directly from just satellite observations. The total mass is determined by calculating the sum of the mass for each individual OMI pixel. The individual pixel mass is the product of the VCD, area of the pixel and a conversion factor (1 DU = 0.02848 g SO₂ m⁻²)

$$Total\ Mass = \sum_{p=1}^n VCD_p * A_p * 0.02848 \quad (Eq\ 4.2)$$

For OMI, mass estimates can be obtained with the standard OMI SO₂ VCD products with an assumed reference height. In reality, the actual plume heights can be quite different from the assumed plume height in the standard VCD retrievals. Additionally, the heights of the SO₂ can be variable throughout the plume. Thus it is beneficial to use the retrieved heights to “correct” the SO₂ amounts and to account for height variations across the plume. In this case, the FP-ILM retrieved height would be used to generate a new VCD field that is interpolated from OMI standard SO₂ VCD retrievals assuming different reference heights. For example, a pixel with a retrieved height of 10 km would have a VCD value between the TRM VCD (assumed plume height of 8 km) and TRU VCD (assumed plume height of 13 km).

These calculations were performed for the Raikoke and Kasatochi cases in order to determine the total SO₂ mass of the plume for several days of the eruption in the following

section. Comparisons are also made with the OMPS instrument, as well as previous estimates in literature.

4.3.1 Raikoke Mass Estimates

The interpolated VCD field was calculated for OMI orbits 79449 and 79463 which correspond to June 23rd, 2019 at 00 UTC and June 24th, 2019 at 01 UTC. A noticeable difference between the two days is that the plume was more concentrated on the first of the two orbits as seen by the swath of VCD greater than 250 DU in the middle of the plume. On the following day the plume was more spread out and had VCDs of 100-200 DU, Based on the interpolated VCD fields (Figure 4.10), the calculated total SO₂ mass was 1.71 Tg and 1.633 Tg for June 23rd and June 24th, respectively (Table 4.4). Given that this is only a few days after the eruption, most of the SO₂ has not been oxidized and dispersed, hence the similar total mass for the two days. The same mass calculation was also done with SNPP/OMPS for comparison. For the first day, the calculated total mass for OMPS orbit 39649 was 1.602 Tg while for the second day it was 1.66 Tg (Table 4.4). This agrees well with the OMI estimates, indicating consistent VCD retrievals with the same PCA-based algorithm between the two instruments. The mass estimates also agree with recent findings using the TROPOMI and IASI instrument [de Leeuw et al., 2021]. This study found peak loadings of around 1.5 ± 0.2 Tg for the Raikoke eruption during the early stages of the eruption with 0.4-0.7 Tg injected into the lower troposphere and 0.9-1.1 Tg into the lower stratosphere. These values were based on IASI observations and the Volcanic Response (VolRes) emission profile. The estimates for a SO₂ profile derived with TROPOMI VCD observations were 1.4-1.6 Tg.

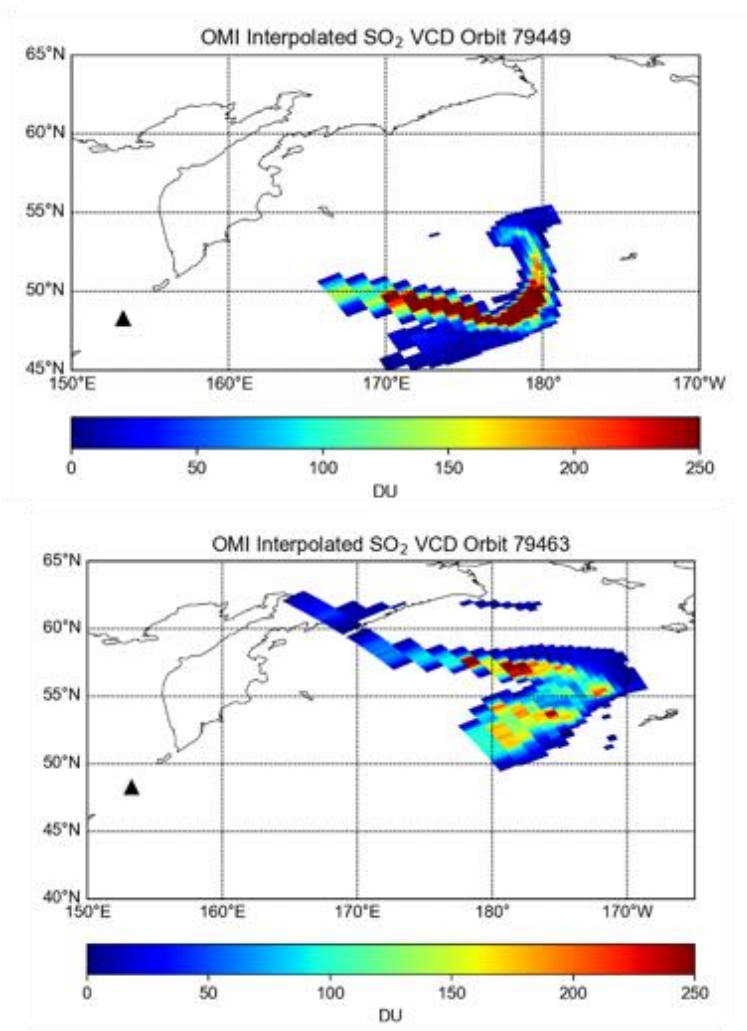


Figure 4.10: The OMI Column Amounts calculated by interpolating the FP-ILM retrievals with the standard SO₂ products for (a) June 23rd at 2352 UTC (OMI orbit 79449) and (b) June 24th, 2019 (OMI orbit 79463) at 0045 UTC. All pixels with VCD > 5 DU are shown.

Table 4.4: Estimated total SO₂ mass of the interpolated VCD field, the TRM (8 km reference) product and TRU (13 km reference) product for two days of the Raikoke eruption. The OMI estimates are calculated with orbit 79449 and 79463 and orbits 39649 and 39663 for OMPS.

	FP-ILM OMI	8 km standard OMI	13 km standard OMI	FP-ILM OMPS	8 km standard OMPS	13 km standard OMPS
Raikoke Day 1	1.711	2.031	1.426	1.615	1.642	1303
Raikoke Day 2	1.633	1.654	1.425	1.601	1.701	1395

4.3.2 Kasatochi Mass Estimates

For the Kasatochi case, the SO₂ estimates were calculated for four orbits on the days of August 9-13th, 2008. In this plume, there was considerable movement compared to Raikoke due to the presence of a low pressure pattern that drifted the plume into northwestern Canada and caused the plume to swirl counterclockwise. As seen below the plume is highly concentrated for Orbit 21650 at 00Z on August 10th, but rapidly spreads out over the following days (Figure 4.) to the east. The density of the plume also decreases from around the 650 DU peak for orbit 21650 to 240 DU for orbit 21692. Mass estimates also have a reduction over the course of the four days (Table 4.5). The total estimates are 2.22, 1.54, 1.17 and 1.04 Tg for a, b, c and d respectively in Figure 4.11. Over the four days there is a fairly large range of mass estimates between 1-2.2 Tg. This change may be due to evolution of the plume over time with portions of the SO₂ being oxidized or transported away from the main bulk of the plume. For the last orbit the plume had been spread much thinner in which case the SO₂ signal would be harder to detect in the height retrieval. As a result, since the same SO₂ VCD threshold was used in the calculation for all days, there may be some low biases in the mass estimate for days 3 and 4.

The OMI estimates are generally in line with previous total mass estimates from other instruments. For two IR-based instruments, AIRS and IASI, estimates of 1.2 Tg [Prata et al., 2010; Kristiansen et al, 2010] and 1.7 Tg [Karagulian et al., 2010] were obtained respectively. With GOME-2 peak loadings of 2.5 Tg were reported [Richter et al., 2009], which is substantially higher than the average over the four orbits, but still quite similar to calculated 2.2 Tg in orbit 21650. Given the consensus of all the estimates, it is likely that Kasatochi plume reached a peak loading of 1.5-2.0 Tg in the few days after the eruption.

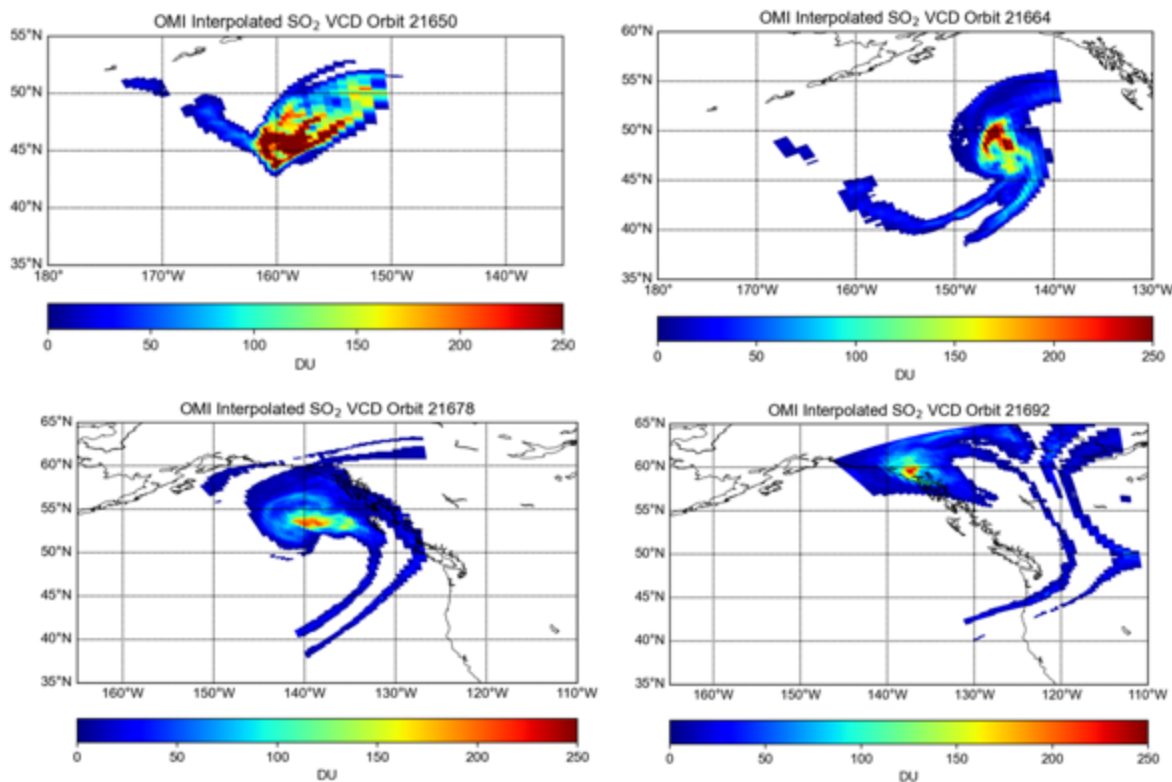


Figure 4.11: The OMI Column Amounts calculated by interpolating the FP-ILM retrievals with the standard SO₂ products for (a) August 10th at 0000 UTC, (b) August 10th, at 2300 UTC, (c) August 11th at 2215 UTC and (d) August 12th at 2125 UTC.

It is also important to compare the differences in total mass when calculating the SO₂ mass using the standard VCD product versus the interpolated field. The mass estimates of all orbits of Kasatochi and Raikoke are provided in Table 4.3. The differences between the interpolated field and the closest reference heights (8 and 13 km) are generally within 0.2-0.3 Tg for all cases. However, without the interpolated field, for some orbits such as 21650 and Day 1 of Raikoke (orbit 79449), the difference can be as large as 0.6 Tg. In general, the SO₂ mass is a fairly precise quantity between instrument, assuming the height is correct. If the height is off, the difference in SO₂ total mass can be fairly significant and can make an influence on the SO₂ flux calculation and model simulations that use this data. Therefore, there is some benefit in using the

retrieved plume heights to adjust the VCD field for the mass calculations. In the comparisons it is also worth noting that the low bias in the height retrievals can also affect the mass estimates. Since the low SO₂ height pixels with sufficiently high SO₂ amounts are included in the calculation, the resulting total SO₂ mass is closer to the 8 km reference height mass than the 13 km due to larger contribution from those pixels. This issue will be resolved once the issue with low biases is diagnosed.

This analysis leaves opportunities for future work. The interpolation method in this case is simple but can be less accurate than other methods. Another way to update the VCD data would be to use the retrieved heights to improve SO₂ Jacobian or AMF calculations (which depend on SO₂ height) and to use the refined SO₂ Jacobians in VCD retrievals. This will improve the accuracy of SO₂ Jacobians and further improve the accuracy of the SO₂ VCD retrievals.

Table 4.5: Estimated total SO₂ mass of the interpolated VCD field, the TRM (8 km reference) product and TRU (13 km reference) product for 4 OMI orbits of the Kasatochi eruption.

	Total Mass using Interpolated VCD (Tg)	Total mass using TRM VCD (Tg)	Total Mass using TRU VCD (Tg)
Orbit 21650	2.225	2.341	1.656
Orbit 21664	1.494	1.583	1.286
Orbit 21678	1.143	1.203	1.055
Orbit 21692	1.038	1.020	0.440

4.4 Conclusions

In this chapter, some potential applications of the FP-ILM retrieval were discussed. In section 4.1, the FP-ILM was applied to the SNPP/OMPS and NOAA20/OMPS instruments which are crucial for continuing the data record of SO₂ from volcanic eruptions. The process to retrieve height for the two instruments was mostly identical to OMI, but involves using the instrument-specific slit function to convolve synthetic data and retraining the neural network. Results showed lower retrieved heights for the NOAA20/OMPS than the other instruments where the mean of the retrieval was around 9 km as compared with retrieved heights of 10-10.5 km with OMI and SNPP/OMPS. One potential application of the retrieval is to use it in an operational setting where the height of the SO₂ layer help to improve forecasts of volcanic plumes for aviation safety. I conducted HYSPLIT trajectory simulations using the FP-ILM heights as input for up to 3 days. In this analysis, the model did well in predicting the position and heights of the plume for up to 69 hours, although with increasing error over time. I also constructed SO₂ profiles from trajectory end points at 23 and 46 h after trajectory initialization. For Kasatochi and Raikoke cases both 23h and 46h the reconstructed profiles had a center height of 11 km and 10 km respectively, with the latter being biased low as compared with CALIPSO and TROPOMI. In general, having fast and efficient tools such as a trajectory model and the NRT height retrieval algorithm can improve the forecasts for volcanic disaster monitoring and mitigation. The other section of this chapter focused on SO₂ mass estimates. The mass depends on the VCDs that are retrieved from OMI, however there is a substantial difference in estimated mass depending on which reference height is used in VCD retrievals. Interpolating with the height field can therefore slightly improve mass estimates. Between the TRM and TRU SO₂ datasets, there can be a difference of greater than 0.5 Tg for a large eruption which shows the

need for introducing an observed height field into mass calculations. The OMI total mass estimates using the retrieved heights were comparable with estimates from literature as well as those from the OMPS instrument. Overall, the results in this chapter highlight the potential benefits of the having an operational, fast SO₂ height retrieval. With the future availability of NRT data, an increase in speed of applications such as volcanic plume tracking, data assimilation and SO₂ flux estimates can be expected.

Chapter 5 Overall Conclusions

5.1 Summary of research

The research presented in this dissertation focuses on two different aspects of sulfur dioxide. The first component deals with the anthropogenic emissions of SO₂, in particular how reductions in SO₂ pollution have led to decreases in sulfate deposition. To this end, I found the contribution of source areas to improvements in sulfate deposition downwind using trajectory analysis, OMI data and ground based measurements. The second component deals with natural emissions of SO₂ from volcanoes, which can have significant impacts on air travel as well as climate. Here my primary objective was to develop a highly efficient SO₂ layer height retrieval algorithm for OMI and OMPS using only BUUV measurements and viewing geometry. Chapter 4 is an extension of this work where I provided some examples of potentially useful applications for the OMI/OMPS SO₂ height retrievals. In all these studies I have made use of data from OMI and OMPS instruments.

In Chapter 2, trends in annual mean OMI SO₂ VCDs and sulfate wet deposition were calculated for the period 2005-2015. Over the 10-year period, SO₂ VCDs decreased by around -0.020 DU yr⁻¹ in areas along the Ohio River where there were a number of coal power plants. The sulfate wet deposition reduction in the same ten-year period was in the range between -16 and -12 kg S hectare⁻¹ over a larger portion of the study domain in the Eastern U.S, with the biggest negative trends of 18-20 kg S hectare⁻¹ in some locations. At all of the five National Atmospheric Deposition Program (NADP) sites that I selected for case studies, the sulfate wet deposition decreased by at least 50% from 2005 to 2015. The HYSPLIT model was then used to calculate 72 h back trajectories from the NADP sites, initialized at 500 m above the ground. Since the SO₂ and sulfate deposition are not spatially correlated, the PSCF method was used to

connect the areas of SO₂ origin to the ground receptor sites. Using the PSCF along with the trends of SO₂ and sulfate deposition, I obtained a percent contribution of each grid cell to the sulfate deposition trend at each NADP/AQS site. The contributing source regions for each site reflect the dominant flow pattern shown by the trajectories and the areas of negative SO₂ column trend observed by OMI. A seasonal dependence was also found because of the prevailing westerly wind in winter changing to a more variable direction in summer. The strongest contribution to the sulfate trend is from west of the sites in winter months, but during summer months some contribution comes from the east as well. This seasonality can also be attributed to faster oxidation of SO₂ in the summer, when contributing grid cells are closer to the receptor sites. In the case of the Beltsville, MD site, in winter roughly 2/3 of the contribution to the deposition trend is from the west and from sources greater than 500 km away. In summer, however, most of the contribution was from within 300 km, consistent with weaker winds and faster SO₂ oxidation. For the AQS site in Hackney, OH, the SO₂ sources are much closer, and the seasonal pattern is much less pronounced: 80% of the contribution to sulfate trend comes from within 400 km from the site for both summer and winter, although summer months do see some more contribution from the east instead of west. The differing results for the two sites shows that the proximity to sources and weather patterns influence the sulfate deposition occurring at a given location. However, the main idea remains the same - pollution controls for coal-fired power have led to dramatic improvements in sulfate wet deposition in the eastern United States both near the source and further downwind. The effect of state legislations is also noticeable in the data such as the case of the Maryland Healthy Act which reduced SO₂ emissions from power plants by over 80%. The PSCF and source-receptor analysis for the Beltsville site showed that between 2008-2012, the largest contribution to the sulfate deposition trend came from nearby

sources, even during winter months. During this time period both dry and wet sulfate flux decreased drastically which indicates that the pollution controls also indirectly affected the dry deposition.

The other component of my research is centered around volcanic SO₂ layer height retrieval (FP-ILM) for OMI. The SO₂ layer height is important because it can be used as a proxy for tracking the height of volcanic ash plumes, which are major hazards for aviation and air travel. The SO₂ height is also a crucial input needed for volcanic plume forecasting and data assimilation. Lastly, the height can also aid in assessing the impacts of volcanic eruptions on radiative forcing. The SO₂ LH retrieval algorithm was trained through a neural network with thousands of synthetic BUV spectra and physical parameters for varying conditions. The OMI BUV radiances were input to the trained inverse model to obtain the heights. The height retrieval results were tested for 4 eruptions and all of them agreed with other sensors within the 2 km uncertainty range. The algorithm estimated 10-12 km height for Kasatochi is in agreement with the IASI instrument and previous OMI height estimates of 9-11 km in Yang et al. [2010]. For the 2015 Calbuco and 2014 Kelud eruptions, heights were found to be around 15-17 km and 18-19 km, respectively. Although a direct comparison with CALIPSO was not possible in these cases due to the lost OMI spatial coverage related to instrument anomaly, for the same plume CALIPSO showed an ash plume at 17 km for Calbuco and 19.5 km for Kelud. Lastly for the 2019 Raikoke eruption, the OMI retrieval indicated SO₂ heights of 11-12 km for the densest part of the plume, again in agreement with IASI and CALIPSO.

This algorithm could also be applied to SNPP/OMPS and NOAA20/OMPS instruments (Section 4.1), provided that the spectra were treated with the unique slit functions of each instrument. In Chapter 4 I also demonstrated two potential applications of the height retrievals.

The first one is volcanic plume forecasting. When provided as an input into HYSPLIT, the retrieved SO₂ heights can help to produce reasonably accurate forecasts on the location of the plume for up to 2 days from the initialization time. SO₂ height retrievals can also be used to refine the estimates of total SO₂ mass loading in a plume for a given OMI (or OMPS) orbit. By using the retrieved SO₂ heights, I estimated that the SO₂ mass from the Kasatochi eruption was nearly 2 Tg on August 10th, 2008 and then reduced to around 1.1 Tg over the following days as the plume was oxidized, and was transported and dispersed to the east. The Raikoke plume had totals of around 1.7 Tg and 1.4 Tg on June 24th and June 25th, 2019 respectively, which was within 0.25 Tg of OMPS and TROPOMI estimates. The difference in estimated total mass between using fixed height and retrieved height was also apparent, where in some cases they varied by more than 0.2 Tg. For some orbits, the mass estimates using the OMI VCDs refined with the retrieved heights were closer to the total mass found by other instruments, compared to OMI estimates using a fixed height. These results showed that more accurate height input can lead to improved SO₂ mass loading estimates.

5.2 Future Work

Additional work can lead to improvement in quality of results and to further applications. For the sulfate deposition trend study, future work can incorporate further chemical transport models in addition to the existing statistical method used in the study. Additional meteorological analyses can also be useful in determining the role of seasonal precipitation patterns and climatology on wet deposition rates. One such analysis could be linking varying magnitudes of precipitation events and weather systems to the uptick in sulfate wet deposition, on a smaller time scale. The results focused on the differences between summer and winter seasons, however

the analysis can also be extended to spring and fall seasons. A larger number of sites and extension of the trajectory climatology to more than 5 years may increase the robustness and accuracy of the results. The methods presented here may prove useful in areas that are experiencing large changes in sulfur pollution such as East Asia or South Asia and could help guide the selection of key targets for pollution control. The method can be particularly useful for in situ data-poor areas, given that satellite data will help to capture the fast-paced changes in emissions and provide more frequent updates than conventional bottom-up emission inventories. Lastly, other forms of acid deposition can be explored, for instance, nitrogen deposition which stems from NO_x pollution.

The height retrieval algorithm presented in this dissertation has shown promising results but can be further optimized to improve the accuracy of the retrievals and reduce the uncertainties. One assumption is that ash and sulfur dioxide plumes are mostly collocated when using CALIPSO as a source to verify the plume height. Although this is often true at the initial stage of many eruptions, dispersion of the plume and gravitational settling of the ash in the following days can separate the two effluents. Therefore, tracking these plumes becomes challenging when using reflectance spectra alone; further analysis may need to include trajectory modeling and wind data to simulate the movement of the ash. The neural network model was trained on synthetic spectra calculated for molecular atmosphere conditions in the absence of aerosols. The impact of including aerosols in the simulations is another subject for a follow-up study as aerosols complicate the radiative transfer calculations. Another potential improvement is to generate data sets of synthetic spectra using a vector RRS model to account for polarization as well as adding significantly more spectra with low SO_2 VCDs into the training. This may help in reducing the low bias in the results and overall increase the performance of the retrievals at low

SO₂ amounts (< 30 DU), common in small to moderate volcanic eruptions. Further analysis is also needed for determining effect of the SO₂ and ozone profiles used for the LIDORT-RRS model calculations. For instance, using different sets of ozone climatological profiles or varying shapes and FWHM in the constructing the SO₂ profile would be a helpful in better determining the impact of assumed *a priori* profiles on the generating the spectral dataset and algorithm results. For improving the performance and efficiency of the machine learning, the use of neural network ensembles and a further optimized setup of NN structure and parameters will be explored. These parameters may include the number of hidden nodes, regularization techniques and activation function types. I may also reassess the number of PCs used in training as more may be needed for optimal performance than the eight PCs used in the study. The FP_ILM algorithm has the potential to be applied operationally to the OMPS instruments although further optimizing the quality of the retrievals is necessary.

The results of this work show the benefit of using both satellites and ground monitoring for observing SO₂ and its effects. Some of the next generation of VIS/UV satellite instruments will be onboard geostationary satellites and allow for multiple observations per day over an area of interest as opposed to polar orbiting satellites. Some examples of this are the Geostationary Environmental Monitoring Spectrometer (GEMS) launched by South Korea, NASA's TEMPO instrument, and the Sentinel-4 from the European Space Agency. Through these future improvements in the capabilities and coverage of satellite instruments, the coverage in observing networks, and cutting edge retrieval methods, the speed and quality of information about not only SO₂ but other important atmospheric species can be greatly enhanced.

Appendix: Chapter 2 Supplementary Tables

Table A1: Cumulative distribution of winter (DJF) percent contribution to SO₄²⁻ deposition trend at the Beltsville, MD site within given ranges from the site. The totals are summed through each distance range and are broken up by direction with respect to the longitude of the site. The first column is the distance range from the site over which the contribution of grid boxes is summed. The last column is the percent contribution for only the single distance range, not the cumulative amount.

Distance from Site (km)	East	West	Total	Incremental difference (between two radii)
0-50	3.11	0.24	3.35	3.35
50-100	17.04	1.74	18.78	15.43
100-200	33.1	11.34	44.44	25.66
200-300	34.31	21.67	55.98	11.54
300-400	35.51	35.54	71.05	15.07
400-500	35.62	41.88	77.5	6.45
500-1000	35.62	62.41	98.03	20.53

Table A2: Same as Table A.1 but for summer (JJA)

Distance from Site (km)	East	West	Total	Incremental difference (between two radii)
0-50	0.00	0.00	0.00	0.00
50-100	0.81	2.09	2.90	2.90
100-200	27.86	14.11	41.97	39.07
200-300	63.05	19.47	82.52	40.55
300-400	66.36	19.47	85.83	3.31
400-500	65.34	21.02	86.36	0.53
500-1000	66.37	32.87	99.24	12.88

Table A3: Cumulative distribution of winter (DJF) percent contribution to SO₄²⁻ wet deposition trend at the Hackney, OH site within given ranges from the site. The totals are summed through each distance range and are broken up by direction with respect to the longitude of the site. The first column is the distance range from the site over which the contribution of grid boxes is summed. The last column is the percent contribution for only the single distance range, not the cumulative amount.

Distance from Site (km)	East	West	Total	Incremental difference (between two radii)
0-50	4.93	5.94	10.87	8.71
50-100	6.91	16	22.91	12.04
100-200	9.01	38.16	47.17	24.26
200-300	9.09	53.96	63.05	15.88

300-400	9.09	67.9	76.99	13.94
400-500	9.28	76.62	85.9	8.91
500-1000	9.28	90.72	100	14.1

Table A4: Same as Table A.3 but for summer (JJA)

Distance from Site (km)	East (%)	West (%)	Total (%)	Incremental difference (between two radii)
0-50	2.95	1.75	4.70	4.703
50-100	5.56	5.438	11.00	6.297
100-200	18.14	20.67	38.81	27.81
200-300	29.10	37.01	66.11	27.3
300-400	31.16	47.06	78.22	12.11
400-500	31.70	54.73	86.43	8.205
500-1000	31.87	67.15	99.02	12.595

References

- Baumgardner, R.E., Lavery, T.F., Rogers, C.M., Isil S.S. (2002). Estimates of the atmospheric deposition of sulfur and nitrogen species: Clean air status and trends network, 1990–2000. *Environmental Science & Technology*, 36(12), 2614–2629. doi:10.1021/es011146g.
- Begum, B. A., Kim, E., Jeong, C.-H., Lee, D.-W., & Hopke, P. K., (2005): Evaluation of the potential source contribution function using the 2002 Quebec forest fire episode. *Atmospheric Environment*, 39(20), 3719–3724. doi: 10.1016/j.atmosenv.2005.03.008
- Bernard, A., and Rose, W. I. (1990): The injection of sulfuric acid aerosols in the stratosphere by the El Chichón volcano and its related hazards to the international air traffic, *Nat. Hazards*, 3(1), 59–67, doi: 10.1007/BF00144974.
- Bluth, G., Doiron, S., Schnetzler, C., Krueger, A. and Walter, L. (1992): Global tracking of the SO₂ clouds from the June, 1991 Mount Pinatubo eruptions. *Geophysical Research Letters*. 19, doi:10.1029/91GL02792.
- Bogumil, K., Orphal, J., Homann, T., Voigt, S., Spietz, P., Fleischmann, O. C., Vogel, A., Hartmann, M., Bovensmann, H., Frerick, J., and Burrows, J. P. (2003): Measurements of molecular absorption spectra with the SCIAMACHY pre-flight model: Instrument characterization and reference data for atmospheric remote sensing in the 230-2380 nm region, *J. Photochem. Photobiol. A: Chem.* 157, 167-184, doi: 10.1016/S1010-6030(03)00062-5.
- Brook, J.R, Samson P.J, Sillman, S. (1994): A meteorology-based approach to detecting the relationship between changes in SO₂ emission rates and precipitation concentrations of sulfate. *Journal of Applied Meteorology*, 33, pp. 1050-1066. doi: 10.1175/1520-0450(1994)033<1050:AMBATD>2.0.CO;2
- Burrows, J. P., Weber, M., Buchwitz, M., Rozanov, V., Ladstätter-Weißenmayer, A., Richter, A., et al. (1999). The Global ozone monitoring experiment (GOME): Mission concept and first scientific results. *Journal of the Atmospheric Sciences*, 56(2), 151– 175.

- Butler, T.J., Likens, G.E., Stunder, B.J. (2001). Regional-scale impacts of Phase I of the Clean Air Act Amendments in the USA: The relation between emissions and concentrations, both wet and dry. *Atmospheric Environment*. 35(6). 1015–1028. doi: 10.1016/S1352-2310(00)00386-1
- Carn, S.A., Krueger, A.J., Krotkov, N.A. et al (2009). Tracking volcanic sulfur dioxide clouds for aviation hazard mitigation. *Nat Hazards* 51, 325–343, <https://doi.org/10.1007/s11069-008-9228-4>.
- Carn, S., Fioletov, V., McLinden, C. et al. (2017): A decade of global volcanic SO₂ emissions measured from space. *Sci Rep* 7, 44095, <https://doi.org/10.1038/srep44095>.
- Carn, S. (2021): Multi-Satellite Volcanic Sulfur Dioxide L4 Long-Term Global Database V4, Greenbelt, MD, USA, Goddard Earth Science Data and Information Services Center (GES DISC), Accessed: Dec 2020 doi:10.5067/MEASURES/SO2/DATA405
- Casadevall, T.J., Delos Reyes, P.J., Schneider, D.J. (1996): The 1991 Pinatubo eruptions and their effects on aircraft operations. In: Newhall CG, Punongbayan RS (eds) *Fire and Mud: eruptions and lahars of Mount Pinatubo, Philippines*. Philippines Institute of Volcanology and Seismology/University of Washington Press, Quezon City/Seattle, pp 625–636.
- Chance, K., and Kurucz, R. L. (2010): An improved high-resolution solar reference spectrum for Earth's atmosphere measurements in the ultraviolet, visible, and near infrared, *J. Quant. Spectrosc. Radiat. Transfer*, 111, 1289–1295, doi:10.1016/j.jqsrt.2010.01.036.
- Charles T. Driscoll, Gregory B. Lawrence, Arthur J. Bulger, Thomas J. Butler, Christopher S. Cronan, Christopher Eagar, Kathleen F. Lambert, Gene E. Likens, John L. Stoddard, Kathleen C. Weathers. *Acidic Deposition in the Northeastern United States: Sources and Inputs, Ecosystem Effects, and Management Strategies: The effects of acidic deposition in the northeastern United States include the acidification of soil and water, which stresses terrestrial and aquatic biota*, *BioScience*, Volume 51, Issue 3, 1 March 2001, pp 180–198. doi: 10.1641/0006-3568(2001)051[0180:ADITNU]2.0.CO;2
- Chen, L. W. A., Doddridge, B. G., Dickerson, R. R., Chow, J. C., & Henry, R. C. (2002). Origins of fine aerosol mass in the Baltimore–Washington corridor: Implications from

- observation, factor analysis, and ensemble air parcel back trajectories. *Atmospheric Environment*, 36, 4541–4554. doi: 10.1016/S1352-2310(02)00399-0
- Clarisse, L., Coheur, P. F., Prata, A. J., Hurtmans, D., Razavi, A., Phulpin, T., Hadji-Lazaro, J., and Clerbaux, C. (2008): Tracking and Quantifying Volcanic SO₂ with IASI, the September 2007 Eruption at Jebel at Tair, *Atmospheric Chemistry & Physics* 8: 7723–7734. doi:10.5194/acp-8-7723-2008.
- Clarisse, L., Hurtmans, D., Clerbaux, C., Hadji-Lazaro, J., Ngadi, Y., and Coheur, P.-F. (2012): Retrieval of sulphur dioxide from the infrared atmospheric sounding interferometer (IASI), *Atmos. Meas. Tech.*, 5, 581–594, <https://doi.org/10.5194/amt-5-581-2012>.
- Clarisse, L., Coheur, P. F., Theys, N., Hurtmans, D., and Clerbaux, C. (2014): The 2011 Nabro eruption, a SO₂ plume height analysis using IASI measurements, *Atmos. Chem. Phys.*, 14, 3095–3111, <https://doi.org/10.5194/acp-14-3095-2014>.
- Daumont, D., Brion, J., Charbonnier, J., and Malicet, J. (1992): Ozone UV spectroscopy. I: Absorption cross-sections at room temperature, *J. Atmos. Chem.*, 15, 145 – 155, doi:10.1007/BF00053756.
- de Laat, A. and Vazquez-Navarro, M., Theys, N. and Stammes, P. (2020): Analysis of properties of the 19 February 2018 volcanic eruption of Mount Sinabung in S5P/TROPOMI and Himawari satellite data. *Natural Hazards and Earth System Sciences*, 20, pp. 1203-1217. Copernicus Publications. doi: 10.5194/nhess-20-1203-2020. ISSN 1561-8633.
- De Leeuw, J., Schmidt, A., Witham, C. S., Theys, N., Taylor, I. A., Grainger, R. G., Pope, R. J., Haywood, J., Osborne, M., and Kristiansen, N. I. (2021): The 2019 Raikoke volcanic eruption – Part 1: Dispersion model simulations and satellite retrievals of volcanic sulfur dioxide, *Atmos. Chem. Phys.*, 21, 10851–10879, <https://doi.org/10.5194/acp-21-10851-2021>.
- Draxler, R.R. and Rolph, G. D. (2007): HYSPLIT-WEB Short Course, National Air Quality Conference, Feb. 11, 2007, https://www.arl.noaa.gov/documents/workshop/NAQC2007/HTML_Docs/trajerro.html
- Driscoll, C.T., Driscoll, K.M., Roy, K.M., Mitchell, M.J., 2003. Chemical response of lakes in the Adirondack region of New York to declines in acid deposition. *Environmental Science and Technology* 37 (10), pp 2036-2042. doi: 10.1021/es020924h

- Dutkiewicz, V. A.; Das, M.; Husain, L. The relationship between regional SO₂ emissions and downwind aerosol sulfate concentrations in the northeastern U.S., *Atmos. Environ.* 2000, 34, 1821- 1832. doi: 10.1016/S1352-2310(99)00334-9
- Efremenko, D. S., Loyola R., D. G., Hedelt, P., and Spurr, R. J. D. (2017): Volcanic SO₂ plume height retrieval from UV sensors using a full-physics inverse learning machine algorithm, *International Journal of Remote Sensing*, 38, 1–27, <https://doi.org/10.1080/01431161.2017.1348644>.
- Eskes, H. J. and Boersma, K. F. (2003): Averaging kernels for DOAS total-column satellite retrievals, *Atmos. Chem. Phys.*, 3, 1285–1291, <https://doi.org/10.5194/acp-3-1285-2003>
- Fedkin, N. M., Li, C., Krotkov, N. A., Hedelt, P., Loyola, D. G., Dickerson, R. R., and Spurr, R. (2021): Volcanic SO₂ effective layer height retrieval for the Ozone Monitoring Instrument (OMI) using a machine-learning approach, *Atmos. Meas. Tech.*, 14, 3673–3691, <https://doi.org/10.5194/amt-14-3673-2021>.
- Fedkin, N. M., Li, C., Dickerson, R. R., Canty, T., Krotkov, N. A. (2019): Linking improvements in sulfur dioxide emissions to decreasing sulfate wet deposition by combining satellite and surface observations with trajectory analysis, *Atmos. Environ*, Volume 199, pp 210-223, <https://doi.org/10.1016/j.atmosenv.2018.11.039>.
- Fioletov, V. E., C. A. McLinden, N. Krotkov, M. D. Moran, and K. Yang (2011): Estimation of SO₂ emissions using OMI retrievals, *Geophys. Res. Lett.*, **38**, L21811, doi: 10.1029/2011GL049402.
- Fioletov, V. E., McLinden, C. A., Krotkov, N., and Li, C (2015) : Lifetimes and emissions of SO₂ from point sources estimated from OMI, *Geophys. Res. Lett.*, 42, 1969–1976, doi:10.1002/2015GL063148.
- Fioletov, V., McLinden, C. A., Griffin, D., Theys, N., Loyola, D. G., Hedelt, P., Krotkov, N. A., and Li, C. (2020): Anthropogenic and volcanic point source SO₂ emissions derived from TROPOMI onboard Sentinel 5 Precursor: first results, *Atmos. Chem. Phys.*, 20, 5591–5607, <https://doi.org/10.5194/acp-20-5591-2020>
- Fisher, B. L., Krotkov, N. A., Bhartia, P. K., Li, C., Carn, S. A., Hughes, E., & Leonard, P. J. T. (2019). A new discrete wavelength backscattered ultraviolet algorithm for consistent

volcanic SO₂ retrievals from multiple satellite missions. *Atmospheric Measurement Techniques*, 12(9), 5137–5153. <https://doi.org/10.5194/amt-12-5137-2019>

Flynn, L., Long, C., Wu, X., Evans, R., Beck, C. T., Petropavlovskikh, I., McConville, G., Yu, W., Zhang, Z., Niu, J., Beach, E., Hao, Y., Pan, C., Sen, B., Novicki, M., Zhou, S., and Seftor, C. (2014): Performance of the Ozone Mapping and Profiler Suite (OMPS) products, *J. Geophys. Res.-Atmos.*, 119, 6181– 6195, <https://doi.org/10.1002/2013JD020467>.

Gao, N., Cheng, M.D., Hopke, P.K., 1993. Potential source contribution function analysis and source apportionment of sulfur species measured at Rubidoux, CA during the southern California air quality study, 1987. *Analytica Chimica Acta* 277, 369–380. doi: 10.1016/0003-2670(93)80449-U

Geddes, J. A. and Martin, R. V.: Global deposition of total reactive nitrogen oxides from 1996 to 2014 constrained with satellite observations of NO₂ columns, *Atmos. Chem. Phys.*, 17, 10071–10091, 2017, <https://doi.org/10.5194/acp-17-10071-2017>

Gorkavyi, N. et al. (2021): Tracking aerosols and SO₂ clouds from the Raikoke eruption: 3D view from satellite observations, *Atm. Meas. Tech. Discuss.*, <https://doi.org/10.5194/amt-2021-58>.

Guffanti, M., T. J. Casadevall, and K. Budding (2010): Encounters of aircraft with volcanic ash clouds: A compilation of known incidents, 1953-2009, Tech. rep., U. S. Geological Survey, Data Series 545, ver. 1.0. [Available at <http://pubs.usgs.gov/ds/545/>].

Halton, J. H. (1960): On the Efficiency of Certain Quasi-Random Sequences of Points in Evaluating Multi-Dimensional Integrals. *Numerical Mathematical* 2 (1), 84–90, doi:10.1007/BF01386213.

He, H., Vinnikov, K., Li, C., Krotkov, N. A., Jongeward, A. R., Li, Z., Stehr, J. W., Hains, J. C., and Dickerson, R. R (2016).: Response of SO₂ and particulate air pollution to local and regional emission controls: A case study in Maryland, *Earth's Future*, doi:10.1002/2015EF000330

- Hedelt, P., Efremenko, D. S., Loyola, D. G., Spurr, R., and Clarisse, L. (2019): SO₂ Layer Height retrieval from Sentinel-5 Precursor/TROPOMI using FP_ILM, *Atmos. Meas. Tech.*, 12, 5503–5517, <https://doi.org/10.5194/amt-12-5503-2019>.
- Heo, J., McGinnis, J.E., de Foy, B., Schauer, J.J., (2013): Identification of potential source areas for elevated PM_{2.5}, nitrate and sulfate concentrations. *Atmos. Environ.* 71, 187–197. doi: 10.1016/j.atmosenv.2013.02.008
- Jaross, G., Bhartia, P. K., Chen, G., Kowitt, M., Haken, M., Chen, Z., Xu, P., Warner, J., and Kelly, T. (2014): OMPS Limb Profiler instrument performance assessment, *J. Geophys. Res. Atmos.*, 119, 4399– 4412, doi:10.1002/2013JD020482.
- Karagulian, F., Clarisse, L., Clerbaux, C., Prata, A. J., Hurtmans, D., and Coheur, P. F. (2010): Detection of volcanic SO₂, ash, and H₂SO₄ using the Infrared Atmospheric Sounding Interferometer (IASI), *J. Geophys. Res.*, 115, D00L02, doi:10.1029/2009JD012786.
- Kingma, D. P. and Ba, J. (2015): A Method for Stochastic Optimization, International Conference for Learning Representations, San Diego, CA, 8 May 2015.
- Kristiansen, N. I., Stohl, A., Prata, A. J., Richter, A., Eckhardt, S., Seibert, P., Hoffmann, A., Ritter, C., Bitar, L., Duck, T. J., and Stebel, K. (2010): Remote sensing and inverse transport modeling of the Kasatochi eruption sulfur dioxide cloud, *J. Geophys. Res.*, 115, D00L16, doi:10.1029/2009JD013286.
- Kristiansen, N. I., Prata, A. J., Stohl, A., and Carn, S. A. (2015): Stratospheric volcanic ash emissions from the 13 February 2014 Kelut eruption, *Geophys. Res. Lett.*, 42, 588–596, doi:10.1002/2014GL062307.
- Krotkov, N. A., Carn, S. A., Krueger, A. J., Bhartia, P. K., and Yang, K. (2006): Band residual difference algorithm for retrieval of SO₂ from the aura ozone monitoring instrument (OMI), *IEEE Transactions on Geoscience and Remote Sensing*, vol. 44, no. 5, pp. 1259-1266, doi: 10.1109/TGRS.2005.861932.
- Krotkov, N.A., Schoeberl, M.R., Morris, G.A., Carn, S. and Yang, K. (2010): Dispersion and lifetime of the SO₂ cloud from the August 2008 Kasatochi eruption. *Journal of Geophysical Research*, Vol. 115: doi: 10.1029/2010JD013984.

- Krotkov, N., McLinden, C.A, Li, C., L.N. Lamsal, Celarier, E. A., Marchenko, S. V., Swartz, W. H., Bucsela, E., Joiner, J., Duncan, B, Boersma, F., Veeffkind, P., Levelt, P., Fioletov, V., Dickerson, R. R., He, H., Lu, Z., and Streets, D. (2016): Aura OMI observations of regional SO₂ and NO₂ pollution changes from 2005-2015. *Atmos. Chem. Phys.*, 16, 4605–4629. doi: 10.5194/acp-16-4605-2016
- Krotkov, N., Realmuto, V., Li, C., Seftor, C., Li, J., Brentzel, K., Stuefer, M., Cable, J., Dierking, C., Delamere, J., Schneider, D., Tamminen, J., Hassinen, S., Ryyppö, T., Murray, J., Carn, S., Osiensky, J., Eckstein, N., Layne, G., Kirkendall, J. (2021): Day–Night Monitoring of Volcanic SO₂ and Ash Clouds for Aviation Avoidance at Northern Polar Latitudes. *Remote Sens.*, 13, 4003. <https://doi.org/10.3390/rs13194003>
- Krueger, A. J. (1983): Sighting of El Chichón sulfur dioxide clouds with the Nimbus 7 total ozone mapping spectrometer, *Science*, 220, 1377–1379, <https://doi.org/10.1126/science.220.4604.1377>.
- Krueger, A. J., L. S. Walter, P. K. Barthia, C. C. Schnetzler, N. A. Krotkov, I. Sprod, and G. J. S. Bluth (1995): Volcanic sulfur dioxide measurements from the Total Ozone Mapping Spectrometer instrument. *J. Geophys. Res.*, 100, 14 057–14 076.
- Lamb, D., and V. Bowersox. 2000. The national atmospheric deposition program: an overview. *Atmos Environ.* 34:1661–1663. doi: 10.1016/S1352-2310(99)00425-2
- Lamsal, L. N., Krotkov, N. A., Vasilkov, A., Marchenko, S., Qin, W., Yang, E.-S., Fasnacht, Z., Joiner, J., Choi, S., Haffner, D., Swartz, W. H., Fisher, B., and Bucsela, E.: Ozone Monitoring Instrument (OMI) Aura nitrogen dioxide standard product version 4.0 with improved surface and cloud treatments, *Atmos. Meas. Tech.*, 14, 455–479, <https://doi.org/10.5194/amt-14-455-2021>
- Lee, C., Martin, R. V., Van Donkelaar, A., O’Byrne, G., Krotkov, N., Richter, A., Huey, L. G., and Holloway, J. S. (2009): Retrieval of vertical columns of sulfur dioxide from SCIAMACHY and OMI: Air mass factor algorithm development, validation, and error analysis, *J. Geophys. Res.-Atmos.*, 114, D11301, doi:10.1029/2009JD012123.
- Lee, C., R. V. Martin, A. Van Donkelaar, R. R. Hanlim Lee, J. C. H. Dickerson, N. Krotkov, A. Richter, K. Vinnikov, and J. J. Schwab. (2011): SO₂ Emissions and Lifetimes: Estimates from Inverse Modeling Using in Situ and Global, Space-Based (SCIAMACHY and OMI)

- Observations, *Journal of Geophysical Research: Atmospheres* 116: (D6): n/a–n/a.
D06304. doi:10.1029/2010JD014758.
- Levelt, P. F., Noordhoek, R. (2002): OMI Algorithm Theoretical Basis Document, Volume I, OMI Instrument, Level 0 - 1B processor, Calibration and Operations.
URL: <https://eosps.nasa.gov/sites/default/files/atbd/ATBD-OMI-01.pdf>
- Levelt, P. F., Van Den Oord, G. H. J., Dobber, M. R., Mälkki, A., Visser, H., De Vries, J., Stammes, P., Lundell, J. O. V., and Saari, H. (2006b): The Ozone Monitoring Instrument, *IEEE Trans. Geosci. Remote Sens.*, 44, 1093–1101.
- Levelt, P., Joiner, J., Tamminen, J., Veefkind, P., Bhartia, P. K., Stein Zweers, D., Duncan, B. N., Streets, D. G., Eskes, H., van der A, R., McLinden, C., Fioletov, V., Carn, S., de Laat, J., DeLand, M., Marchenko, S., McPeters, R., Ziemke, J., Fu, D., Liu, X., Pickering, K., Apituley, A., González Abad, G., Arola, A., Boersma, F., Chan Miller, C., Chance, K., de Graaf, M., Hakkarainen, J., Hassinen, S., Ialongo, I., Kleipool, Q., Krotkov, N., Li, C., Lamsal, L., Newman, P., Nowlan, C., Suileiman, R., Tilstra, L. G., Torres, O., Wang, H., and Wargan, K. (2018): The Ozone Monitoring Instrument: overview of 14 years in space, *Atmos. Chem. Phys.*, 18, 5699–5745, <https://doi.org/10.5194/acp-18-5699-2018>
- Li, C., Joiner, J., Krotkov, N. A., and Bhartia, P. K. (2013): A fast and sensitive new satellite SO₂ retrieval algorithm based on principal component analysis: Application to the ozone monitoring instrument, *Geophys. Res. Lett.*, 40, 6314–6318,
doi:10.1002/2013GL058134.
- Li, C., McLinden, C., Fioletov, V., Krotkov, N., Carn, S., Joiner, J., Streets, D., He, H., Ren, X., Li, Z., and Dickerson, R. (2017a): India is overtaking China as the world’s largest emitter of anthropogenic sulfur dioxide, *Scientific Reports*, DOI:10.1038/s41598-017-14639-8.
- Li, C., Krotkov, N. A., Carn, S., Zhang, Y., Spurr, R. J. D., and Joiner, J. (2017bf): New-generation NASA Aura Ozone Monitoring Instrument (OMI) volcanic SO₂ dataset: algorithm description, initial results, and continuation with the Suomi-NPP Ozone Mapping and Profiler Suite (OMPS), *Atmos. Meas. Tech.*, 10, 445– 458,
<https://doi.org/10.5194/amt-10-445-2017>.

- Li, C., Krotkov, N. A., Leonard, P. J. T., Carn, S., Joiner, J., Spurr, R. J. D. and Vasilkov, A. (2020): Version 2 Ozone Monitoring Instrument SO₂ Product (OMSO2 V2): New Anthropogenic SO₂ Vertical Column Density Dataset, *Atmos. Meas. Tech.*, 13, 6175–6191, 2020 <https://doi.org/10.5194/amt-13-6175-2020>
- Likens G. E. and Bormann, H. F. (1974): Acid Rain: A Serious Regional Environmental Problem, *Science*, Vol 184, pp. 1176-1179, doi: 10.1126/science.184.4142.1176.
- Likens, G. E., Driscoll, C.T., Buso, D.C., Mitchell, M. J., Lovett, G. M., Bailey, S. W., Siccama, T. G., Reiners, W. A., Alewell, C. (2002), The biogeochemistry of sulfur at Hubbard Brook, *Biogeochemistry*, 60(3), 235-316.
- Loyola, D. G., M. Pedernana, and S. Gimeno Garcia. (2016): Smart Sampling and Incremental Function Learning for Very Large High Dimensional Data. *Neural Networks* 78: 75–87. doi:10.1016/j.neunet.2015.09.001.
- Loyola, D. G., Xu, J., Heue, K.-P., and Zimmer, W. (2020): Applying FP_ILM to the retrieval of geometry-dependent effective Lambertian equivalent reflectivity (GE_LER) daily maps from UVN satellite measurements, *Atmos. Meas. Tech.*, 13, 985–999, <https://doi.org/10.5194/amt-13-985-2020>.
- Ludewig, A., Kleipool, Q., Bartstra, R., Landzaat, R., Leloux, J., Loots, E., Meijering, P., van der Plas, E., Rozemeijer, N., Vonk, F., and Veeffkind, P. (2020): In-flight calibration results of the TROPOMI payload on-board the Sentinel-5 Precursor satellite, *Atmos. Meas. Tech.*, 13, 3561–3580, <https://doi.org/10.5194/amt-13-3561-2020>.
- Margitan, James J. (1984) Mechanism of the atmospheric oxidation of sulfur dioxide. Catalysis by hydroxyl radicals. *The Journal of Physical Chemistry*, 88 (15). 3314- 3318, doi:10.1021/j150659a035
- McCormick, M. P., L. W. Thomason, and C. R. Trepte. (1995): Atmospheric Effects of the Mt Pinatubo Eruption, *Nature* 373: 399–404. doi:10.1038/373399a0.
- McLinden, C. A., Fioletov, V., Shephard, M. W., Krotkov, N., Li, C., Martin, R. V., et al. 2016: Space-based detection of missing sulfur dioxide sources of global air pollution. *Nature Geoscience*, 9(7), 496–500. doi: 10.1038/ngeo2724
- McPeters, R.D., Bhartia, P.K., Krueger, A.J., Herman, J.R., Wellemeyer, C.G., Seftor, C.J., Jaross, G., Torres, O., Moy, L., Labow, G., Byerly, W., Taylor, S.L., Swissler, T., and

- Cebula, R.P. (1998). Earth probe total ozone mapping spectrometer (TOMS): data products user's guide. NASA Reference Publication 206895, 69 pp.
- Merucci, L., Burton, M., Corradini, S., and Salerno, G. G. (2011): Reconstruction of SO₂ flux emission chronology from spacebased measurements, *J. Volcanol. Geoth. Res.*, 206, 80–87, doi:10.1016/j.jvolgeores.2011.07.002.
- Munro, R., Lang, R., Klaes, D., Poli, G., Retscher, C., Lindstrot, R., Huckle, R., Lacan, A., Grzegorski, M., Holdak, A., Kokhanovsky, A., Livschitz, J., and Eisinger, M. (2016): The GOME-2 instrument on the Metop series of satellites: instrument design, calibration, and level 1 data processing – an overview, *Atmos. Meas. Tech.*, 9, 1279–1301, <https://doi.org/10.5194/amt-9-1279-2016>.
- National Atmospheric Deposition Program, 2016. Total Deposition 2015 Annual Map Summary. NADP Data Report 2016-02. Illinois State Water Survey, University of Illinois at Urbana-Champaign, IL.
- NASA Goddard Earth Sciences: Aura OMI Sulphur Dioxide Data Product-OMSO₂, available at: http://disc.sci.gsfc.nasa.gov/Aura/data-holdings/OMI/omso2_v003.shtml, Accessed 2017.
- NASA: CALIPSO LIDAR BROWSE IMAGES, available at: https://www-calipso.larc.nasa.gov/products/lidar/browse_images/production (last access: 5 March 2021), NASA [data set], 2011.
- NASA: Goddard Earth Sciences Data and Information Services Center (GES DISC), available at: <https://earthdata.nasa.gov/eosdis/daacs/gesdisc> (last access: 1 March 2021), NASA Earth Data [data set], 2020.
- NASA/LARC/SD/ASDC: CALIPSO Lidar Level 1B profile data, V4-10, NASA Langley Atmospheric Science Data Center DAAC [data set], https://doi.org/10.5067/CALIOP/CALIPSO/LID_L1-STANDARD-V4-10, 2016.
- Nowlan, C. R., X. Liu, K. Chance, Z. Cai, T. P. Kurosu, C. Lee, and R. V. Martin. (2011): Retrievals of Sulfur Dioxide from the Global Ozone Monitoring Experiment 2 (GOME-2) Using an Optimal Estimation Approach: Algorithm and Initial Validation, *Journal of Geophysical Research: Atmospheres* 116 (D18): n/a–n/a. D18301. doi:10.1029/2011JD015808.

- Odabasi, M., Bagiroz, H.O. (2002): Sulfate Dry Deposition Fluxes and Overall Deposition Velocities Measured with a Surrogate Surface. *Sci. Total Environ.* 297: 193–201, doi: 10.1016/s0048-9697(02)00127-4.
- Palmer, P. I., Jacob, D. J., Chance, K., Martin, R. V., Spurr, R. J. D., Kurosu, T. P., Bey, I., Yantosca, R., Fiore, A., and Li, Q. B. (2001): Air mass factor formulation for spectroscopic measurements from satellites: Application to formaldehyde retrievals from the Global Ozone Monitoring Experiment, *J. Geophys. Res.*, 106, 14 539–14 550.
- Pekney, Natalie J., Davidson, Cliff I., Zhou, Liming, Hopke, Philip K. (2006): Application of PSCF and CPF to PMF-Modeled Sources of PM_{2.5} in Pittsburgh, *Aerosol Science and Technology*, 40:10, 952-961. doi: 10.1080/02786820500543324
- Polissar, A. V., Hopke, P.K. , Paatero, P. , Kaufmann, Y.J., Hall, D.K. , Bodhaine, B.A. , Dutton, E.G. , Harris, J.M. (1999). *The aerosol at Barrow, Alaska: Long-term trends and source locations*, *Atmos Envir.*, 33, pp. 2441-2458. doi: 10.1016/S1352-2310(98)00423-3
- Platt, U. (1994): Differential optical absorption spectroscopy (DOAS), in *Air Monitoring by Spectroscopic Techniques*, M.W. Sigrist, ed., Chemical Analysis Series, Wiley, New York, 127, 27–84.
- Platt, U. and Stutz, J. (2008): *Differential Optical Absorption Spectroscopy, Physics of Earth and Space Environments*, Springer, Berlin, Germany, <https://doi.org/10.1007/978-3-540-75776-4>.
- Prata, A.J., Bernardo, C., (2007). Retrieval of volcanic SO₂ column abundance from atmospheric infrared sounder data. *J. Geophys. Res.* 112, D20204. <http://dx.doi.org/10.1029/2006JD007955>.
- Prata, A. J., G. Gangale, L. Clarisse, and F. Karagulian (2010): Ash and sulfur dioxide in the 2008 eruptions of Okmok and Kasatochi: Insights from high spectral resolution satellite measurements, *J. Geophys. Res.*, 115, D00L18, doi:10.1029/2009JD013556.
- Prata, A. T., Mingari, L., Folch, A., Macedonio, G., and Costa, A. (2021): FALL3D-8.0: a computational model for atmospheric transport and deposition of particles, aerosols and radionuclides – Part 2: Model validation, *Geosci. Model Dev.*, 14, 409–436, <https://doi.org/10.5194/gmd-14-409-2021>.

- Qu L.L, Xiao H.Y, Zheng N.J, Zhang Z.Y, Xu Y. (2016): Comparison of four methods for spatial interpolation of estimated atmospheric nitrogen deposition in South China. *Environ Sci Pollut Res*, doi: 10.1007/s11356-016-7995-0.
- Quan, J. N., Zhang, X. S., Zhang, Q., Guo, J. H., Vogt, R.D. (2008): Importance of sulfate emission to sulfur deposition at urban and rural sites in China, *Atmos. Res.*, 89, pp. 283-288, <https://doi.org/10.1016/j.atmosres.2008.02.015>.
- Quei er, M., Burton, M., Theys, N. et al. (2019): TROPOMI enables high resolution SO₂ flux observations from Mt. Etna, Italy, and beyond. *Sci Rep* 9, 957, <https://doi.org/10.1038/s41598-018-37807-w>
- Realmuto, V. J., Berk, A. (2016): Plume Tracker: Interactive mapping of volcanic sulfur dioxide emissions with high-performance radiative transfer modeling, *J. Volcanol. Geotherm. Res.* 2016, 327, 55–69, doi:10.1016/j.jvolgeores.2016.07.001
- Richter, A., Wittrock, F., and Burrows, J. P. (2006): SO₂ measurements with SCIAMACHY, in *Proceedings of the Atmospheric Science Conference, 8–12 May 2006, ESRI, Frascati (CD-ROM)*, Eur. Space Agen., Spec. Publ. ESA SP-628.
- Richter, A., Wittrock, F., Schonhardt, A., and Burrows, J. (2009): Quantifying volcanic SO₂ emissions using GOME2 measurements, *Geophys. Res. Abstr.*, EGU2009-7679, EGU General Assembly 2009, Vienna, Austria.
- Rix, M., P. Valks, N. Hao, D. Loyola, H. Schlager, H. Huntrieser, A. Flemming, U. Koehler, U. Schumann, and A. Inness. (2012): Volcanic SO₂, BrO and Plume Height Estimations Using GOME-2 Satellite Measurements during the Eruption of Eyjafjallaj kull in May 2010, *Journal of Geophysical Research (Atmospheres)* 117: D00U19. doi:10.1029/2011JD016718.
- Robock, A. and Mao, J. (1995): The volcanic signal in surface temperature observations, *Journal of Climate*, 8, 1086–1103 [https://doi.org/10.1175/1520-0442\(1995\)008<1086:TVSIST>2.0.CO;2](https://doi.org/10.1175/1520-0442(1995)008<1086:TVSIST>2.0.CO;2).
- Robock, A. (2002): Pinatubo eruption: The climatic aftermath, *Science*, 295, 1242–1244, doi: 10.1126/science.1069903.
- Samson, P. J., 1981: Trajectory Analysis of Summertime Sulfate Concentrations in the Northeast United States. *Journal of Applied Meteorology*, 19, 1382–1394. doi: 10.1175/1520-0450(1980)019<1382:TAOSSC>2.0.CO;2

- Schenkeveld, V. M. E., Jaross, G., Marchenko, S., Haffner, D., Kleipool, Q. L., Rozemeijer, N. C., Veefkind, J. P., and Levelt, P. F. (2017): In-flight performance of the Ozone Monitoring Instrument, *Atmos. Meas. Tech.*, 10, 1957–1986, <https://doi.org/10.5194/amt-10-1957-2017>.
- Schmidt, A.; Witham, C.S.; Theys, N.; Richards, N.A.D.; Thordarson, T.; Szpek, K.; Feng, W.; Hort, M.C.; Woolley, A.M.; Jones, A.R.; Redington, A.L.; Johnson, B.T.; Hayward, C.L.; Carslaw, K.S. (2014): Assessing hazards to aviation from sulfur dioxide emitted by explosive Icelandic eruptions. , *Journal of Geophysical Research D: Atmospheres*, Vol. 119, Issue 24, 14180-14196, doi: 10.1002/2014JD022070.
- Sears, T.M., Thomas, G.E., Carboni ,E., Smith, A.J.A., Grainger, R.G. (2013): SO₂ as a possible proxy for volcanic ash in aviation hazard avoidance. *J Geophys Res (Atmospheres)*, 118(11): doi:10.1002/jgrd.50505 doi:10.1002/jgrd.50505
- Seinfeld, J.H. and Pandis, S.N. (2006) *Atmospheric Chemistry and Physics: From Air Pollution to Climate Change*. 2nd Edition, John Wiley & Sons, New York
- Shah, V., Jaeglé, L., Thornton, J. A., Lopez-Hilfiker, F. D., Lee, B. H., Schroder, J. C., Campuzano-Jost, P., Jimenez, J. L., Guo, H., Sullivan, A. P., Weber, R. J., Green, J. R., Fiddler, M. N., Bililign, S., Campos, T. L., Stell, M., Weinheimer, A. J., Montzka, D. D., and Brown, S. S. (2018): Chemical feedbacks weaken the wintertime response of particulate sulfate and nitrate to emissions reductions over the eastern United States, *P. Natl. Acad. Sci. USA*, <https://doi.org/10.1073/pnas.1803295115>
- Shannon, J.D. (1997) Scales of sulfur concentrations and deposition from the perspective of the receptor. *Atmos. Envir.* 31, 3933–3939. doi:10.1016/S1352-2310(97)00242-2
- Shannon, J.D. Regional Trends in Wet Deposition of Sulfate in the United States and SO₂ Emissions from 1980 through 1995; *Atmos. Environ.* 1999, 33 (5), 807-816. doi: 10.1016/S1352-2310(98)00143-5
- Singh, A. and Agrawal, M. (2008): Acid rain and its ecological consequences, *Environmental Science, Medicine, Journal of Environmental Biology* 29(1):15-24.
- Smith, S. J., van Aardenne, J., Klimont, Z., Andres, R. J., Volke, A., and Delgado Arias, S. (2011): Anthropogenic sulfur dioxide emissions: 1850–2005, *Atmos. Chem. Phys.*, 11, 1101–1116, doi:10.5194/acp-11-1101-2011.

- Spurr, J.D.R. (2006). VLIDORT: A linearized pseudo-spherical vector discrete ordinate radiative transfer code for forward model and retrieval studies in multilayer multiple scattering media, *Journal of Quantitative Spectroscopy and Radiative Transfer*, Volume 102, Issue 2, Pages 316-342, <https://doi.org/10.1016/j.jqsrt.2006.05.005>.
- Spurr, R., de Haan, J., van Oss, R., and Vasilkov, A. (2008): Discreteordinate radiative transfer in a stratified medium with first-order rotational Raman scattering, *J. Quant. Spectrosc. Ra.*, 109, 404–425, <https://doi.org/10.1016/j.jqsrt.2007.08.011>.
- Stein, A.F., Draxler, R.R, Rolph, G.D., Stunder, B.J.B., Cohen, M.D., and Ngan, F., (2015). NOAA's HYSPLIT atmospheric transport and dispersion modeling system, *Bull. Amer. Meteor. Soc.*, **96**, 2059-2077. doi: [10.1175/BAMS-D-14-00110.1](https://doi.org/10.1175/BAMS-D-14-00110.1)
- Stenchikov, G., Ukhov, A., Osipov, S., Ahmadov, R., Grell, G., Cady-Pereira, K., et al. (2021): How does a Pinatubo-size volcanic cloud reach the middle stratosphere? *Journal of Geophysical Research: Atmospheres*, 126, e2020JD033829, <https://doi.org/10.1029/2020JD033829>
- Stohl, A. (1998) : Computation, accuracy and applications of trajectories – a review and bibliography, *Atmos. Environ.*, 32, 947–966, [https://doi.org/10.1016/S1352-2310\(97\)00457-3](https://doi.org/10.1016/S1352-2310(97)00457-3)
- Stohl, A., Forster, C., Frank, A., Seibert, P., and Wotawa, G. (2005): Technical note: The Lagrangian particle dispersion model FLEXPART version 6.2, *Atmos. Chem. Phys.*, 5, 2461–2474, <https://doi.org/10.5194/acp-5-2461-2005>
- Thomas, H. E., Prata, A.J. (2011): Sulphur dioxide as a volcanic ash proxy during the April–May 2010 eruption of Eyjafjallajökull Volcano, Iceland. *Atmos. Chem. Phys.*, 11, 6871–6880, doi:10.5194/acp-11-6871-2011.
- Torres, O., Bhartia, P. K., Jethva, H., and Ahn, C. (2018): Impact of the ozone monitoring instrument row anomaly on the long-term record of aerosol products, *Atmos. Meas. Tech.*, 11, 2701–2715, <https://doi.org/10.5194/amt-11-2701-2018>.
- Theys, N., Campion, R., Clarisse, L., Brenot, H., van Gent, J., Dils, B., Corradini, S., Merucci, L., Coheur, P.-F., Van Roozendael, M., Hurtmans, D., Clerbaux, C., Tait, S., and Ferrucci, F. (2013): Volcanic SO₂ fluxes derived from satellite data: a survey using OMI,

- GOME-2, IASI and MODIS, *Atmos. Chem. Phys.*, 13, 5945–5968,
<https://doi.org/10.5194/acp-13-5945-2013>.
- Theys, N., De Smedt, I., van Gent, J., Danckaert, T., Wang, T., Hendrick, F., Stavrou, T., Bauduin, S., Clarisse, L., Li, C., Krotkov, N., Yu, H., Brenot, H., and Van Roozendael, M. (2015): Sulfur dioxide vertical column DOAS retrievals from the Ozone Monitoring Instrument: Global observations and comparison to ground-based and satellite data, *J. Geophys. Res. Atmos.*, 120, 2014JD022657, doi:10.1002/2014JD022657.
- Theys, N., Hedelt, P., De Smedt, I. *et al.* Global monitoring of volcanic SO₂ degassing with unprecedented resolution from TROPOMI onboard Sentinel-5 Precursor. *Sci Rep* **9**, 2643 (2019). <https://doi.org/10.1038/s41598-019-39279-y>
- Theys, N., Fioletov, V., Li, C., De Smedt, I., Lerot, C., McLinden, C., Krotkov, N., Griffin, D., Clarisse, L., Hedelt, P., Loyola, D., Wagner, T., Kumar, V., Innes, A., Ribas, R., Hendrick, F., Vlietinck, J., Brenot, H., and Van Roozendael, M.: A Sulfur Dioxide Covariance-Based Retrieval Algorithm (COBRA): application to TROPOMI reveals new emission sources, *Atmos. Chem. Phys. Discuss.* [preprint], <https://doi.org/10.5194/acp-2021-294> , accepted, 2021.
- U.S. EPA (United States Environmental Protection Agency). 2017. Data from the Clean Air Status and Trends Network. Accessed 2017. <https://www.epa.gov/castnet>
- U.S. EPA. (2002): EPA Acid Rain Program 2001 Progress Report. EPA-430-R-02-009. Clean Air Markets Program, Office of Air and Radiation, Nov 2002.
- U.S. EPA. (2003): Latest findings on national air quality: 2002 status and trends. EPA/454/K-03/001. Research Triangle Park, NC.
- U.S. EPA. (2015): The Clean Air Act – Highlights of the 1990 Amendment.
https://www.epa.gov/sites/production/files/2015-11/documents/the_clean_air_act_-_highlights_of_the_1990_amendments.pdf
- Vasilkov, A., Qin, W., Krotkov, N., Lamsal, L., Spurr, R., Haffner, D., Joiner, J., Yang, E.-S. and Marchenko, S. (2017): Accounting for the effects of surface BRDF on satellite cloud and trace-gas retrievals: a new approach based on geometry-dependent Lambertian equivalent reflectivity applied to OMI algorithms, *Atmospheric Measurement Techniques*, 10(1), 333–349, doi:10.5194/amt-10-333-2017.

- Vernier, J.-P., Fairlie, T. D., Deshler, T., Natarajan, M., Knepp, T., Foster, K., Wienhold, F. G., Bedka, K. M., Thomason, L., and Trepte, C. (2016): In situ and space-based observations of the Kelud volcanic plume: The persistence of ash in the lower stratosphere, *J. Geophys. Res. Atmos.*, 121, 11104–11118, <https://doi.org/10.1002/2016JD025344>.
- Vet, R., Artz, R. S., Carou, S., Shaw, M., Ro, C.-U., Aas, W., Baker, A., Bowersox, V. C., Dentener, F., Galay-Lacaux, C., Hou, A., Pienaar, J. J., Gillet, R., Forti, M. C., Gromov, S., Hara, H., Khodzher, T., Mahowald, M., Nickovic, S., Rao, P. S. P., and Reid, N. W. (2014): A global assessment of precipitation chemistry and deposition of sulfur, nitrogen, sea salt, base cations, organic acids, acidity and pH, and phosphorus, *Atmos. Environ.*, 93, 3– 100, doi:10.1016/j.atmosenv.2013.10.060
- von Glasow, R., Bobrowski, N., and Kern, C. (2009): The effects of volcanic eruptions on atmospheric chemistry, *Chem. Geol.*, 263, 131–142, <https://doi.org/10.1016/j.chemgeo.2008.08.020>.
- Wang, Y., Zhang, X., & Draxler, R. R. TrajStat, (2009): GIS-based software that uses various trajectory statistical analysis methods to identify potential sources from long-term air pollution measurement data. *Environmental Modelling & Software*, 24(8), 938–939. doi:10.1016/j.envsoft.2009.01.004
- Wetherbee, G. A., (2017): Precipitation collector bias and its effects on temporal trends and spatial variability in National Atmospheric Deposition Program/National Trends Network data. *Environmental Pollution*, 223, 90–101. doi:10.1016/j.envpol.2016.12.036
- Xu, Y., Carmichael, G. R. (1998): Modeling the dry deposition velocity of sulfur dioxide and sulfate in Asia, *Journal of Applied Meteorology*, 37, pp. 1084-1099, doi: 10.1175/15200450(1998)037<1084:mtddvo>2.0.co;2.
- Xu, J., Schüssler, O., Loyola R., D., Romahn, F., and Doicu, A. (2017): A novel ozone profile shape retrieval using Full-Physics Inverse Learning Machine (FP_ILM)., *IEEE J. Sel. Topics Appl. Earth Observ. Remote Sens.*, 10, 5442–5457, <https://doi.org/10.1109/JSTARS.2017.2740168>.
- Yang, K., N. A. Krotkov, A. J. Krueger, S. A. Carn, P. K. Bhartia, and P. F. Levelt. (2007): Retrieval of large volcanic SO₂ columns from the Aura Ozone Monitoring

- Instrument: Comparison and limitations, *J. Geophys. Res.*, 112, D24S43, doi:10.1029/2007JD008825.
- Yang, K., X. Liu, N. A. Krotkov, A. J. Krueger, and S. A. Carn, (2009): Estimating the altitude of volcanic sulfur dioxide plumes from space borne hyper-spectral UV measurements, *Geophys. Res. Lett.*, 36, L10803, doi:10.1029/2009GL038025.
- Yang, K., P. K. Xiong Liu, N. A. Bhartia, S. A. Krotkov, E. J. Carn, A. J. Hughes, R. J. Krueger, D. Spurr, and S. G. Trahan (2010): Direct Retrieval of Sulfur Dioxide Amount and Altitude from Spaceborne Hyperspectral UV Measurements: Theory and Application, *Journal of Geophysical Research: Atmospheres* 115: D2. doi:10.1029/2010JD013982.
- Yang, K., Dickerson, R., Carn, S. Ge, C., and Wang, J. (2013): First observations of SO₂ from the satellite Suomi NPP OMPS: Widespread air pollution events over China, *Geophys. Res. Lett.*, 40, 4957-4962, <https://doi.org/10.1002/grl.50952>.
- Young, A. T. (1981): Rayleigh Scattering. *Applications Optical* 20 (4): 533–535. doi:10.1364/AO.20.000533.
- Zhang, Z. Y., Wong, M. S. and Lee, K. H. (2015): Estimation of potential source regions of PM_{2.5} in Beijing using backward trajectories, *Atmos. Pollut. Res.*, 6(1), 173–177. doi:10.5094/APR.2015.020.
- Zhang, Y., Li, C., Krotkov, N. A., Joiner, J., Fioletov, V., and McLinden, C. (2017): Continuation of long-term global SO₂ pollution monitoring from OMI to OMPS, *Atmos. Meas. Tech.*, 10, 1495–1509, <https://doi.org/10.5194/amt-10-1495-2017>.
- Zheng, B., Tong, D., Li, M., Liu, F., Hong, C., Geng, G., Li, H., Li, X., Peng, L., Qi, J., Yan, L., Zhang, Y., Zhao, H., Zheng, Y., He, K., and Zhang, Q. (2018): Trends in China's anthropogenic emissions since 2010 as the consequence of clean air actions, *Atmos. Chem. Phys.*, 18, 14095–14111, <https://doi.org/10.5194/acp-18-14095-2018>.